
# Electrostatic potential measurements and point cusp theories applied to a low beta Polywell fusion device

Matthew Carr (SID: 309143487)

School of Physics
University of Sydney
Australia

A thesis submitted for the degree of Doctor of Philosophy (Research)

February 26, 2013

# Declaration of originality

I certify that the work presented in this thesis was undertaken solely during my PhD candidature, and has not been presented for any other degree.

I certify also that this thesis was written by myself, and that to the best of my knowledge, this thesis contains no copy or paraphrase of work published by another person, except where duly acknowledged in the text.

Signature of candidate:

.....

Matthew Carr

## Abstract

The magnetic field structure in a Polywell device is studied to understand both the physics underlying the electron confinement properties and its estimated performance compared to other cusped devices. Analytical expressions are presented for the magnetic field in addition to expressions for the point and line cusps as a function of device parameters. It is found that at small coil spacings, it is possible for the point cusp losses to dominate over the line cusp losses, leading to longer overall electron confinement. The types of single particle trajectories that can occur are analysed in the context of the magnetic field structure which results in the ability to define two general classes of trajectories, separated by a critical flux surface. In addition, knowledge of the types of electron trajectories is used to propose a ballistic model for the single particle confinement time and is subsequently compared with simulation results.

Floating potential measurements were carried out on a prototype Teflon Polywell with a cylindrical hollow cathode electron gun. Dynamic floating potentials of up to –250 V were obtained for periods of several milliseconds, suggesting the formation of a virtual cathode stable on at least the millisecond time scale. The dependence of the floating potential on the coil current and background gas pressure was studied. The magnetic field coils were driven by a pulsed current supply and it was found that the virtual cathode could only be established within a narrow range of currents. In addition, it was shown that the magnitude of the floating potential increased with decreasing background gas pressure. It is conjectured that the depth of the virtual cathode and its lifetime are dependent on the magnitude of the injected electron current.

Finally, orbital limited motion theory was been applied to two biased probes in a low beta Polywell approximating a small scale WB6 design, referred to as WB6-mini. The cases studied include electron injection, magnetic field scaling, Polywell bias scaling, and radial position profiles. Langmuir's original orbital limited motion results for a monoenergetic electron beam are shown to be in excellent agreement for electron injection into the Polywell. A distribution function is proposed for the electron plasma characteristics in the centre of the magnetic null and confirmed with experimental results. A translational stage was used to measure the radial plasma potential profile. In other experiments two probes were used to simultaneously measure the profiles in both the null and a position halfway along a corner cusp. The results confirm a radial potential well created by electron trapping in the device. In addition, we present preliminary results of the potential well scaling with the magnetic field, Polywell bias voltage, and the injected beam current. The electron population was found to maintain non-equilibrium in all cases studied.

## Acknowledgements

Through the years many people have helped me develop as a scientist and a person. I would very much like to thank them all for their support and guidance.

I would like to give an extra special thanks to my supervisor, A/Prof. Joe Khachan. Joe has taught me so much over the years and really guided my development as a scientist. Despite his busy teaching schedule, somehow he always finds the time to help his students. Whether it is experiments in the lab, discussing theoretical ideas and problems, or even just a social chat, Joe's door is always open. We also shared many great lunches dreaming about entrepreneurialism and taking practical innovative science out into the world. Joe's passion has been very inspiring.

I also thank my co-supervisor Dr. Alex Samarian for his helpful comments and challenging my ideas about biased Langmuir probes. I'd like to thank Prof. Rod Cross for being an inspiration to me. He always showed an enthusiasm for experimental physics that I have rarely seen. I also thank many members of the wider plasma physics community of the School of Physics for their stimulating discussions and advice, especially Dr Cenk Kocer, Dr Ian Falconer and Dr Stephen Bosi.

Mr. Phil Dennis deserves extra special thanks for the many countless hours of advice and mentoring. He basically made me an apprentice and taught me so much about circuit design and testing. Thanks also goes to Mr. John Pigott for help with power supply design in the first year of my PhD. The workshop staff, Mr. Michael Paterson and Mr. Terry Pfeiffer, provided countless hours of advice on design of structural components and helped to build most of the equipment in this thesis. Mr. Rob Davies also provided technical advice and could always help me to find parts and tools when needed in the lab.

I wish to express gratitude to the UPA scholarship scheme and the Denison Postgraduate Award, both of which allowed me to work full time on the PhD.

Thanks to the previous students, in particular Dr. John Kipritidis for mentoring me as a new student to the school and Dr. Oded Shrier for many deep philosophical discussions and introducing me to Jiddtek and Les. I have had the pleasure of sharing our office with some great friends, including fellow students David Gummersall, Scott Cornish, Rehan Bandara, Adam Israel, Johnson Ren and Dominic Poznic. Thanks to all of you for the camaraderie and helpful discussion. In particular, thanks to my fellow students of the Polywell, David, Scott and Johnson, for help with proof reading of papers, sharing experimental ideas and correcting mistakes in my work.

A very special thanks to my partner, Wendy, for your love and support over the years. I am especially thankful for your patience with me during the hard times. And finally, a very special thanks to my family. My Dad, Trevor, deserves a special thanks for spending countless hours helping me to debug and fix my circuits. My mum has inspired me with her dedication to her practice and compassion. And my brother James and I have always been so close and share ambitious dreams for the future.

This work is dedicated to my parents.

# Publications by the Author

## Refereed articles

- M. Carr, D. Gummersall, S. Cornish, and J. Khachan. *"Low beta confinement in a Polywell modelled with conventional point cusp theories "* Physics of Plasmas. **18** (2011) 112501.
- M. Carr, and J. Khachan. *"The dependence of the virtual cathode in a Polywell on the coil current and background gas pressure"* Physics of Plasmas. **17** (2010) 052510.
- M. Carr, and J. Khachan. *"A biased probe analysis of potential well formation in an electron only, low beta Polywell magnetic field."* Currently under internal review.

## Conference proceedings

- M. Carr, D. Gummersall, S. Cornish, and J. Khachan. *"Conventional Point Cusp Theories Applied to the Polywell."*. 13th US-Japan Workshop on IEC Fusion, The Menzies Hotel, Sydney, Australia, Dec 7 – 8, 2011.
- M. Carr, and J. Khachan. *"Progress in the Sydney University Polywell project"*. 12th US-Japan Workshop on IEC Fusion, KKR Hotel, Osaka, Japan, Oct 20 – 21, 2010.
- M. Carr, D. V. Gummersall and J. Khachan. *"First steps towards a Polywell fusion device prototype"*. 11th US-Japan Workshop on IEC Fusion, University of Wisconsin, Madison, USA, Oct 12 – 13, 2009.

## Posters

- M. Carr, and J. Khachan. *"Virtual Cathode formation in a Polywell fusion device"*. 10th Carolus Magnus Summer School on Plasma and Fusion Energy Physics. Weert, The Netherlands, September 4 – 16, 2011.
- M. Carr, and J. Khachan. *"Virtual Cathode lifetimes and floating potential measurements in a Polywell fusion device"*. Bulletin of the American Physical Society. **55** 2010.
- M. Carr, and J. Khachan. *"Virtual Cathode lifetimes and floating potential measurements in a Polywell fusion device"*. 47th Culham Plasma Physics Summer School, University of Oxford, UK, July 12 – 23, 2010.

# Contents

**Abstract** v

**Acknowledgements** vi

**Publications by the Author** vii

**1 Introduction** 1
- 1.1 Nuclear Fusion . . . 1
  - 1.1.1 Fusion Reaction Rate . . . 3
- 1.2 Magnetic Confinement Schemes . . . 4
  - 1.2.1 Closed (toroidal) confinement systems . . . 4
  - 1.2.2 Open (mirror) confinement systems . . . 6
- 1.3 Inertial Electrostatic Confinement . . . 9
- 1.4 The Polywell . . . 11
  - 1.4.1 The Key Concepts - a Hybrid Device . . . 11
  - 1.4.2 Experimental Polywells . . . 14
  - 1.4.3 PIC Simulations . . . 16
  - 1.4.4 Advanced Fuels . . . 16
  - 1.4.5 Non-electrical Applications of Polywell Fusion Research . . . 17
- 1.5 Criticism of the Polywell Concept . . . 18
  - 1.5.1 Ion Thermalisation . . . 18
  - 1.5.2 Core Convergence and Ion Defocusing . . . 19
  - 1.5.3 Electron Cusp Losses . . . 20
- 1.6 Aims of the Thesis . . . 20

**2 Magnetic Fields** 21
- 2.1 Single Current Loops . . . 21
- 2.2 Six Polywell coils . . . 23
- 2.3 B Field Structure and Single Particle Trajectories . . . 25
- 2.4 Point and Line Cusps . . . 30
- 2.5 Central Magnetic Field Approximation . . . 39
- 2.6 Approximate loss rate and confinement time . . . 42
- 2.7 Electrostatic Plugging of Point Cusps . . . 44
- 2.8 Summary . . . 45

**3 Experimental Setup and Techniques** **47**
3.1 Teflon Polywell Experiments . . . 47
3.1.1 Design Rationale and Construction . . . 47
3.1.2 High Current Pulsed Power Supply . . . 50
3.1.3 Cylindrical Cathode Electron Source . . . 52
3.1.4 Langmuir Probe Construction . . . 53
3.1.5 Vacuum Chamber and Mounting . . . 54
3.1.6 Copper Collector Plates . . . 56
3.2 WB6-mini . . . 57
3.2.1 Design Rationale and Construction . . . 57
3.2.2 Constant Current Power Supply . . . 61
3.2.3 Filament Electron Sources . . . 61
3.2.4 Langmuir Probe Mounting . . . 62
3.3 Biased Langmuir Probe Driver . . . 65
3.4 Confinement Time Clamp Circuit . . . 70

**4 Floating Potential Measurements in a Teflon Polywell** **73**
4.1 The Floating Potential as a Diagnostic for the Plasma Potential . . . 73
4.2 Electron Confinement Predictions . . . 74
4.3 Floating Potential Measurements . . . 76
4.3.1 Well variation with magnetic field strength . . . 76
4.3.2 Dependence on electron injection energy and current . . . 83
4.3.3 Dependence on gas pressure . . . 85
4.4 Collector Plates . . . 85
4.5 Summary . . . 90

**5 Biased Probe Results and Analysis in WB6-mini** **91**
5.1 Introduction and Motivation . . . 91
5.2 Experimental Setup . . . 92
5.3 Orbital Limited Motion Langmuir Probe Theory . . . 93
5.4 Analysis of Electron Injection . . . 95
5.5 With B and Without B Test Cases . . . 99
5.6 Radial plasma potential profile in a strong magnetic field . . . 105
5.7 Scaling with B and E . . . 108
5.8 Summary . . . 114

**6 Conclusions and Further Work** **115**

**7 Bibliography** **119**

**Appendix** **127**

**A Derivations** **127**
A.1 The monoenergetic isotropic distribution function . . . . . 127
A.2 Potential Well Derivation . . . . . 128

**B Power Supplies and Custom Electronics** **131**
B.1 Pulsed High Current Capacitor Supply Circuit . . . . . 131
B.2 Langmuir Probe Driver Circuit . . . . . 132
B.2.1 Arduino Microcontroller Code . . . . . 135

Chapter 1

# Introduction

The worlds population crossed the 7 billion people mark in late 2012 [4] and is expected to grow to almost 10 billion people by the year 2050 [8]. As the world population grows, so too do our expectations of higher living standards, longer life expectancy and general quality of life. The world energy market is in many ways the lynch pin that supports so much of our growth, however simply expanding the existing fossil fuel based infrastructure will only further strain our already endangered natural environment. If the human race is to be truly sustainable we must find new sources of base-load power that can ease environmental pressures and continue to support improvements in quality of life. Many "green technology" solutions have emerged in recent years, but few have the reliability and economic viability to be suitable for base-load power [13]. One of the most promising options in terms of the potential for radical change in the energy infrastructure landscape is nuclear energy.

Nuclear fission is the better known nuclear technology solution that already has a significant presence in the energy market as a proven technology [12]. However its use has been limited by concerns for proliferation of weapons grade nuclear materials, the inherent safety risks with regard to potential for a nuclear accident, and general concerns around radioactive waste. Generation IV fission technology [8] attempts to address these wide ranging concerns, but is generally considered to be on the horizon. Most of the proposed solutions are in the very early prototyping phase. The other potential solution for practical nuclear energy is nuclear fusion.

## 1.1 Nuclear Fusion

Nuclear fusion is a reaction in which two light nuclei collide to form a single heavier nucleus [43, 12, 48]. In this process a significant proportion of the mass of the reacting nuclei is converted directly into energy, making nuclear fusion one of the most energetic reactions known. As a potential energy source, fusion has several clear advantages over nuclear fission: the fuel used is naturally abundant and readily available, and the waste products are usually light stable nuclei.

However, a serious obstacle to the fusion process is that all nuclei are positively charged, and hence there is a large repulsive force between two nuclei in close proximity. For a fusion reaction to occur, the two nuclei must be sufficiently close for the attractive strong nuclear force to dominate. This requires a very large amount of energy, known as the coulomb barrier. By comparison, nuclear fission reactions can be induced by neutrons which have no net charge, and thus there is no coulomb barrier in a fission reaction and low energy incident particles can be used. For example, the reaction cross section for $^{235}$U increases with decreasing neutron

| Reaction | Thermonuclear Energy Released | Threshold Energy |
|---|---|---|
| $D + T \rightarrow {}^4He + n(14.1\ MeV)$ | 17.4 MeV | 4 keV |
| $D + D \rightarrow \begin{cases} T + p(3\ MeV) \\ {}^3He + n(2.5\ MeV) \end{cases}$ | 4.0 MeV | 35 keV |
| | 3.25 MeV | 35 keV |
| $D + {}^3He \rightarrow {}^4He + p$ (14.7 MeV) | 18.2 MeV | 30 keV |

Table 1.1: The fusion reactions of primary research interest [48].

energy[12]. However for fusion, the cross sections tends to decrease with decreasing energy due to the mutual repulsion of the reacting ions. This fact is the largest single factor that makes fusion reactions much more difficult to produce than fission reactions.

When a gas is heated to thermonuclear temperatures on the order of $10^8$ K, a significant number of particles in the gas will have sufficient energy to tunnel through the coulomb barrier and produce a fusion reaction. At these temperatures the nuclei and electrons of the gas have separated, forming a new state of matter called a plasma. The energy released in these reactions will heat the plasma further and hence sustain the fusion reactions occurring within it. This process occurs naturally in stars and is the fundamental source of most of the energy on the earth due to the energy from the sun.

Only a small number of the possible fusion reactions are candidates for energy research because of the high threshold energies required and corresponding energy output (see Table 1.1). Generally, the more stable the end product, the larger the energy released in the reaction. The deuterium - tritium (D-T) reaction is the reaction of choice for most fusion reactor designs because of its large energy output and relatively low threshold energy. A disadvantage is that such a large portion of the product energy leaves with the neutron, which is in a form that requires further technical infrastructure that has yet to be developed for energy recovery from the neutrons. Nuclear fission is quite advantageous in this respect because most of the reaction energy is given to the kinetic energy of the fission fragments making it easy to extract, which is technically less challenging than extraction of energy from neutrons, and is a current technology used in nuclear power plants.

The source of energy released in nuclear reactions is the nuclear binding energy. A stable bound system must have a lower potential energy in its bound configuration than its constituent parts. It is equivalent to the energy required to disassemble a nucleus into its free unbound neutrons and protons. When two light nuclei combine in a fusion reaction to form a product nucleus, the difference in binding energies is released either as gamma radiation or as the kinetic energy of the products. The binding energy per nucleon curve is shown in Figure 1.1 and reaches its maximum around $^{62}$Ni, $^{58}$Fe and $^{56}$Fe, after which fusion becomes an endothermic reaction.

The energy released is much larger than chemical reactions because the binding energy of the nucleus is much larger than the binding energy of electrons to a nucleus. For example, the

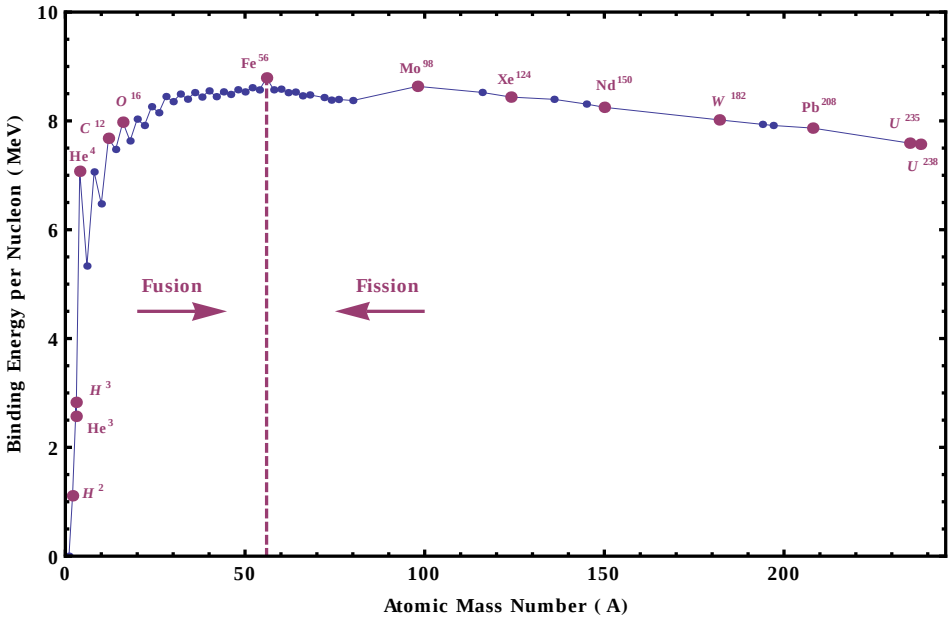


Figure 1.1: The binding energy per nucleon of some common isotopes. Data from [9].

typical energy of ionisation is on the order of eV's compared with the MeV's released in fusion. Even when compared with fission, the energy density released is many times greater in fusion. Fusion reactions produce far greater energies per unit mass even though individual fission events are generally much more energetic than a fusion event. Only direct conversion of mass to energy is more energetic per unit of mass than fusion.

### 1.1.1 Fusion Reaction Rate

The reaction rate per unit volume can be expressed as:

$$R = n_1 n_2 \langle \sigma v \rangle_{12} \tag{1.1}$$

where $n_1$ and $n_2$ are the number densities of the two fuel species and $\langle \sigma v \rangle_{12}$ is the fusion reactivity, and $\sigma$ is the cross section for fusion reactions. In thermonuclear fusion there will typically be a distribution of particle energies described by the Maxwell-Boltzmann distribution

$$n(v) \propto e^{-mv^2/2kT} \tag{1.2}$$

where $n(v)v^2dv$ gives the relative probability of finding a particle with speed between $v$ and $v+dv$ in a collection of particles in thermal equilibrium with temperature $T$ [12]. The fusion cross section can be adapted from basic expressions for nuclear cross sections including the standard $1/v$ term, and a barrier penetration factor to account for the probability of quantum tunnelling. Hence we arrive at the fusion reactivity averaged over all energies.

$$\langle \sigma v \rangle \propto \int_0^\infty \frac{1}{v} e^{-2G} e^{-mv^2/2kT} v^2 dv \tag{1.3}$$

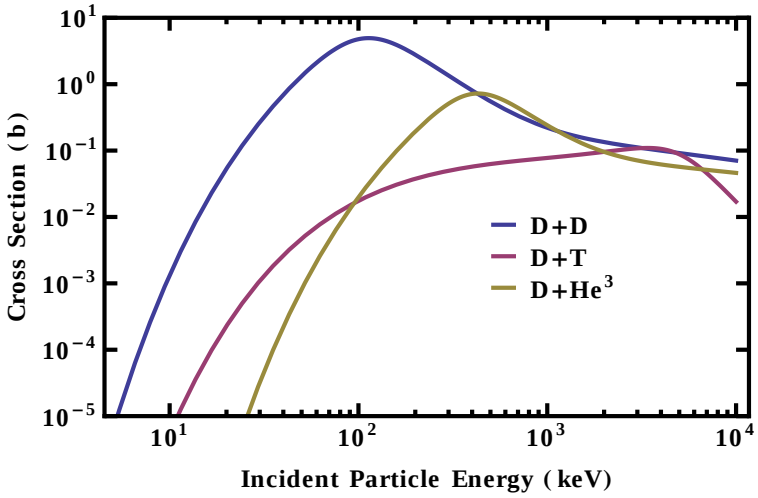


Figure 1.2: Values of the fusion reaction cross-section $\sigma$ (barns) calculated for three of the most significant fusion reactions [7, 10, 14].

## 1.2 Magnetic Confinement Schemes

A fusion plasma at thermonuclear energies cannot easily be contained in any material chamber because when allowed to come in contact with the walls, the plasma will sputter away wall material, removing energy from the plasma and potentially damaging the confining structure. Furthermore, the eroded wall material acts as an impurity that radiates away a large fraction of the plasma energy, rapidly quenching the plasma. Magnetic confinement concepts centre around the idea that charged particles will gyrate around magnetic field lines. In a sufficiently large magnetic field, the radius of gyration can be very small such that drift motion of particles is constrained along magnetic field lines. The study of magnetic confinement devices is split on the basis of the confining magnetic field geometry in to two configurations, either open or closed systems.

### 1.2.1 Closed (toroidal) confinement systems

Magnetic field lines can be configured to loop back on themselves, and hence be completely closed systems, by carefully choosing the spatial arrangement of magnetic coils. The simplest configuration is the torus where many individual magnetic coils from a solenoid are bent around in a closed loop to make a toroidal magnetic field (see Figure 1.3). In principle, charged particles will follow the field lines and be confined within the torus indefinitely. However the spatial non-uniformity created by bending the field lines leads to uneven forces during the gyration of the particle about a field line. This results in a drift force known as grad B ($\nabla \vec{B}$) drift, which causes the particles to drift out radially towards the outer wall.

Particle loss due to grad B drift is countered by the superposition of a poloidal magnetic

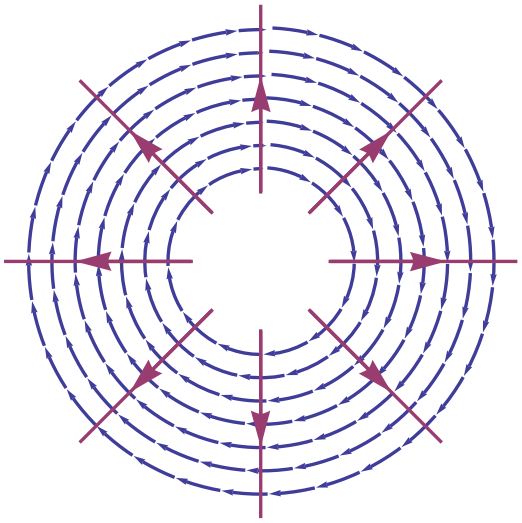

Figure 1.3: The closed magnetic fieldline geometry of a Tokamak [47, 48].

field on top of the toroidal magnetic field, resulting in a helical magnetic field geometry. In the tokamak configuration, the plasma acts as the secondary of a step down transformer, and external coils are used to induce a current in the plasma in the toroidal direction. This induced plasma current creates the poloidal magnetic field to confine the plasma and prevent it from reaching the vessel walls.

The unique combination of magnetic fields utilised in the Tokamak has proven highly successful in confining plasmas with temperatures over 1 million degrees. The Joint European Torus holds the record for fusion power attained with $Q = 0.62$ at 16MW [11]. ITER is a significant international collaboration which aims to be the first magnetic confinement system with a $Q \geqslant 10$.

Perhaps the biggest hindrance to the development of the Tokamak has been the discovery of various instabilities that weaken its confining properties. Instabilities can arise because the plasma itself creates magnetic and electric fields which counteract the confining magnetic field. As a consequence, the size of the vessel required for power gain has steadily increased to combat the instabilities in Tokamak plasmas. The current design for the next generation Tokamak, ITER, has a plasma radius on the order of 6 m with no currently known physics that can result in the miniaturisation of the design, placing severe limitations on the application, economics and portability of the Tokamak as a power source. The Tokamak will likely be successful as the first large scale fusion power-plant, but may never have the scalability and wide applicability originally intended by its designers.

### 1.2.2 Open (mirror) confinement systems

It may seem counter-intuitive to use an open magnetic field system for plasma confinement since the fieldlines appear to guide the gyrating particles out of the trap. However, open magnetic field systems can still confine charged particles by creating a magnetic well[47]. These magnetic well configurations utilise conservation of energy and the magnetic moment to create constraints on the particle motion along a fieldline. This effect is known as the magnetic mirror effect.

#### Mirror Machines

The simplest magnetic mirror device is created by using two solenoidal coils in a magnetic field configuration known as the Magnetic Mirror Machine, see Figure 1.4 for an annotated example. The maximum magnetic field, $B_{max}$, is produced on the axes of the two magnetic field coils located at $\pm x_{max}$. On any field line between the two coils, the field strength decreases to a minimum, $B_{min}$, at the centre of the device. If the spatial variation of the magnetic field, $|\nabla B/B|$, is small compared with the radius of gyration $r_g$,

$$r_g|\frac{\nabla B}{B}| \ll 1, \tag{1.4}$$

then the magnetic moment, $\mu$, is an approximate constant of motion. From elementary electrodynamics we know that magnetic forces do no work, and thus the kinetic energy ($KE$) of a particle must remain constant if no other forces act. For the purposes of understanding the mirror reflection effect it is convenient to split the $KE$ into velocity terms perpendicular and parallel to the applied magnetic field.

$$KE = \frac{1}{2}m[v_{\parallel}^2(x) + v_{\perp}^2(x)] = constant \tag{1.5}$$

The magnetic moment is

$$\mu = \frac{mv_{\perp}^2(x)}{2B(x)}, \tag{1.6}$$

which is a constant of motion providing condition 1.4 is satisfied. These expressions can be combined to yield the relationship between the velocity of a particle along a field line, the magnetic field strength along the field line, and the constants of motion of the particles [47],

$$v_{\parallel}^2(x) = \frac{2}{m}[KE - \mu B(x)]. \tag{1.7}$$

For the initial conditions of a given particle, if the magnetic field $B$ becomes sufficiently large along $x$ such that $B(x) = KE/\mu$ then $v_{\parallel} = 0$, meaning that the component of velocity along the magnetic field is zero and the particle is reflected at the point $x$ back along the field line. Hence, it is possible to confine a particle indefinitely in a magnetic well if its constants of motion constrain the particles orbit to bounce between the peak magnetic field points.

The velocity space for particles inside a mirror machine field can be divided into classes of particles that will either be confined indefinitely or escape on a single transit. It is more

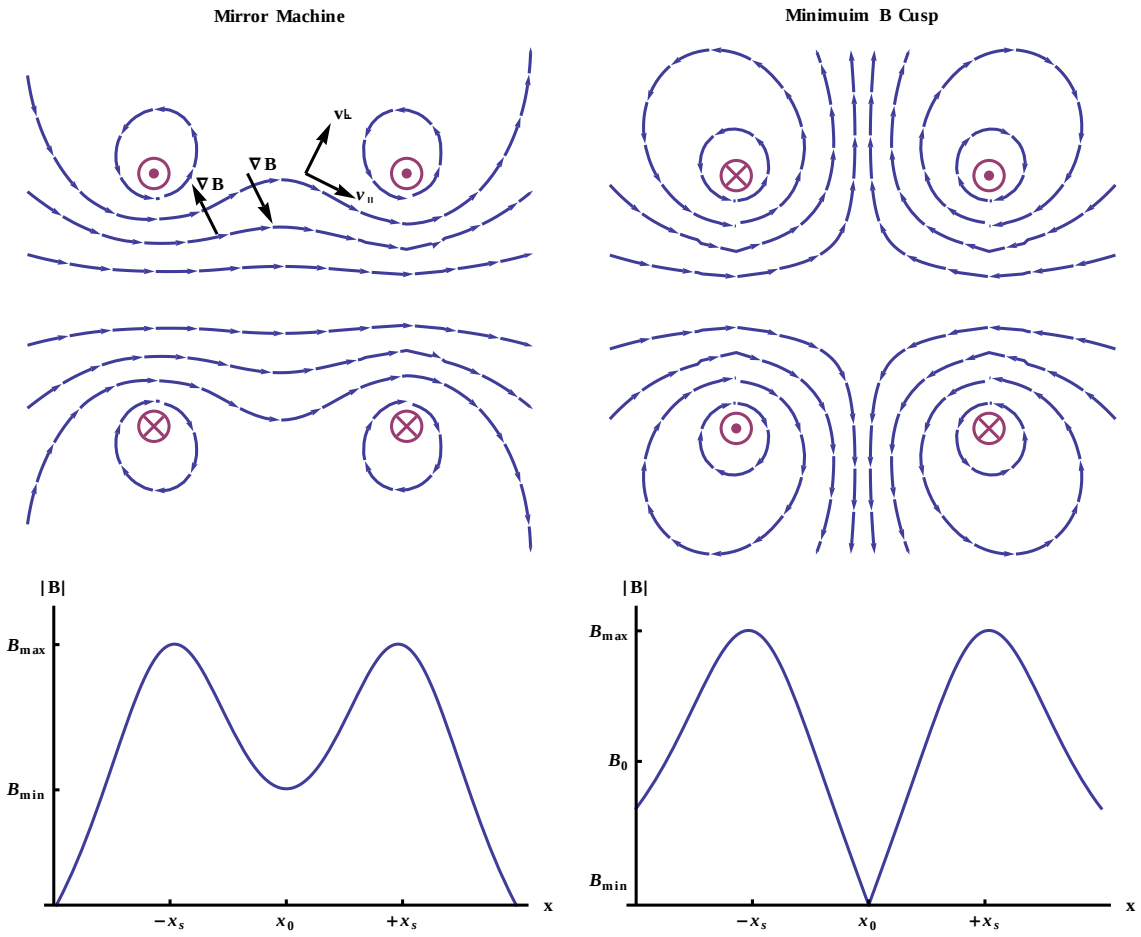


Figure 1.4: The two main open magnetic field confinement geometries [47]. On the left is the simplest magnetic mirror geometry known as the mirror machine, constructed from two solenoidal coils centred on the cylindrical symmetry axis. Both coils have currents running parallel to each other in the same direction. The direction of the field gradient, $\nabla B$, is indicated for the two important field locations, near the coils and near the middle of the device. The coordinates used in the derivation of the magnetic mirror effect, $v_{\|}$ and $v_{\perp}$, are indicated. Directly below the plot of the mirror machine field lines is a plot of the magnitude of the field, $|B|$, along the cylindrical axis. The important locations of the field $B_{max}$ and $B_{min}$ are marked. On the right is a plot of the related open field geometry, the minimum B cusp, which has a very similar construction except that the magnetic fields in the two coils now oppose each other. The resulting cusped field structure is more MHD stable than the mirror machine because of its favourable field gradient orientation. See text for more details.

significant to know whether a given particle will be reflected at all, rather than knowing where exactly along a fieldline the reflection will take place. Therefore, we can divide the velocity space into the trajectory confinement classes by considering the extreme case of a particle that is exposed to the full magnetic field gradient (i.e. from $x_0$ to $x_{max}$) and is reflected when $v_{\parallel}(x_{max}) = 0$. These values are substituted into equations 1.6 and 1.7 to give

$$v_{\perp}(x_0) = \pm \left( \frac{B_{max}}{B_{min}} - 1 \right)^{-1/2} v_{\parallel}(x_0). \tag{1.8}$$

which defines a straight line through the origin. Since velocity space is actually 3D rather than 2D, this line is revolved around the cylindrically symmetric $v_{\parallel}$ axis to define a cone. Any particle with $v_{\parallel}$ and $v_{\perp}$ components inside the cone are not reflected, and hence this region is known as the loss cone [47]. The loss cone concept can be applied to any confinement device that has a magnetic field gradient (e.g. banana orbits in tokamaks). The angle of the loss cone at the device centre can be related to the magnetic field change over a transit,

$$\alpha_{LC}(x_0) = \sin^{-1} \left( \sqrt{\frac{B_{min}}{B_{max}}} \right). \tag{1.9}$$

For the simple mirror machine configuration in Figure 1.4 the particles in the loss cone are lost immediately. The remaining particles are confined to drift along magnetic flux surfaces, which are the surfaces of the field lines revolved around the symmetry axis. In principle, if the flux surfaces do not intersect with any wall material single particles can be confined in the mirror machine indefinitely.

But when considering a bulk plasma, coulomb collisions will scatter the particles through velocity space, effectively randomising their magnetic moments. Overtime particles will be scattered into the loss cone and eventually leave the system. This makes the choice of design parameters critical to ensure that the loss rate is kept low and there have been many schemes which attempt to "plug" the holes in the loss cones[55].

This, however, is still insufficient to make the mirror machine into a practical fusion reactor. This field configuration is unstable to flute instabilities which seriously degrade the confinement properties. The black arrows in Figure 1.4 show the direction of the magnetic field gradient $\nabla B$ when near the coils and near the centre of the device. In normal MHD stable conditions the kinetic plasma pressure $p$ is balanced by the magnetic pressure $B^2/2\mu_0$. Near the coils the plasma is confined on the low side of outermost magnetic field line. If there is a small perturbation outwards across the field line, the magnetic field is now higher and hence the higher magnetic pressure force restores the plasma to its stable confinement mode. However, the field gradient is inverted near the device centre and a perturbation in this region results in a decrease in the balancing magnetic pressure force and feedback can lead to a rapid growth of the instability.

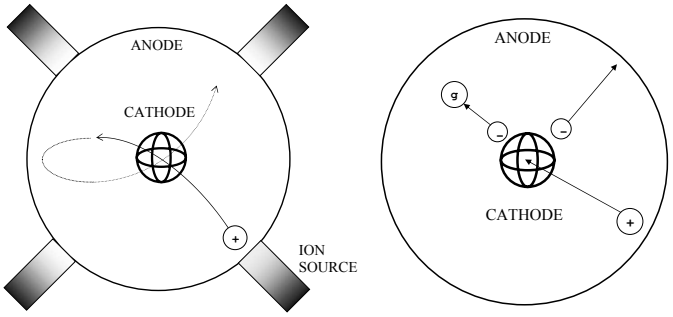


Figure 1.5: Some gridded IEC devices. Reproduced from [25]

### Cusps and Minimum B wells

The flute instabilities that present many technical challenges for the mirror machine can be overcome by creating a "minimum-B" configuration where the field lines are everywhere concave to the plasma [56–58]. Examples of this configuration include the Joffee bars [42, 1] and the simple cusp created by two opposing current loops (Figure 1.4). The mirror effect still applies to these devices even though the magnetic field $B \to 0$ in the null at the centre. Because of the magnetic null, the magnetic moment is no longer a constant of motion and is instead randomised every time a particle passes through the null. This effectively means that no particle can be confined indefinitely in a cusp field. Although these configurations are MHD stable, the loss cones are actually larger because of an additionally created linear loss region in the centre plane. Again, many schemes have been applied but none have managed to make a cusp system sufficiently efficient for fusion power applications [42, 1].

## 1.3 Inertial Electrostatic Confinement

Inertial Electrostatic Confinement (IEC) is a purely electric design that relies on spherically symmetric electric fields to inertially confine and accelerate ions to thermonuclear energies [19–21, 23, 24, 29]. Some example devices are shown in Figure 1.5. Typically, the device consists of two spherically concentric electrodes with the outer electrode being the chamber itself at ground potential. A gridded inner electrode is floated to a high negative potential which creates a radial electric field, effectively acting as a potential well. Positive ions that are created in the device are accelerated down the potential well and converge on the centre of the device at fusion energies.

A portion of the ions arriving at the centre of the device will undergo fusion reactions. The remaining ions are scattered by the well and pass outside the grid where again they see the potential well, and are reflected back into the core of the device. These ions are known as the recirculating current since they can recirculate around the device until they eventually undergo a fusion reaction or collide with the grid itself and remove energy from the system.

IEC systems offer a number of key advantages over mainstream magnetic confinement fusion schemes. Three particular advantages stand out in making IEC research relevant and attractive:

- **Plasma Heating** - acceleration of the ions by the electric field makes it easy to attain the temperatures needed for fusion. Magnetic confinement schemes require techniques such as Neutral Beam Injection (NBI), RF power and Electron Cyclotron Resonance (ECRH) to head the plasma. These technologies can greatly complicate the overall system design and fundamentally limit the scale of economical fusion operation. By comparison, the ideal cross-section energies of 10-100 eV can easily be produced through an IEC system with comparatively simple equipment.

- **Stability** - non-neutral plasmas are inherently more stable since the electric forces inside the plasma tend to stabilise against perturbations. IEC based systems tend to be exposed to a much narrower range of instabilities and hence it might be possible to avoid some of the major instability issues encountered in D-T Tokamak designs.

- **Size and Portability** - IEC designs are typically much smaller than any existing magnetic confinement device. The infrastructure costs associated with IEC are much smaller in low neutron output applications. Hence IEC devices can be used in many non-electric applications of fusion that are currently inaccessible to tokamak devices. Some of these applications are covered in Section 1.4.5.

Gridded IEC devices can achieve typical steady state D-D neutron outputs of $10^6$ - $10^8$ neutrons per second and is actively pursued in both the US [28, 31, 32, 41] and Japan [30, 34]. The outputs already being achieved are suitable for many non-power fusion applications. However it is currently unlikely that gridded IEC systems will ever become a practical device for fusion power output due to the following reasons. Because the fusion cross-section is low when compared with the coulomb collision cross-section, a very high recirculation current is needed to ensure sufficient numbers of ions undergo fusion for a net energy gain to be produced. However, because no grid is 100% transparent to ion collisions, most ions are more likely to be lost in a grid collision long before they undergo a fusion event. Therefore, the major disadvantage of gridded IEC designs is that they suffer substantial energy loss rates through ion collisions with the metal grid. Additionally, ion collisions can either destroy the grid completely, or raise the grid temperature to levels impractical for steady state fusion operation.

The development of an IEC device relevant to fusion energy applications is largely dependant on solving this grid transparency issue. One of best solutions developed so far is the idea of a virtual cathode where an electron plasma is confined to produce a region of negative space charge which in turn confines the ions [19, 23]. The virtual cathode aims to solve the problems of gridded IEC by making the confinement mechanism 100% transparent to the confined energetic ions. The ion recirculation current in a virtual cathode would be correspondingly larger because of the lack of grid collisions, and hence the resulting increase in confinement time leads to a higher probability of a fusion event occurring before an ion is lost. An increase in the ion confinement time improves the device efficiency and might eliminate the principle barrier to practical fusion in an IEC device. The Polywell is one such device that aims to address this issue through the use of a virtual cathode.

## 1.4 The Polywell

### 1.4.1 The Key Concepts - a Hybrid Device

The Polywell concept [68, 69, 77, 80, 81, 87, 88] is a hybrid device that uniquely combines ideas from both cusped magnetic confinement fusion [56, 58] and IEC devices [19, 24, 29]. The concept was invented by Robert Bussard as a magnetic Spherically Convergent Ion Focus (SCIF) device and has been patented three times[65, 70, 73]. The device aims to create a virtual cathode by magnetically confining electrons in a quasi spherical cusp magnetic field [80].

Electrons are injected into the Polywell at high energy and are confined by the cusped magnetic field through the magnetic mirror effect. The confined electrons produce a region of negative space charge which creates a potential well of sufficient depth to accelerate ions to fusion relevant energies. Continual injection of electrons ensures that the system remains electrically non-neutral and balances the loss of electrons escaping from the cusp field. The magnetic field needed to confine energetic electrons is much less than the corresponding field needed for confinement of energetic ions because of their vastly different masses. Hence the aim of a Polywell device is to transfer the problem of energetic ion confinement to that of electron energy loss through transport across field lines. To produce net power output, the power required to maintain the virtual cathode must be less than the fusion power produced by the converging ions.

#### Cusp Confinement and the Wiffle Ball Mode

The unique magnetic field configuration of the Polywell is created by pairs of opposing current loops, each creating a cusp (see Figure 1.6). In the cube configuration each pair of cusps is centred on a Cartesian axis such that each coil sits on a face of the cube. The opposing contributions from each coil cancel out in the centre of the device creating a magnetic null point. The resulting field acts like a magnetic well and contains a combination of point and line cusps.

By using a virtual cathode there is no longer a loss surface embedded within the plasma. The outer grid that contains the magnetic field coils is effectively isolated by the magnetic field it creates [69]. The field lines loop around the coils and will deflect electrons from direct collisions with the magnetic grid. Instead they will recirculate around the device core through mirror effect collisions until they eventually escape the device. In this configuration, the electron population is confined by the magnetic mirror effect with a reflection coefficient $\propto 1/B$ [69, 43, 55].

However, the electron confinement can be further improved over normal cusp confinement by increasing the electron density such that a high $\beta$ condition is reached, where $\beta = p_e/p_m$ is the ratio of plasma kinetic pressure, $p_e$, to the vacuum magnetic field pressure $p_m$.

$$\beta = \frac{p_e}{B/2\mu_0} \tag{1.10}$$

Near the $\beta = 1$ condition, the collective diamagnetic effect of the confined electrons is to exclude the magnetic field from the cusp interior such that a well defined sheath is formed, separating the high field exterior from the interior region [64]. The diamagnetic effect distorts the magnetic field

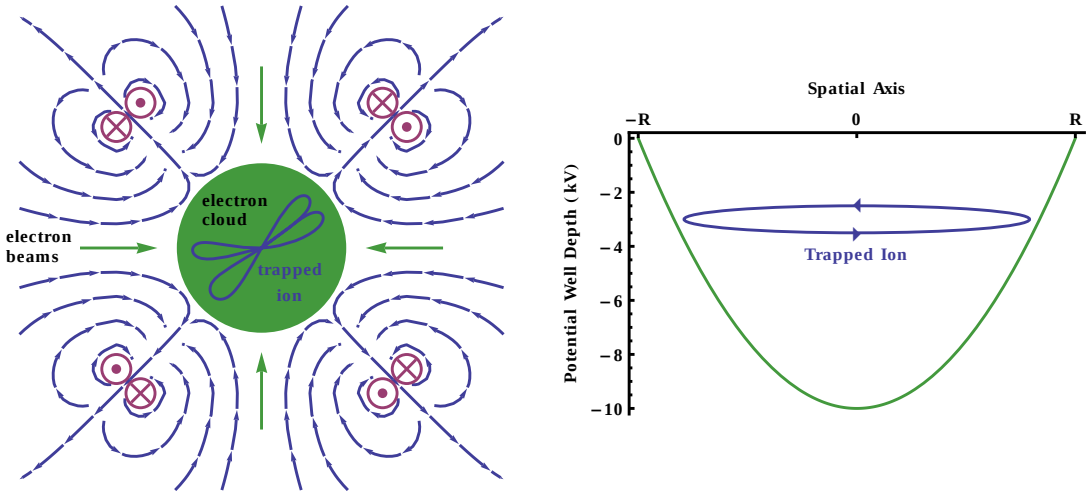


Figure 1.6: A high level view of the Polywell concept [80]. On the left is a plot of the Polywell magnetic field, which is closely related to the biconic cusp field in Figure 1.4. The Polywell magnetic field is created through six pairs of coils, each centred on the face of a cube. Shown in the figure is a slice through the $x - y$ plane of the coils, and hence only four of the coils can be seen. Each pair of coils are in opposition to create a three dimensional point cusp system (covered in Chapter 2). Electrons are injected into the cusped field through the coil faces where they are confined initially through mirror reflection and form a virtual cathode. The build up of negative space charge results in a deep potential well which can in turn trap ions. An illustration of the potential well is shown on the right side of this figure.

in the cusps such that a smaller loss area is presented to electrons inside the device, creating a quasi-spherical magnetic field, known as the "Wiffle Ball" (WB) [69]. Magnetic Mirror reflection still occurs in the cusps but the WB effect adds additional reflection effects such that the cusp reflection coefficient becomes $\propto 1/B^2$ [67]. However, experimental evidence for the WB mode is yet to be published.

The cusp geometry utilised in the Polywell is known to be inherently magnetohydrodynamically stable because the field lines are everywhere convex toward the plasma [49, 51]. However it may not be immune to kinetic instabilities such as the loss cone instability or two-stream instability. The dominate energy loss mechanism is anticipated to be collisional scattering and direct propagation of electrons through the confining cusps.

The plasma in the Polywell is required to be far from thermal equilibrium and at a minimum the ion velocity distribution must be far from Maxwellian[80]. Electron orbits must be dominated by cusp confinement and constrained to a small volume within the device. By contrast, ion orbits should be comparable to the device size such that their motion is dominated by the electrostatic potential well created by the electrons. The fusion products are more energetic than the fuel ions, and are also heavier in mass. Hence the fusion products are expected to have orbits larger than the device and easily escape the cusp field. Because the fusion products do not deposit their energy into the Polywell plasma, the Polywell cannot achieve ignition. Instead the Polywell is more analogous to a power amplifier ($P_{electric}$ in gives $P_{fusion}$ out) [66]. For reactions in which the fusion products are also charged ions, direct conversion of charged particle energy to electricity is an attractive method of extracting the fusion power[80].

### Power Losses and Fusion Power Density

Synchrotron radiation is potentially a significant power loss mechanism in any confinement system that utilises magnetic fields and charged particles. In the case of the Polywell, the ion contribution to Synchrotron radiation is expected to be negligible because the ions are at their lowest energy when the magnetic field is highest, and vice versa [68]. For electrons the situation is reversed, and hence the electron population is expected to emit Synchrotron radiation at the edge of the electron plasma in the high beta region. However, because this emission region is small compared to the overall size of the device, Synchrotron losses are small compared to the power injected into the system and hence can be neglected [68].

Bremsstrahlung is a similar radiation loss mechanism, and predominantly originates from the acceleration of electrons by ions. Unlike Synchrotron radiation, Bremsstrahlung cannot be neglected and is expected to be a significant factor in determining whether or not the Polywell can break even. Electron-ion Bremsstrahlung is largest in the device centre where the densities of both species are highest. The ratio of Bremsstrahlung to fusion power determines the minimum electrostatic well depth required for fusion power to exceed Bremsstrahlung losses.

Just as is the case for Tokamak confinement systems [16], the upper limit of confined fusion particle density is governed by the pressure balance $\beta$, which in the case of the Polywell is the

$\beta = 1$ condition [72]. To maintain magnetic pressure balance, the electron density limit becomes

$$\beta B^2 = n_e E_e \tag{1.11}$$

where $n_e$ is the electron density and $E_e$ is the electron injection energy. To maintain non-neutrality and sustain the electrostatic potential well, only a small difference in the species densities is required and hence $n_e \approx n_i$, where $n_i$ is the ion density at the device edge. Furthermore, because ions move radially in the potential well, the ion density varies $\propto 1/r^2$ as ions converge on the core at the device centre with core radius $r_c$ expressed as a fraction of the device radius $R_d$, $< r_c >= r_c/R_d$. Therefore the ion density in the core can be written as $n_c = n_e / < r_c >^2$ [72]. In fusion systems where the reactants are the same species and approximately monoenergetic, the fusion power is proportional to the reactant density squared and the reaction volume. The reaction volume scales as $V_c \propto r_c^3 \propto < r_c >^3 R_d^3$ and therefore the fusion power scaling can be approximated as

$$P_{fusion} \propto n_c^2 < r_c >^3 R_d^3 \propto \frac{\beta^2 B^4 R_d^3}{< r_c >}, \tag{1.12}$$

which gives the same approximate fusion power scaling as a neutral maxwellian plasma confined in a Tokamak magnetic field geometry [16]. Therefore a Polywell would be an attractive design for commercial fusion power applications if its base system size can be made smaller than that currently needed for DEMO, the first anticipated commercial Tokamak design.

This analysis highlights the difference between the closed toroidal confinement schemes and the Polywell design. The toroidal systems confine neutral fusion plasmas with magnetic pressure, with loss rates governed by ion transport. In contrast, the Polywell uses magnetic pressure to confine the high energy injected electrons at the device surface, with the electron energy being converted to ion energy in the device core. The ratio of typical magnetic pressures in the two different confinement schemes is approximately equal to $\sqrt{m_e/m_i}$, the square root of the ratio of electron to ion masses [72]. Because electron confinement generally requires a lower magnetic pressure than that for an equivalent neutral plasma, the inherent technology levels required (i.e. superconducting coils VS water cooled copper wires) are expected to be lower [72].

### 1.4.2 Experimental Polywells

The majority of experimental Polywell research has been undertaken by one company, EMC2, that has a non-disclosure IP protection policy and, therefore, any of their experimental results are usually only published in non-peer reviewed internal reports. Consequently, this section will only summarise some of the key results from work that has been published in the peer reviewed literature. In addition, this review will not cover any current research work being carried out commercially (for example, WB7 and WB8).

Between 1994 and 2006 at least 10 different experimental Polywell designs were constructed by Robert Bussard's research company, EMC2 [69, 75]. The experimental parameters for a subset of the devices is presented in Table 1.2. The first Polywell built, HEPS, was built in conjunction

| Device | $R_d$ | $B_{face}$ | $E_{inj}$ | $I_{inj}$ | Notes |
|---|---|---|---|---|---|
| HEPS | 93 cm | 0.35 T | 15 keV | 5-10 A | closed box configuration |
| PZLx-1 | 3 cm | 3.5 T | 15 keV | 10 A | hydromagnetic stability tests |
| WB1 | 5 cm | 0.08 T | 1-2 keV | 4-5 A | solid state magnets → big line cusps |
| WB2 | 5 cm | 0.13 T | 1-2 keV | 4 A | copper coils, cusp confinement study |
| WB3 | 10 cm | 0.24 T | 15 keV | 3 A | larger version of WB3 |
| WB4 | 15 cm | 0.5 T | 15-30 keV | 2-4 A | $10^6$ n/s |
| WB6 | 15 cm | 0.13 T | 12.5 keV | 40 A | $10^9$ n/s, $s \approx 1.4$, conformal coil formers |

Table 1.2: The parameters of a subset of EMC2's experimental Polywell devices, where $R_d$ is the device radius and $B_{face}$ is the peak magnetic field in the the coil face. $E_{inj}$ and $I_{inj}$ are the injected electron energy and current respectively. All parameters are only sample data points taken from available publications [67, 69, 81].

with DARPA and is the largest device built to date with the highest power input. The device demonstrated deep potential wells of up to 10 keV, at 80% of the injected electron energy [81]. However the device used a closed box configuration which meant that the metal surfaces in the corners and coil faces were not magnetically isolated and hence acted as collectors leading to higher electron losses than expected.

The early WB devices experimented with electron trapping in a number of different cusped magnetic field designs with varying degrees of success. WB1 used permanent annulus magnets, and thus had large linear line cusps exhibiting losses similar to the line cusps of the biconic spindle cusp [69]. This resulted in large electron losses but demonstrated basic electron trapping.

WB2-4 all used copper wire coils for creating the magnetic field and featured open coil faces and corners, allowing recirculation of the electron current without large metal loss surfaces. These devices were used to study potential well formation and the changes in cusp confinement with varying magnetic field intensity and drive conditions [69]. These machines also demonstrated that the machine itself could act as an electron extraction grid from electron sources located on the cusp axes. PZLx-1 was designed to prove the hydromagnetic stability of a plasma in a cusped magnetic field, derived theoretically by Berkowitz [49, 51].

WB5 was another closed box design with the magnet coils mounted on the exterior of the vacuum chamber. The experimental design resulted in excessive electron losses to the uninsulated metal surfaces. Floating ceramic repeller plates were used to plug some of the line cusps and resulted in reduced electron losses by a factor of 2.5, but consequently led to an increase in the ion loss rate [69]. This is because in electric confinement schemes, modifications to improve the confinement of one species with an electric field tend to decrease the confinement of the other species.

WB6 was the final machine employing all the best features of the previous devices. It was an uncooled, pulsed coil device, producing peak magnetic fields of 0.13 T in the coil faces. Electrons were injected at energies of 12.5 keV with a current of up to 40 A. These conditions produced

potential wells as deep as 10 kV. The coil formers were toroidal to be conformal with the coils magnetic field and magnetically insulate the biased grid. Additionally, the Polywell structure minimised any connecting metal surfaces that could act as loss surfaces for electrons, instead allowing for a high degree of recirculation around the device. This design resulted in a high grid transparency and hence improved overall electron confinement. The research with WB6 culminated in a claimed neutron count of $10^9$ n/s [69], but ultimately the device was destroyed through a coil shorting event that resulted in a destructive failure of the structure.

### 1.4.3 PIC Simulations

Particle In Cell (PIC) simulations have been carried out by Rogers [82–85] and Kazemyzade [79] with the commercial OOPIC package [2, 3, 17]. Rogers has simulated potential well formation as a function of injected electron and ion current as well as magnetic field strength [84, 85]. Potential well formation has been simulated with a number of different fuel combinations including D-D and p-$^{11}$B (discussed in section 1.4.4), with simulations showing deep potential wells ∼80% of the Polywell bias can be achieved, supporting the experimental claims of Bussard and Krall [81]. Rogers has done a simulation of the break-even radius of a p-$^{11}$B Polywell finding the required $R_d > 6.6$ m [82]. Rogers has also performed a conceptual design study for a US$250k D-D experimental Polywell with an $R_d \simeq 25$ cm (50 cm diameter device) [83].

Kazemyzade et. al. [79] have used OOPIC to simulate a D-D Polywell and considered the variation in potential well depth with increasing magnetic intensity. By considering two case studies they showed that increasing the magnetic field can actually lead to a decrease in the overall potential well depth. It is conjectured that this phenomena occurred because the increase in magnetic field led to an increase in the electron dwell time that subsequently led to greater ion confinement. Although improved ion confinement is desired for Polywell fusion, increasing the ion confinement beyond the limit required for maintaining non-neutrality will greatly reduce the depth of the potential well. Thus, the simulations demonstrated the need to balance the magnetic field intensity with other device parameters such as injected electron and ion current [79].

### 1.4.4 Advanced Fuels

A number of advanced fuels are aneutronic, that is they do not produce neutrons. The D-D and D-T reactions in Table 1.1 are the most studied because their reaction cross-sections occur at much lower energies than the advanced fuels shown in Table 1.3. D-D and D-T reactions are generally considered the first generation fusion fuels because of the difficulties in heating fusion plasmas to the energies required for using advanced fuels [111]. In the long term, it would be better to switch to advanced aneutronic fuels, eliminating issues associated with neutron radiation damage such as neutron activation of structural materials, biological shielding and remote handling.

Additionally, advanced fuels have the potential to utilise direct energy conversion [112–114, 116]. The bulk of the energy produced in the fusion of advanced fuels is carried away in

| |
|---|
| $D + {}^3He \rightarrow {}^4He(3.6MeV) + p(14.7MeV)$ |
| $p + {}^{11}B \rightarrow 3{}^4He + \gamma(8.7MeV)$ |
| $D + {}^6Li \rightarrow 2{}^4He + \gamma(22.4MeV)$ |
| $p + {}^6Li \rightarrow {}^4He(1.7MeV) + {}^3He(2.3MeV)$ |
| ${}^3He + {}^6Li \rightarrow 2{}^4He + p + \gamma(16.9MeV)$ |
| ${}^3He + {}^3He \rightarrow {}^4He + 2p + \gamma(12.9MeV)$ |
| $p + {}^7Li \rightarrow 2{}^4He + \gamma(17.2MeV)$ |
| $p + {}^{15}N \rightarrow {}^{12}C + {}^4He + \gamma(5.0MeV)$ |

Table 1.3: Some advanced fuel fusion reactions.

the kinetic energy of charged product particles instead of neutrons. Direct energy conversion schemes involve directly extracting the kinetic energy of the products, such as making them do work against an electric field[113, 114].

These techniques could result in unprecedented gains in efficiency of energy conversion, and a substantial reduction in the infrastructure setup costs [110, 114, 115]. D-T fusion neutrons require a traditional thermal cycle to boil water and produce steam which subsequently does work on a turbine. Preliminary studies show direct energy conversion technologies could be significantly cheaper than the infrastructure required for a thermal cycle.

The Polywell is uniquely able to utilise advanced fuels for two reasons. First because heating the plasma ions to the high temperatures needed is trivially achieved by scaling up the accelerating potential well depth [68]. Toroidal magnetic confinement schemes are primarily limited to operating with D-T fuels because of the current limitations on heating with Neutron Beam Injection (NBI) techniques (and more importantly, due to the larger Bremsstrahlung losses at higher maxwellian temperatures). Although the heating with NBI and other techniques may become less technically challenging in the future, it is unlikely to be as simple as it is in the Polywell.

Second, the relative scale of charged particle orbits in the Polywell is determined by their charge to mass ratio. If for a given magnetic field strength the reactant ions have orbits on the scale of the device size, the product ions have orbits much larger than the device because of their high energy and easily escape from the confining cusp field [80]. They will not deposit their energy in the plasma and hence the Polywell is not an ignition device.

### 1.4.5 Non-electrical Applications of Polywell Fusion Research

Although electricity generation is the primary end goal of fusion research, there are a number of non-electrical applications that are usually overlooked. These other commercial applications may not have the society wide impact that fusion power could have, but they could significantly impact the public image and funding available for fusion [119]. The public image of fusion is low because the promise of fusion has thus far failed to deliver a commercial power plant after 60

years of research.

Commercial applications can improve the public image of fusion and also inject funding and investment from the private sector into small scale projects with realistic near-term outcomes [117]. In this way it may be possible to build up momentum and continued public support for fusion energy research through ITER and DEMO [118, 124]. Studies by the University of Wisconsin IEC group identified five unique products that fusion plasmas can sell to the commercial sector [119–122] :

- high energy neutrons (2-14 MeV)
- thermal neutrons
- high energy protons (3-15 MeV)
- electromagnetic radiation (microwave to x-rays to $\gamma$ rays)
- high energy electrons coupled with photons to provide ultrahigh heat fluxes.

Neutron sources are likely to be the quickest technologies to market because some of the applications require neutron rates on slightly higher than currently produced. Some applications of neutron sources include the production of radio isotopes for medical imaging and cancer treatments [123], the destruction of long lived fission products [119], and the detection of landmines and other explosives[119].

## 1.5 Criticism of the Polywell Concept

A number of critique's of the Polywell IEC have emerged and a few of the most significant criticisms will be briefly reviewed. The three concepts that are challenged the most are ion/electron thermalisation, ion core convergence, and the degree of electron losses through the point cusps.

### 1.5.1 Ion Thermalisation

The Polywell device requires the ion distribution function to be approximately monoenergetic to take advantage of the resonances in the fusion cross-section for maximising $P_{fusion}/P_{brem}$. Both Nevins [33] and Rider [35–37] have examined the Polywell concept and concluded it will not be possible to maintain a monoenergetic ion distribution long enough for a significant portion of the ion population to undergo fusion before relaxation to a maxwellian.

Rider has modified the Spitzer ion-electron energy transfer rate for the case when the ion temperature $T_i$ is significantly higher than the electron temperature $T_e$, and found that as $T_i/T_e$ increases the heat transfer rate decreases to around 60-80% of its classical value [37]. Rider goes on to conclude that "since the ion distributions are essentially Maxwellian and the ion-electron heat transfer rate is not greatly modified from the Spitzer value, one will obtain results already familiar for other fusion reactors" [35]. The resulting Bremsstrahlung radiation losses prevent

net energy production in all fuels except D-T, D-D, and D-$^3$He. Hence, Rider concludes that passive methods of maintaining non-equilibrium are inadequate unless one uses active external cooling/heating [35].

Rider has also investigated ways of actively maintaining a monoenergetic non-equilibrium distribution [36]. Due to coulomb collisions, a certain number of particles $n_{fast}$ will gain an amount of energy $\Delta E_{fast}$ on a timescale $t_{fast}$. To keep the energy distribution monoenergetic, the excess energy of the $n_{fast}$ particles gained in collisions must be extracted and given to particles that were collisionaly down-scattered, which is defined as the recirculating power $P_{recirc}$. Rider shows that $P_{recirc}$ is always $> P_{fus}$, and therefore, on the basis that such a mechanism for power recirculation will never be 100% efficient, break even with advanced fuels is not possible [36]. Nevins has made similar conclusions [33].

However these results directly contradict the analysis of Rosenberg and Krall [86], who showed that when the ions are able to transit the device in a single collision time two body collisions can actually passively maintain a non-maxwellian ion-velocity distribution. They showed that collisions in the edge layer can maintain a non-maxwellian distribution in the device interior on time scales longer than the small angle scattering time, which would normally have been sufficient to produce a local maxwellian. If this effect can be experimentally proven it would allow the Polywell to passively maintain non-equilibrium.

### 1.5.2 Core Convergence and Ion Defocusing

Dolan has questioned the degree of ion focusing possible in the Polywell, and the attainable core convergence radius [76]. As the electron density increases, electron diamagnetic currents push the magnetic surfaces outwards producing a sharp magnetic boundary. Dolan argued that since electrons flow easily along field lines, the variation of electrostatic potential along field lines is relatively gradual. Contours of electrostatic potential would tend to be similar to those of the magnetic flux surfaces. As ions leave the central core, they would be reflected from the convex boundary layer which could increase the core focus radius $r_c$.

Bussard argues that this analysis is incorrect because ions approaching the edge region are at lower energy than in the core due to climbing up the potential well [71]. At the edge, collisions isopotrize the ions but their energies remain the same. Thus the only way ions can acquire transverse momentum and continuously defocus the core is through core maxwellianisation and energy upscattering, which spread the edge region and reduce isopotrization. However this would only be a problem if the ion lifetime is too long. Furthermore, Bussard has argued that it is incorrect to assert that equipotential lines will follow the magnetic field lines because electrons are not confined to field lines as in other magnetic confinement systems because of the magnetic null region [71]. Therefore, the degree of attainable ion focusing will be related to the sphericity of the electrostatic equipotential surfaces[78].

### 1.5.3 Electron Cusp Losses

The electron loss rate essentially determines the power balance of a Polywell reactor. A number of previously explored cusped systems have exhibited a cusp leakage loss rate that is not significantly better than that of the biconic spindle cusp, and hence probably not useful for a break even fusion reactor [42, 60, 62]. For the Polywell to be competitive it must be able to produce a cusp leakage rate substantially lower than other cusped fusion devices. Theoretically it is claimed that the Polywell can outperform existing cusp devices through the use of diamagnetic effects [69, 80] and space charge plugging [77]. Experimental verification of these ideas is necessary for the Polywell to become an attractive concept for further fusion research.

## 1.6 Aims of the Thesis

This thesis aims to characterise and measure potential well formation in a low beta Polywell, and study its relationship to the magnetic field structure. Chapter 2 will explore the characteristics of the fundamental underlying vacuum magnetic field. We will examine how the magnetic field structure changes with coil current, radius and coil spacing, such that we can build on these relationships to formulate a general model for low beta confinement in a Polywell. We will also explore the symmetry between confinement behaviour in a magnetic spindle cusp and the Polywell such that the Polywell can be modelled as a series of point cusps. The ultimate goal is that by understanding confinement in low beta operation, future researchers can extend the model into the $\beta = 1$ case and thus answer questions about electron losses from the magnetic cusps, which will ultimately determine if the Polywell can be a useful fusion device.

Chapter 3 will describe the experiment equipment and methods used in the subsequent chapters. The first experimental device is discussed in Chapter 4 and aims to obtain at least qualitative validity of the Polywell concept in establishing a potential well. The first Polywell design will test all aspects of the experimental setup such as device construction, power supply construction and integration with the system as well as electron injection. A floating potential probe will be used to measure potential well formation as a function magnetic field strength, background gas pressure and electron injection parameters.

Last, in Chapter 5 we will adapt orbital limited motion theory to obtain a biased Langmuir probe diagnostic that is uniquely designed for operation in a low beta Polywell. The new diagnostic will be used to examine a number of case studies with the aim of showing that the Polywell is operating as intended. The biased probe will aim to measure the spatial profile of the plasma potential and its dependence on a number of experimental parameters such as magnetic field intensity and injected electron energy and current. Developing a unique diagnostic for the Polywell may allow us to answer questions about issues related to thermalisation and electron cusp losses raised by critics of the Polywell.

Chapter 2

# Magnetic Fields

The aim of this chapter is to characterise the spatial structure of the magnetic field as a function of coil current, radius and coil spacing, in such a way that allows a detailed understanding of its underlying confinement properties. The trajectories of single electrons in this field structure will be analysed as representative of the confinement behaviour in a low-beta electron plasma where single particle behaviour may dominate. This information allows the formation of a general model of confinement in the Polywell including predicted loss rates, and general guidelines for the construction of future experimental devices. Additionally, this model can be compared with other cusp systems as an indicator of relative performance and capability. Lastly, we derive an approximate expression for the magnetic fields in a simplified Polywell system for use in developing a more detailed theory.

## 2.1 Single Current Loops

The full expressions for the magnetic field in the Polywell can be obtained from the superposition of the contributions from each single current loop. Hence it is necessary to start the analysis with the expressions for a single current loop. The derivation of the magnetic field due to a single current loop is shown here for completeness and follows the derivation laid out by Good [50], starting with the Biot-Savart Law [52, 53]

$$\vec{\boldsymbol{B}} = \frac{\mu_0 I}{4\pi} \oint \frac{d\vec{\boldsymbol{l}} \times \vec{\boldsymbol{r}}}{r^3}, \tag{2.1}$$

where $I$ is the current in the loop and $d\vec{\boldsymbol{l}}$ is the differential wire element in the direction of the current. $\vec{\boldsymbol{r}}$ is the displacement vector from the wire element to the point where the field is being calculated. The coordinates for this system are shown in Figure 2.1. The components of $d\vec{\boldsymbol{l}}$ and $\vec{r}$ are found from trigonometry.

For a single current loop centred on the origin of the $z$ axis in cylindrical coordinates, the radial $\rho$ and $z$ axis components of $d\vec{\boldsymbol{l}}$ and $\vec{\boldsymbol{r}}$ are [50]

$$\begin{aligned} d\vec{\boldsymbol{l}} &= a d\vec{\boldsymbol{\phi}} && (2.2)\\ &= -a \sin\phi \, d\phi \, \vec{\hat{\boldsymbol{\rho}}} + a \cos\phi \, d\phi \, \vec{\hat{\boldsymbol{\phi}}} && (2.3)\\ \vec{\boldsymbol{r}} &= (\rho - a\cos\phi)\, \vec{\hat{\boldsymbol{\rho}}} - a \sin\phi \, \vec{\hat{\boldsymbol{\phi}}} + z \, \vec{\hat{\boldsymbol{z}}} && (2.4) \end{aligned}$$

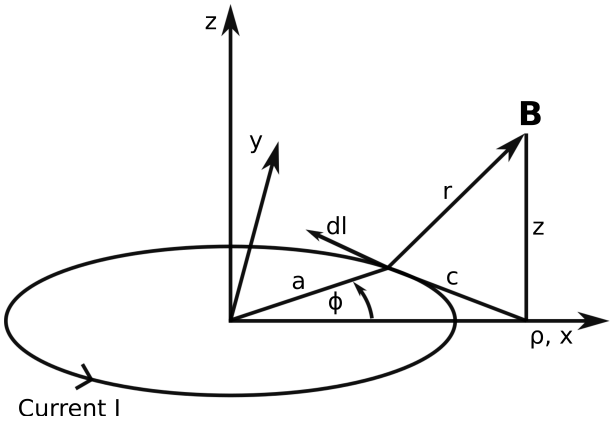


Figure 2.1: The cylindrical coordinate system being used. Redrawn from Good [50].

Using these expressions the cross product term can be evaluated to give

$$d\vec{\boldsymbol{l}} \times \vec{\boldsymbol{r}} = (az\cos\phi)\, d\phi\, \vec{\boldsymbol{\rho}} + az\sin\phi\, d\phi\, \vec{\boldsymbol{\phi}} + (a^2 - a\rho\cos\phi)\, d\phi \vec{\boldsymbol{z}}, \tag{2.5}$$

and therefore we can now split the Biot-Savart Law into three components, one for each coordinate.

$$B_\rho = \frac{2\mu_0 I}{4\pi} \int_0^\pi \frac{az\cos\phi}{(z^2 + a^2 + \rho^2 - 2a\rho\cos\phi)^{3/2}} d\phi \tag{2.6}$$

$$B_\phi = \frac{2\mu_0 I}{4\pi} \int_0^\pi \frac{az\sin\phi}{(z^2 + a^2 + \rho^2 - 2a\rho\cos\phi)^{3/2}} d\phi \tag{2.7}$$

$$B_z = \frac{2\mu_0 I}{4\pi} \int_0^\pi \frac{a^2 - a\rho\cos\phi}{(z^2 + a^2 + \rho^2 - 2a\rho\cos\phi)^{3/2}} d\phi \tag{2.8}$$

Due to the cylindrical symmetry of the single current loop, the $B_\phi$ component must integrate to 0. The other two can be solved using the known elliptical integral identities [50]

$$\int_0^\pi \frac{d\phi}{(b \pm \cos\phi)^{3/2}} = \frac{m}{2 - 2m}\sqrt{2m}E(m) \tag{2.9}$$

$$\int_0^\pi \frac{\pm\cos\phi d\phi}{(b \pm \cos\phi)^{3/2}} = \sqrt{2m}K(m) - \frac{2-m}{2-2m}\sqrt{2m}E(m) \tag{2.10}$$

where $m = \frac{2}{1+b}$. We now use equations (2.9) and (2.10) to find an expression for $B_\rho$.

$$\begin{aligned} B_\rho &= \frac{-\mu_0 I a z}{2\pi} \frac{1}{(2a\rho)^{3/2}} \int_0^\pi \frac{-\cos\phi d\phi}{(b - \cos\phi)^{3/2}} \\ &= \frac{\mu_0 I z}{2\pi}\sqrt{\frac{m}{4a\rho^3}}\left[\frac{2-m}{2-2m}E(m) - K(m)\right] \end{aligned} \tag{2.11}$$

where

$$b = \frac{z^2 + a^2 + \rho^2}{2a\rho} \tag{2.12}$$

$$m = \frac{4a\rho}{z^2 + (a+\rho)^2} \tag{2.13}$$

The integral for $B_z$ evaluates to

$$\begin{aligned} B_z &= \frac{\mu_0 I}{2\pi(2a\rho)^{3/2}}\left[a^2\int_0^\pi \frac{d\phi}{(b-\cos\phi)^{3/2}} - a\rho\int_0^\pi \frac{\cos\phi d\phi}{(b-\cos\phi)^{3/2}}\right] \\ &= \frac{\mu_0 I}{2\pi}\sqrt{\frac{m}{4a\rho^3}}\left[\rho K(m) + \frac{am-\rho(2-m)}{2-2m}E(m)\right]. \end{aligned} \tag{2.14}$$

The functions $E(m)$ and $K(m)$ are the complete Elliptic integrals of the first and second kind respectively, and are only defined for $0 < m < 1$. $m$ is zero on the axis of the coil, and is therefore also zero for all six Polywell coils at the centre of the magnetic well. $m$ goes to 1 in the vicinity of the conducting coil wires.

The total magnetic field at the centre of a coil ($\rho = 0,\ z = 0$) can only be in the z direction due to cylindrical symmetry. Furthermore, the radial component of the magnetic field must always be zero in the plane of the coil, i.e $B_\rho = 0$ at $z = 0$. Both of these limits can be confirmed by applying limit analysis to equations (2.11) and (2.14).

## 2.2 Six Polywell coils

The full magnetic field in the Polywell can be obtained from the superposition of the contributions from each current loop. Since we are neglecting the higher order Polywell geometries and limiting the analysis to the cube configuration we can make further use of the underlying symmetry in the device. Because each Cartesian axis is orthogonal, each pair of loops centred on the same axis will contribute one of the $B_\rho$ or $B_z$ terms in a given Cartesian coordinate, but never both. In a higher order geometry this would not be true and both terms would need to be considered. This can be shown by considering the six loop contributions to the total magnetic field in the $\hat{\boldsymbol{x}}$ coordinate. Each coil has the two field contributions $B_\rho$ and $B_z$, where $B_z$ is now aligned with the axis on which each loop is centred. For the two loops centred on the $\hat{\boldsymbol{x}}$ axis, each loop contributes a $B_z$ term to the total field in the $\hat{\boldsymbol{x}}$ direction. The radial $B_\rho$ components of these two $\hat{\boldsymbol{x}}$ axis loops are always perpendicular to the $\hat{\boldsymbol{x}}$ axis, hence they make no contribution to the total field in the $\hat{\boldsymbol{x}}$ direction.

The four off-axis loops (i.e. the two loop pairs centred on the $\hat{\boldsymbol{y}}$ and $\hat{\boldsymbol{z}}$ axes) have $B_z$ contributions that are always perpendicular to the $\hat{\boldsymbol{x}}$ axis and hence are not included in the $\hat{\boldsymbol{x}}$ direction calculation. However each loop will have a $B_\rho$ contribution to the $\hat{\boldsymbol{x}}$ axis. Consequently, $B_\rho$ must be converted into Cartesian coordinates. For example, the radial coordinate, $\rho_{xz}$, in the $xz$ plane is given by $\rho_{xz} = \sqrt{x^2 + z^2}$ which is used when obtaining the $B_\rho$ contribution due to the loops on the $\hat{\boldsymbol{y}}$ axis. Therefore, in any given coordinate we expect to see two $B_z$ terms

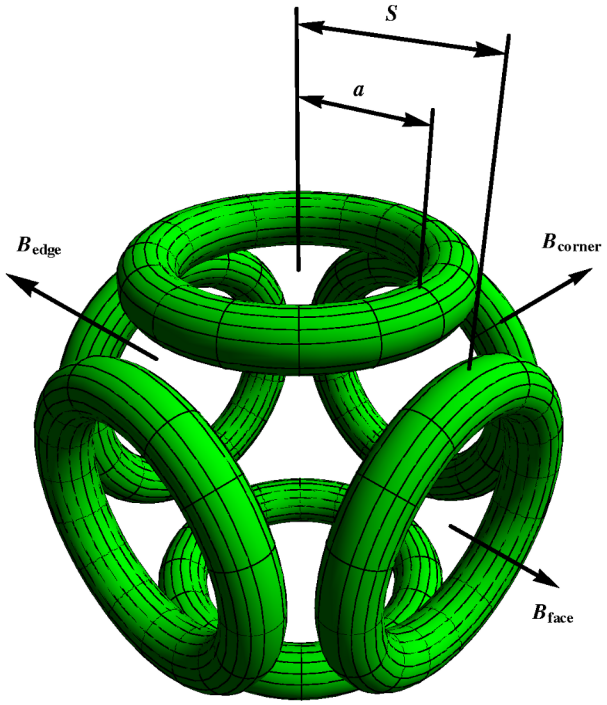


Figure 2.2: A diagram of the cube Polywell configuration. The coil radius $a$ and coil spacing $S$ are marked. Vectors have been used to indicate the positions of the Face, Corner and Edge regions.

from the two loops on the same axis, and four $B_\rho$ terms from the four off axis loops. Thus, the equation for the Polywell field in the $\hat{\boldsymbol{x}}$ direction is

$$\begin{aligned}\vec{\boldsymbol{B}}_{\boldsymbol{x}} = \Bigg( & B_z(\rho_{yz}, x-S) + B_z(\rho_{yz}, x+S) \\ & + B_\rho(\rho_{xz}, y-S)\frac{x}{\rho_{xz}} + B_\rho(\rho_{xz}, y+S)\frac{x}{\rho_{xz}} \\ & + B_\rho(\rho_{xy}, z-S)\frac{x}{\rho_{xy}} + B_\rho(\rho_{xy}, z+S)\frac{x}{\rho_{xy}}\Bigg)\vec{\hat{\boldsymbol{x}}}\end{aligned} \tag{2.15}$$

where $B_z(\rho_{yz}, x-S)$ means the expression for $B_z$ in Equation 2.14, with $\rho_{yz}$ and $x-S$ in place of the $\rho$ and $z$ coordinates respectively. The parameter $S$ is the loop spacing dimension shown in Figure 2.2. The general expression for the overall magnetic field can be expressed as

$$\vec{\boldsymbol{B}} = B_x\vec{\hat{\boldsymbol{i}}} + B_y\vec{\hat{\boldsymbol{j}}} + B_z\vec{\hat{\boldsymbol{k}}} \tag{2.16}$$

where $B_y$ and $B_z$ are generated by cyclically permuting the coordinates in $B_x$, Equation 2.15.

## 2.3 B Field Structure and Single Particle Trajectories

The resultant magnetic field structure consists of field lines that enter through well defined point cusps in the loop faces and leave in the gaps between the loops. The magnetic field lines in the $xy$ plane are shown in Figure 2.3. Note that the magnetic field is everywhere convex towards the centre of the device, making it inherently MHD stable [68]. Figure 2.4 shows the absolute value of $\vec{\boldsymbol{B}}$ in the $xy$ plane, revealing its magnetic well structure. The magnitude of the magnetic field near the null point varies as $r^3$ where $r$ is the radius measured from the magnetic null point.

In principle electrons are confined by reflection from the point cusps if they are outside the loss cone [69]. However the motion is significantly complicated by the presence of the null point, which scatters the electrons' magnetic moment [56]. A sample electron trajectory is shown in Figure 2.5 where the electron is started in the centre of the device. Initially it is reflected from a point cusp in one of the faces but is then scattered around the null region in a chaotic way before eventually returning to its starting point. Figure 2.6 shows the superposition of 10 such trajectories with randomised starting positions and calculated until they leave the cube region defined by the six Polywell loops.

The motion shown in Figures 2.5 and 2.6 is only a slightly more complicated version of the motion in the comparatively simpler biconic cusp. Theories of biconic cusp confinement are based on the hypothesis that there exists a critical flux tube separating an outer region of completely adiabatic orbits from an inner region where every field line passes through a distinctly non-adiabatic region [57, 58, 63]. Orbits guided by magnetic field lines of the latter type consist of segments of adiabatic motion near the reflection points, separated by a non-adiabatic portion

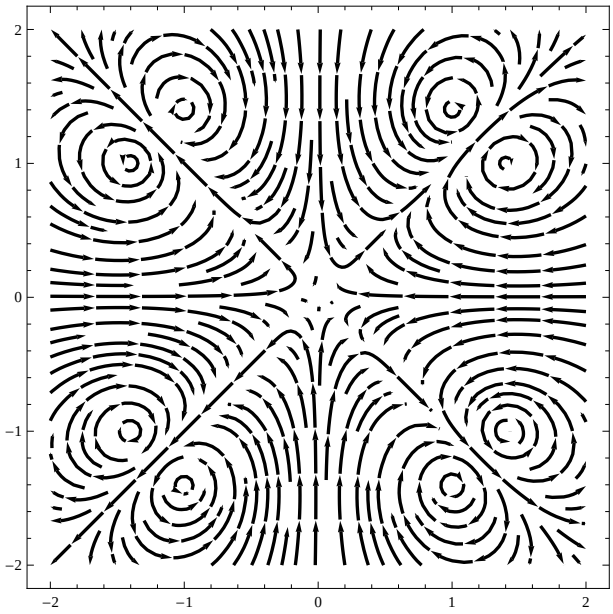


Figure 2.3: The magnetic field lines in the $xy$ plane intersecting four of the six coils. In this plane there are four point cusps, one centred on each coil face. These have been labelled as face cusps. Also present are four line cusps, one in each corner in the spacing between the coil windings. These have been labelled as edge cusps.

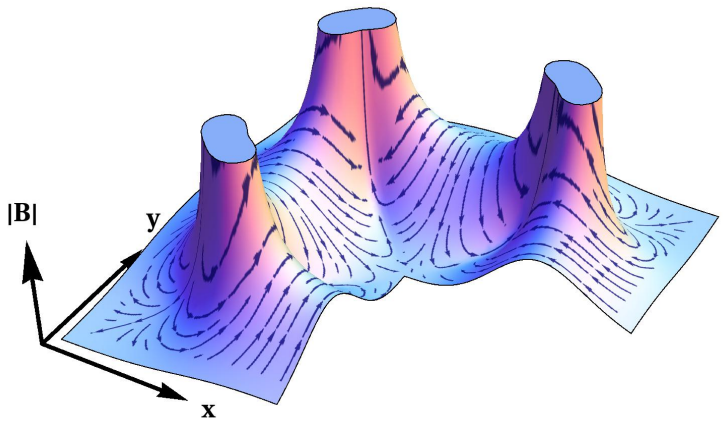


Figure 2.4: The magnitude of the magnetic field in the same $xy$ plane as in Figure 2.3, the magnetic field lines from Figure 2.3 are superimposed over the magnitude plot. It is clear from this structure that the Polywell creates a magnetic well.

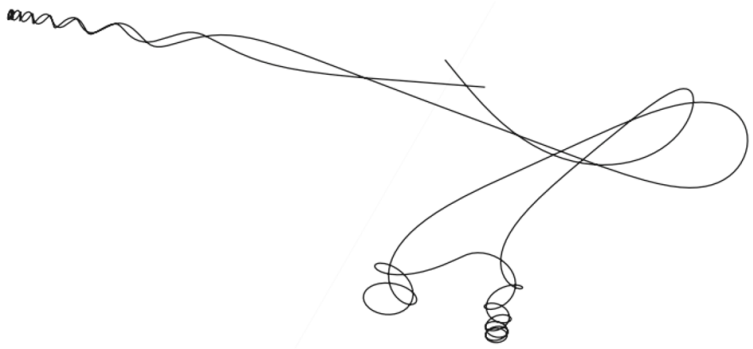

Figure 2.5: A sample isolated electron trajectory. The electron was initialised at the centre of the device with an energy of 100 eV and a randomised velocity vector. The coils are not drawn in the background so as to clarify the different types of motion present. The electron has a clearly defined magnetic moment in three places where it is reflected from a high field region. In the central region it has smoother trajectories.

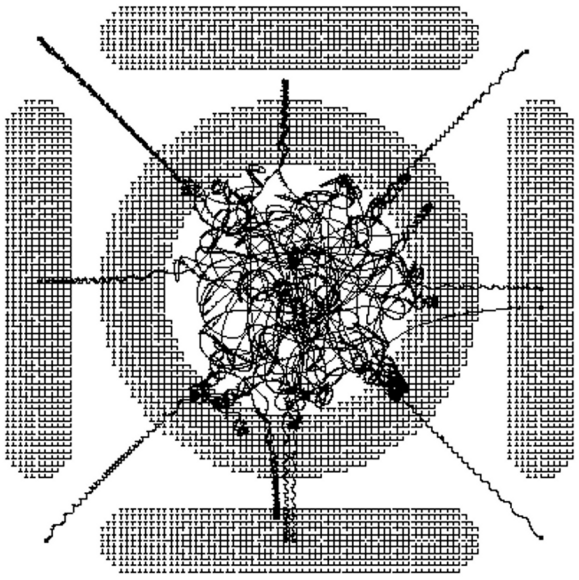

Figure 2.6: A superposition of 10 different electron trajectories. Each electron has a starting energy of 100 eV and a randomised position and directed velocity. The trajectories are plotted until the electrons reach the coil's cube surface, at which point they are considered lost.

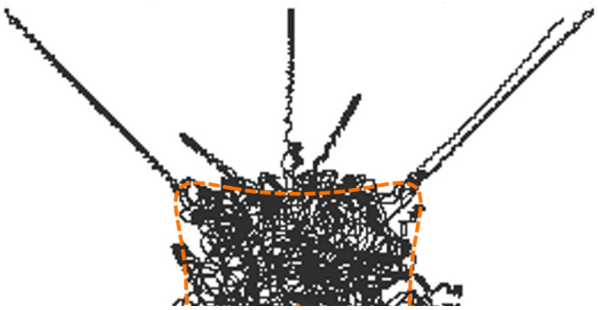

Figure 2.7: A superposition of 10 particles is shown with the magnetic field coils removed for clarity. The contour where the gyroradius is 10% of the device radius is shown in the thick dashed line. This contour approximates the boundary between the adiabatic and non-adiabatic segments of motion.

which randomises the magnetic moment. This hypothesis and the underlying confinement theory derived from it can be extended to apply to the Polywell magnetic field geometry.

The motion of electrons originating in the centre can be understood by examining the behaviour of the electron gyroradius as a function of radius from the central null point. In the vicinity of the null point the gyroradius changes rapidly. Over a distance of half the device radius, the gyroradius $r_g$ can change from $\infty$ to $\approx 1$ cm. This leads to almost straight trajectories in the centre of the magnetic well until the electron is turned around at a region of high field where $r_g$ approaches 10% of the device radius. This region is marked in Figure 2.7.

Electrons will be reflected inside the low field region until they eventually enter a point cusp where the magnetic field is directed radially outwards. As a consequence of this change in field geometry, the electrons follow the field lines out of the device. Additionally, there is a transition to a region where the magnetic field changes slowly compared with the electron gyroradius and the magnetic moment, $\mu$, becomes an adiabatic constant of motion. At this point the electron motion is completely adiabatic and is reflected if the peak magnetic field $B_{peak} >$ kinetic energy$/\mu$ [43]. The magnetic moment of the electron will be scattered each time it passes through the non-adiabatic region. Consequently, no electron with this class of trajectory will be confined indefinitely because it will eventually be scattered into a loss cone.

The boundary that separates adiabatic and non-adiabatic segments of motion is described by the condition for adiabatic invariance of the magnetic moment [43]:

$$r_g|\frac{\nabla B}{B}| \ll 1 \tag{2.17}$$

This transition is not sharply defined, but occurs over a finite distance. However for the purposes of this analysis, we have chosen to approximate the transition region by the contour of $r_g = 0.1R$, where R is the device radius. This is the region marked in Figure 2.7.

The critical flux tube is defined as the set of magnetic field lines that have their minimum magnetic field point on the adiabatic boundary [57, 63], which is shown as the grey contour in Figure 2.8. A sample trajectory is shown for the case where the electron is started inside the

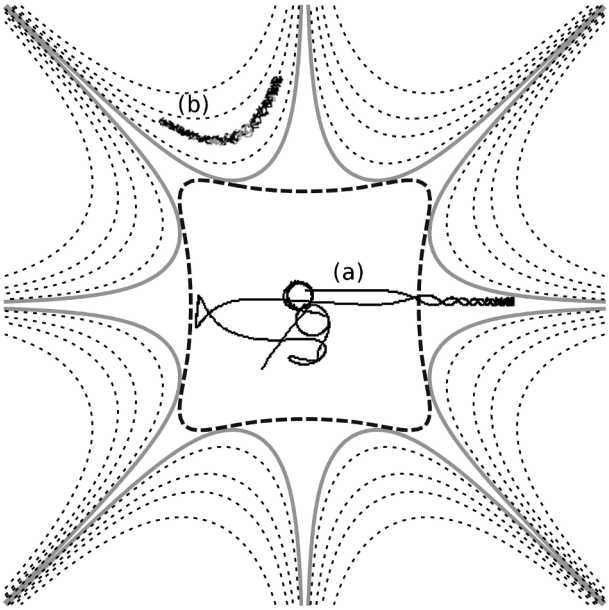


Figure 2.8: The critical flux tube seperating the two types of trajectories is shown as the thick solid line. The dashed line is the contour where the gyroradius is 10% of the device radius. Some other example field lines are shown as dotted lines. Trajectory (a) is inside the critical flux tube and consists of stretches of adiabatic motion seperated by random scattering in the central non-adiabatic region. Trajectory (b) is completely adiabatic and is indefinitely confined.

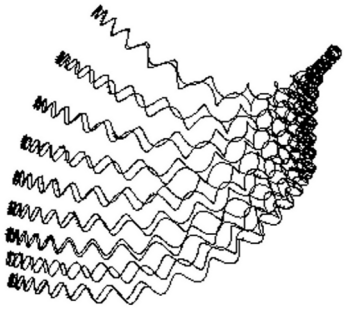

Figure 2.9: A 3D isometric view of the single trajectory shown in Figure 2.8 (b). The motion is completely adiabatic and will be confined indefinitely. Because the magnetic field is not completely uniform the electron drifts on a constant flux surface around the point cusp. When the motion is projected in to the $xy$ plane (as in Figure 2.8) the trajectory clearly bounces along a constant set of field lines.

critical flux tube. It has clearly defined segments of adiabatic and non-adiabatic motion. For electrons started outside this flux surface, the motion is completely adiabatic and the electron will be confined to a given field line. If the peak magnetic field along the field line is $B_{peak} > KE/\mu$, the electron will be confined indefinitely. Because the magnetic field is not uniform the electrons will drift on the same flux surface around the point cusp. This drift motion is shown in Figure 2.9.

## 2.4 Point and Line Cusps

Despite having favourable MHD stability properties, the major disadvantage of open-ended minimum B geometries is the rapid loss of plasma through their loss gaps. The biconic cusp geometry has two point cusps along the central axis and a wide ring cusp in the central plane of symmetry [56]. Some mirror devices utilise Joeffe bars to create a cusp that stabilises the interchange instabilities [42]. However the cusp in this type of device has wide linear loss gaps between the bars. It has been found that linear loss gaps, here referred to as line cusps, considerably reduce the effectiveness of plasma confinement and form the dominant loss mechanism from the device [61]. Various attempts to plug the line cusp have included electrostatic repeller plates, RF power, and simultaneous injection of plasma through the line cusp [44]. However none of these attempts have succeeded in adequately reducing the rate of loss from the line cusps.

The high-order spherical multipole was developed as a minimum B field configuration that eliminates the line cusps and consists only of point cusps [61]. Experimental studies compared a multipole field consisting of 30 point cusps with a conventional spindle cusp and found that the confinement time was 2.5 times longer in the multipole field [60, 62]. Although the experiment succeeded in eliminating the line cusps, the overall loss rate is proportional to the number of individual point cusps, and hence only led to a marginal improvement in overall confinement. The unique field geometry in the Polywell appears to solve both problems.

The point cusps in each face of the Polywell can be analysed with the conventional theory of cusp losses. However the structure of the loss region between the coils is far more complicated and was referred to by Bussard as the "funny cusp" [69]. By analysing the magnitude of the magnetic field at two crucial points we will show that this region can be treated as eight separate point cusps if the loop spacing, $S$, is less than a critical distance.

The simplest starting point is the case where the current loops are all in contact, $S = a$. The peak magnetic field in the face point cusp is given by taking the limit of Equation 2.15 as $y \,\&\, z \to 0$, and $S \,\&\, x \to a$.

$$\begin{aligned} \lim_{\substack{y,z\to 0 \\ S,x\to a}} B_x &= \frac{\mu_0 I\left((\sqrt{5}-25)\pi + 20\sqrt{5}(3E(\frac{4}{5}) - K(\frac{4}{5}))\right)}{50a\pi} \\ \therefore B_{face} &\approx \frac{0.286\mu_0 I}{a\pi} = \frac{0.572}{\pi}\frac{\mu_0 I}{2a} = \frac{0.572}{\pi}B_{loop} \end{aligned} \tag{2.18}$$

This equation is effectively the standard equation for the field due to a single current loop

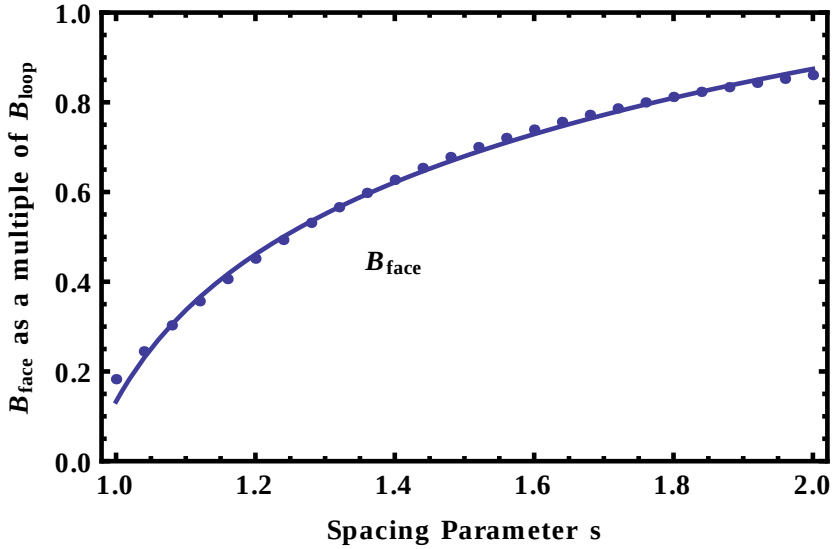


Figure 2.10: The magnetic field in the point face cusp ($B_{face}$) as a function of the coil spacing. Numerical data points are shown, compared to the fitted log function.

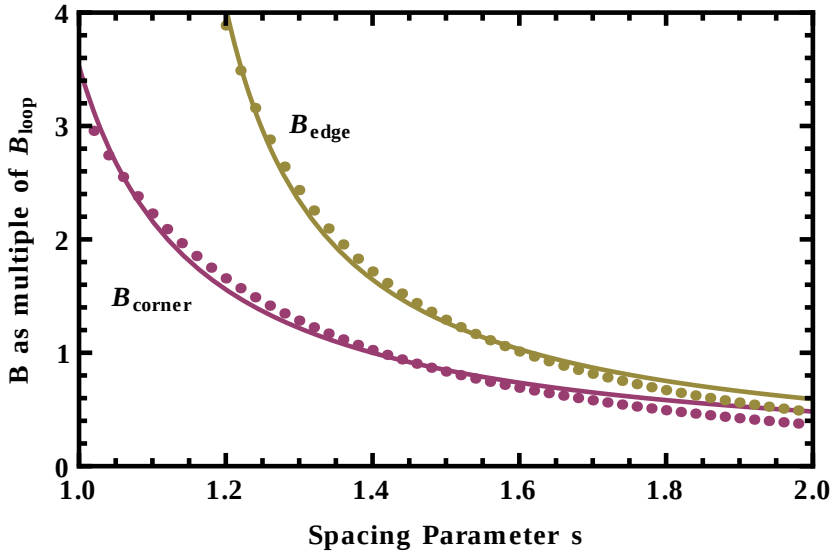


Figure 2.11: The magnetic field in the edge line cusp ($B_{edge}$) as a function of the coil spacing $s$. For small values of coil spacing the field behaves like the field due to infinitely long anti-parallel conductors. Numerical data points are shown against the approximate function.

[52], $B_{loop}$, except with an additional constant term that effectively describes the field reduction due to the superposition of the other adjacent current loops. Let us now express the loop spacing in terms of the loop radius, $a$, through a dimensionless parameter $s$, where $S = sa$. If the spacing parameter $s$ is now allowed to vary, we expect that $B_{face}$ must have the same form as equation 2.18 but multiplied by a function of $s$ that describes the changing superposition of the other loop components. We have found from numerical methods that it can be approximated by a log dependence on $s$.

$$B_{face}(s) = B_{loop}\frac{1.03}{\pi}\log[12.9(s-0.88)] \tag{2.19}$$

The approximate function for $B_{face}$ is plotted with the numerically calculated data points in Figure 2.10.

The field in the edge line cusp is dominated by the two closest loops. When these are almost in contact, we can approximate them as two infinitely straight wires. The expression for the field due to a straight wire is [52]

$$B_{straight}(d) = \frac{\mu_0 I}{2\pi d} \tag{2.20}$$

where d is the distance from the wires. In the geometry of the Polywell, it can be shown that

$$d = \frac{a(s-1)}{\sqrt{2}}. \tag{2.21}$$

We have found that Equation 2.20 approximates the numerically calculated data, providing allowance is made for an extra fitted geometrical factor, which takes into account the field reduction due to cancellation with the four more distant current loops. Once again, the resulting expression can be rearranged to be expressed in terms of the field due to a single current loop, $B_{loop}$. The expression predicted by the approximation is

$$B_{edge}(s) = B_{straight}(d) \times C = \frac{\mu_0 I}{2\pi}\frac{\sqrt{2}}{a(s-1)}C = B_{loop}\frac{\sqrt{2}}{\pi(s-1)}C, \tag{2.22}$$

where $C$ is a geometric constant, and thus the best numerically fitted expression was

$$B_{edge}(s) = B_{loop}\frac{\sqrt{2}}{\pi(s-1.06)}1.23. \tag{2.23}$$

By similar analysis the corner cusp is expressed as

$$B_{corner}(s) = B_{loop}\frac{\sqrt{2}}{\pi(s-0.84)}1.24. \tag{2.24}$$

Figure 2.12 shows the variation of $B_{face}$, $B_{corner}$ and $B_{edge}$ as a multiple of the single loop field, $B_{loop}$, and as a function of the spacing parameter $s$. The underlying trend of field variation with spacing is dominated by the behaviour of the nearest coil components. For example, the $B_{face}$ field is substantially reduced due to cancellation with the fields produced by the adjacent coils, and this effect is greatest at small spacings. In contrast, both $B_{corner}$ and $B_{edge}$ originate

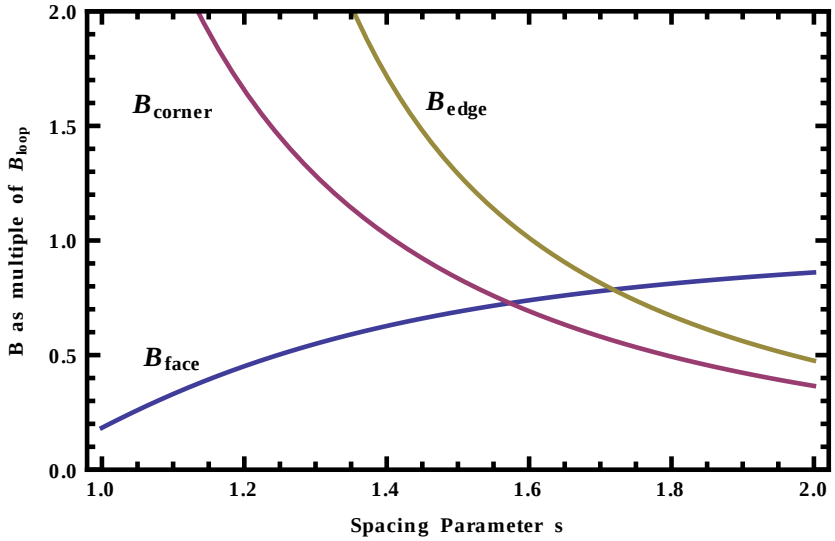


Figure 2.12: The peak magnetic field strength in the face, corner and edge cusps plotted together. The approximate equations for these different field regions described in the text are shown as solid lines, compared with numerically calculated data points. It is significant that at small loop spacings, the line cusp field is almost an order of magnitude larger than the point cusp components.

from the constructive addition of the adjacent coil components and result in an increase in field strength with reduced spacing.

At small loop spacings the magnetic field in the centre of the line cusp, $B_{edge}$, is almost an order of magnitude larger than the field in both types of point cusps. Consequently, in the region of small loop spacing the losses due to the point cusps will dominate, while ignoring the more complicated line cusp components. Instead the loss rate can be modelled with 14 point cusps - 6 due to the faces and 8 due to the corners. This point is reinforced in the heat map of magnetic field strength in Figure 2.13, revealing "the funny cusp" region can be modelled as a point cusp.

These ideas were supported by considering the spatial distribution of simulated electrons lost from the Polywell. The electrons were simulated using the Simion charged particle optics package [6, 15]. The starting position of 2,000 electrons were randomly distributed in a central spherical region inside the critical flux surface. All other parameters were chosen to match previous or planned experimental studies. All electrons had an initial energy of 100 eV and a single loop current of 20 kA (equivalent to 2 kA in our experimental Polywell). The current loop radius was set at $a = 0.025$ m. The electron trajectories were calculated until they left the cube region defined by the Polywell coils, i.e. a cube with side length equal to $S = sa$, centred on the origin. The confinement time of each electron was recorded as well as the spatial location of each electron when it escaped the Polywell's cubic confinement region.

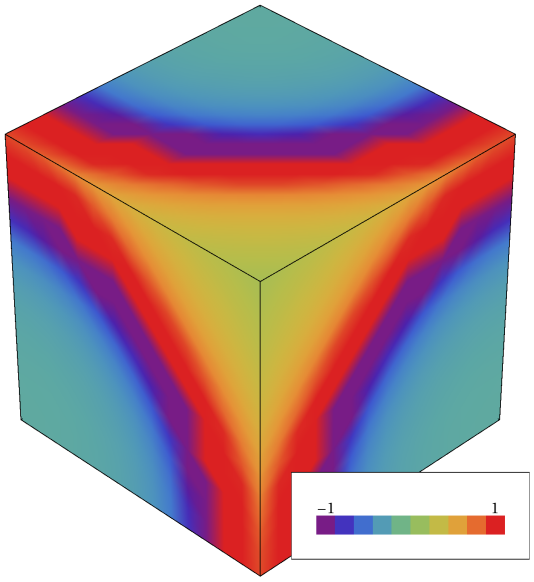


Figure 2.13: The relative magnitude and sign of the radial magnetic field $B_r\vec{\hat{\boldsymbol{r}}}$ on the cube surface containing the current loops. Only 1/8th of the surface is shown to reveal the smallest symmetrical element in detail. Blue and purple areas of the surface indicate where the field diverges radially and reveal the point cusp structure of the face cusps. The yellow and red areas show radial convergence of the field and hence reveal the "funny cusp" region described by Bussard. However, since the strongest field is present in the edge cusp near the current loops, this region can be neglected. Instead the funny cusp region can be modelled by only considering the corner cusp component as a point cusp.

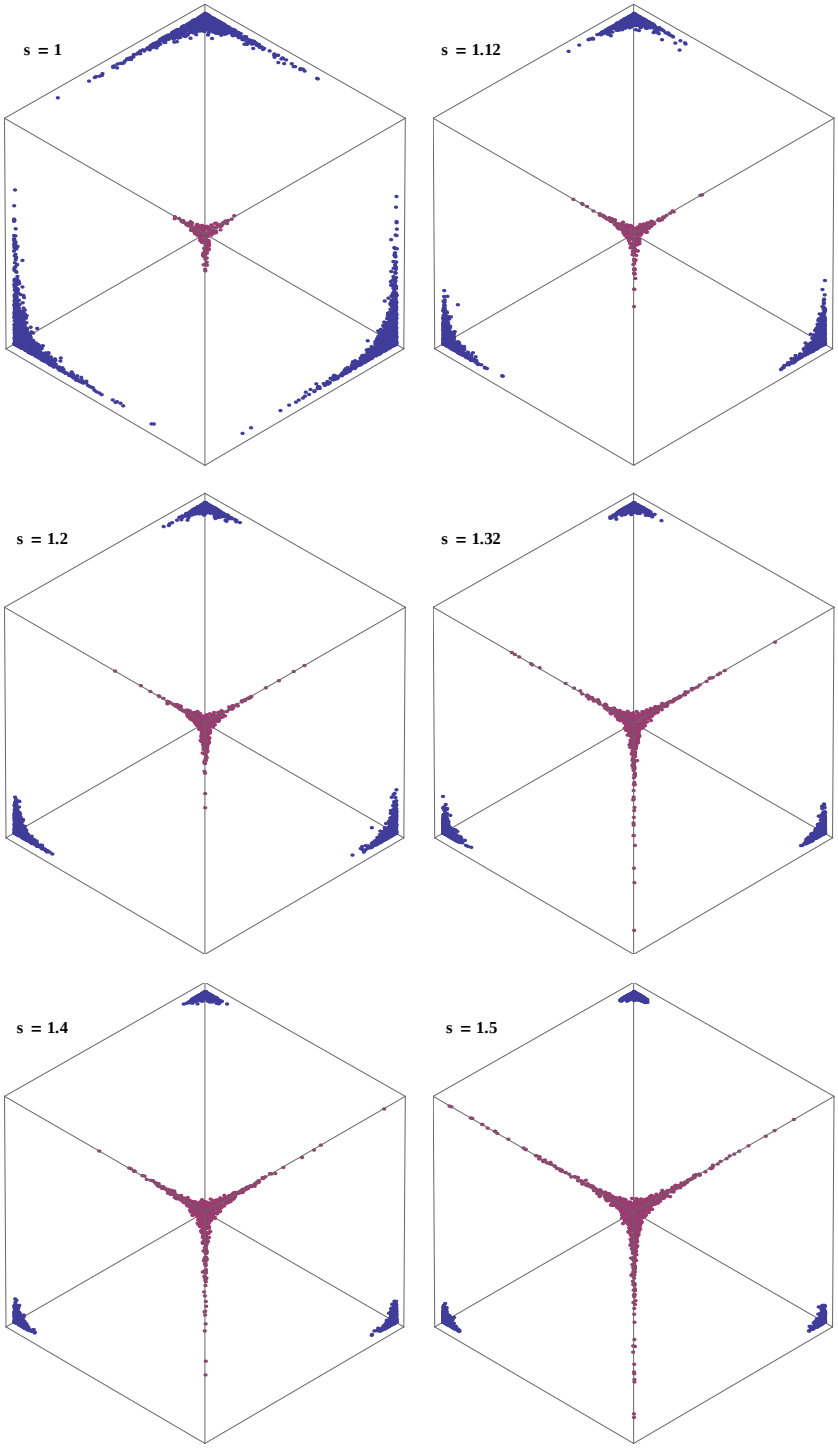


Figure 2.14: The electron loss locations as a function of coil spacing $s$. Only 1/8th of the surface is shown to reveal the smallest symmetrical element in detail.

The spacing was varied from $s = 1 \rightarrow 2$, and for each spacing the above simulation was repeated. The resulting spatial distribution of electrons when lost from the Polywell is plotted as a function of coil spacing $s$ in Figure 2.14. Only 1/8th of the surface is shown to reveal the smallest symmetrical element in detail. The electrons are coloured differently depending on whether they escaped through the face or corner cusp. Overall, the electron losses are quite well confined to narrow regions on the face and corner cusps over all coil spacings. In particular, the electrons are constrained quite tightly to the face and corner cusps for spacings in the range $s = 1.1 \rightarrow 1.3$. Electron loss through the edge line cusp is not significantly observed for any of the coil spacings plotted in Figure 2.14, which supports the hypothesis that electron loss in the Polywell can be analysed with point cusp theories.

The fraction of the electron population inside the loss cone of a single point cusp is well established [43, 46] and was discussed in Chapter 1. The fraction of particles lost in a biconic cusp is

$$L_{biconic} = 1 - \sqrt{1 - \frac{B_0}{B_m}}. \tag{2.25}$$

Bussard argued that this expression can be modified by a factor of $n$ for a system of $n$ point cusps that do not have overlapping loss cones [64]. Thus, equation 2.25 would become

$$L = \frac{n}{2}\left(1 - \sqrt{1 - \frac{B_0}{B_m}}\right). \tag{2.26}$$

In the case of a Polywell with small spacing there are $n = 14$ point cusps (6 due to the faces and 8 from the corners). The magnetic field, $B_0$, is the minimum field from which the magnetic moment is conserved and occurs at the radius $r_0$. The peak magnetic field in the device is $B_m$ and is different for the two different types of point cusps since each has a different maximum magnetic field as a function of coil spacing. Hence we can define the loss fraction for each type of point cusp separately, based on its peak magnetic field defined in equations 2.19 and 2.24.

$$L_{face} = \frac{6}{2}\left(1 - \sqrt{1 - \frac{B_0}{B_{face}}}\right) \tag{2.27a}$$

$$L_{corner} = \frac{8}{2}\left(1 - \sqrt{1 - \frac{B_0}{B_{corner}}}\right) \tag{2.27b}$$

If we assume that each type of point cusp has the same minimum value for the adiabatic field $B_0$ (under these simulation conditions $B_0 \approx 15$ mT), and also assume that each electron has an equal chance of finding any of the point cusps, then we can calculate the total fraction of electrons lost through each type of point cusp by taking the ratio of its loss probability and the total loss probability. For this calculation we will also assume that the probability of electrons being lost through an edge line cusp is negligible ($L_{edge} \approx 0$) for small coil spacings. Thus the fraction of electrons lost through the face and corner cusps would be

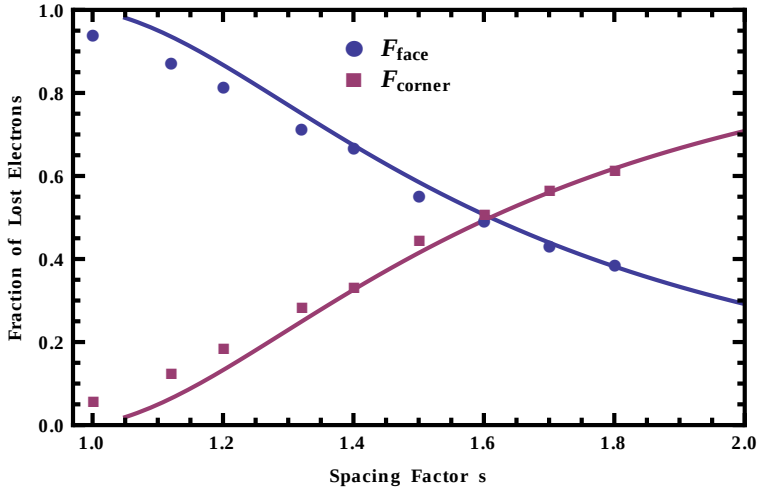


Figure 2.15: The fraction of lost electrons through both the face and corner point cusps as a function of coil spacing $s$. There is good agreement between the theoretical values of equations 2.28a and 2.28b, and the simulated data from Figure 2.14.

$$F_{face} = \frac{L_{face}}{L_{face} + L_{corner}}, \tag{2.28a}$$

$$F_{corner} = \frac{L_{corner}}{L_{face} + L_{corner}}. \tag{2.28b}$$

These loss fractions have been calculated as a function of coil spacing $s$ and plotted in Figure 2.15 with the simulated data from Figure 2.14. There is good agreement between the simulated dataset and the model, even though the model approximates the 3D field structure with a 1D model. The small amount of deviation in Figure 2.15 from the theory suggests $F_{edge} < 10\%$, making it negligible but not zero, $F_{edge} \neq 0$. This result lends further support to the idea of modelling the Polywell with point cusp theories.

The fact that the line cusp component can be neglected indicates that the Polywell magnetic field geometry might result in a greater confinement time than the conventional biconic cusp. In the biconic cusp, the situation is reversed and the line cusp losses dominate [61, 62]. Figure 2.16 shows contour plots for the magnetic field in the $xy$ plane of both devices. The biconic cusp has a wide linear loss region in the central plane of rotation. Here the field is substantially lower than the point cusp, and when revolved in 3D, the loss area is very large. By comparison, because the line cusps can be ignored in the Polywell, the point cusp losses dominate and we expect the loss rate is substantially lower. Consequently confinement times should be longer in the Polywell field geometry.

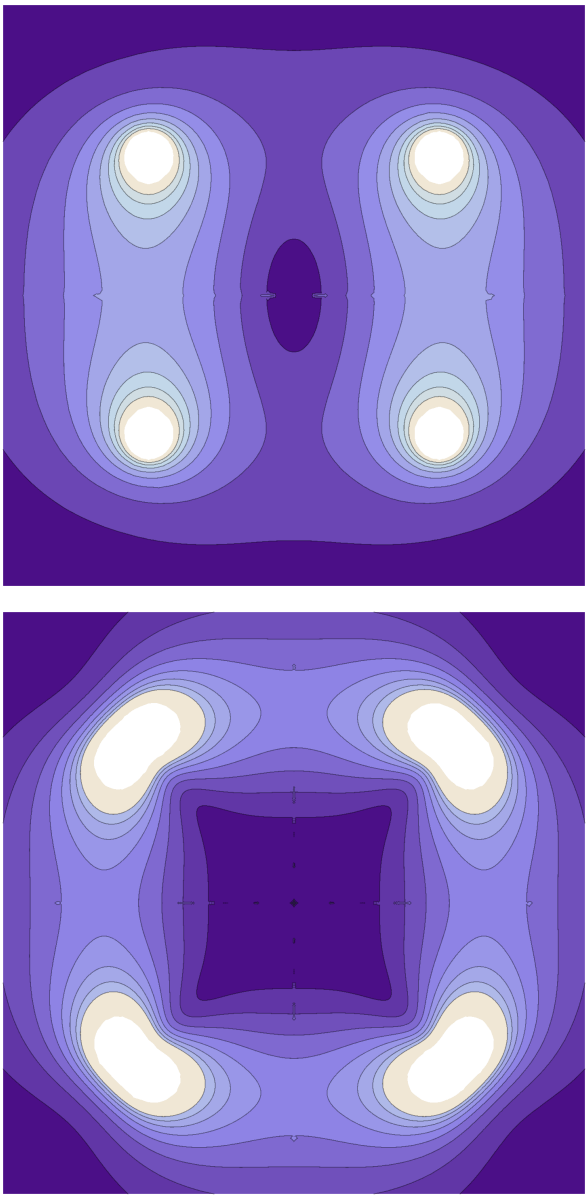

Figure 2.16: A comparison of a biconic cusp (top) and the Polywell (bottom) magnetic fields. Both plots show contours of magnetic field strength in the $xy$ plane. Eight contours are plotted ranging from 0.025 T to 0.2 T in steps of 0.025 T. The darkest contour shading represents the region of lowest magnetic field, through to white for the highest field region. The current in the biconic cusp has been adjusted so that the peak field in the face point cusp of both devices is equal, allowing comparison of the two confining magnetic field structures. In the biconic cusp, the field in the circular line cusp is clearly much weaker than in the point cusp. The line cusp losses dominate both because the field is weaker in this region, and also because the loss area is much larger when revolved around the symmetry axis. In the Polywell, this situation is reversed and the point cusps exhibit the weakest magnetic field.

## 2.5 Central Magnetic Field Approximation

In order to assess the future of the Polywell concept as a fusion energy device and further improve our understanding of its limitations we seek a model system that sufficiently captures the essential physics of the Polywell, while simultaneously being simple enough to make theoretical calculations tractable. For example, in order to carry out an analysis of the electron confinement time in the central region of the Polywell, we need to obtain an unsophisticated analytical expression in closed form for the magnetic field in this region.

For situations of high cylindrical symmetry, the axial magnetic field components of a single loop, $B_\rho$ and $B_z$, can be approximated near the axis of symmetry in terms of the field along the $z$ axis only [54],

$$\begin{aligned} B_\rho(\rho, z) &= -\frac{\rho}{2}B_z'(z) + \frac{\rho^3}{16}B_z'''(z) - \dots \\ &= \sum_{n=1}^{\infty} \frac{(-1)^n B_z^{2n-1}}{n!(n-1)!}\left(\frac{\rho}{2}\right)^{2n-1} \end{aligned} \tag{2.29a}$$

$$\begin{aligned} B_z(\rho, z) &= B_z(z) - \frac{\rho^2}{4}B_z''(z) + \dots \\ &= \sum_{n=0}^{\infty} \frac{(-1)^n B_z^{2n}}{(n!)^2}\left(\frac{\rho}{2}\right)^{2n} \end{aligned} \tag{2.29b}$$

Hence, the contributions due to the two loops centred on a single Cartesian axis can be described by their superposition along that axis only. The magnetic field along the axis of a single coil is [52, 53]

$$\lim_{\rho\to 0} B_z(\rho, z) = B_z(z) = \frac{\mu_0 I a^2}{2(a^2+z^2)^{3/2}} \tag{2.30}$$

and thus the contributions to the field by these two coils are the sum of two $B_z(z)$ axial equations centred on offsets of $\pm S$. In the interests of simplicity let us limit the analysis to the case where adjacent coils are in contact, $S = a$ (or equivalent to $s = 1$), and expand these axial terms in a Taylor series about the point $z = 0$. To avoid a non-trivial solution we need to take terms to third order. This results in

$$B_z(z) \approx \frac{\mu_0 I z(24a^2 + 5z^2)}{32\sqrt{2}a^4}. \tag{2.31}$$

This series approximation converges very well in the region $\pm a/2$, thus the simplified model system will only accurately reflect the field structure in the core of the Polywell. Substituting Equation 2.31 into Equations 2.29a and 2.29b, and using the results in Equations 2.15 and 2.16

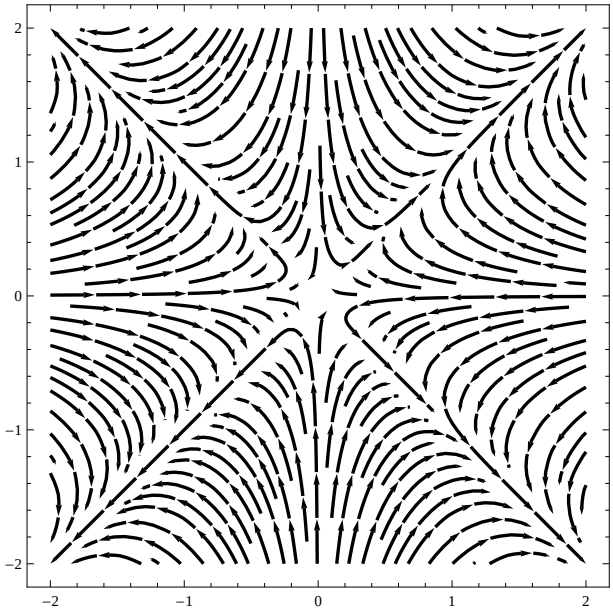


Figure 2.17: The fieldlines generated by Equation 2.32. This field closely approximates the interior magnetic field of the Polywell.

yields

$$\begin{aligned}\vec{\boldsymbol{B}} &= \frac{35\mu_0 I}{128\sqrt{2}a^4}\Big((-2x^3+3x(y^2+z^2))\vec{\boldsymbol{x}} \\ &\quad +(-2y^3+3y(x^2+z^2))\vec{\boldsymbol{y}}+(-2z^3+3z(x^2+y^2))\vec{\boldsymbol{z}}\Big)\end{aligned} \tag{2.32}$$

The resultant field lines in the $xy$ plane are shown in Figure 2.17. Bussard's original field approximation, $B \propto r^3$, can be recovered by setting $y = z = 0$ in Equation 2.32, which gives the field along the $\vec{\boldsymbol{x}}$ axis, $B_x \propto x^3$.

Future analysis of plasma dynamics within the Polywell may require closed form expressions of the magnetic vector potential $\vec{\boldsymbol{A}}$. This can be obtained by using the same methods shown here for the magnetic field, $\vec{\boldsymbol{B}}$, by using the same on-axis approximation for two loops with opposing currents. Zworykin [54] presents an approximation for $\vec{\boldsymbol{A}}$ derived from Stoke's theorem and Maxwell's equations. In the special case of two loops centred on the same axis with high cylindrical symmetry, $\vec{\boldsymbol{A}}$ only has components in the direction of $\vec{\hat{\boldsymbol{\theta}}}$.

$$\begin{aligned}A_\theta(\rho,z) &= \frac{\rho}{2}B_z(z)-\frac{\rho^3}{16}B_z''(z)+\ldots \\ &= \sum_{n=0}^{\infty}\frac{(-1)^n B_z^{2n}}{n!(n+1)!}\left(\frac{\rho}{2}\right)^{2n+1}\end{aligned} \tag{2.33}$$

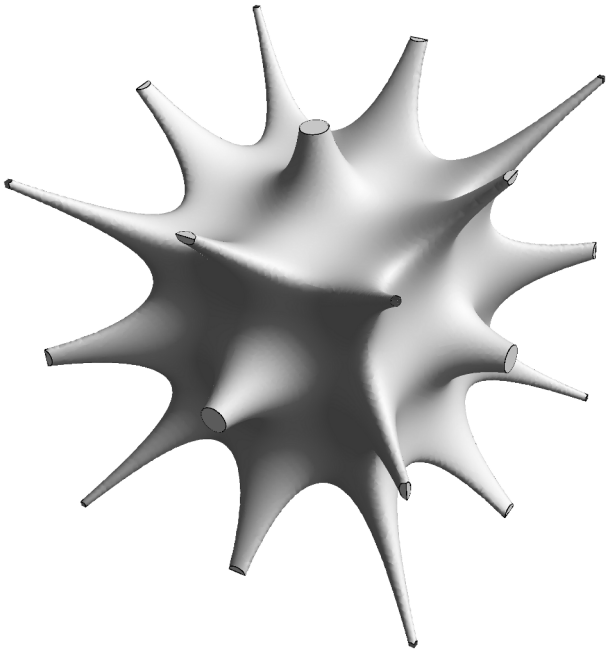

Figure 2.18: The flux surface generated from plotting $\vec{\boldsymbol{A}} = constant$. A slice through the centre plan of this surface reproduces the critical flux lines shown in Figure 2.8. In the limit where the coils are touching, only point cusps are present. As the spacing is increased, the edge cusps span out to the corner cusps and form wide linear loss regions.

Using Equation (2.31) in the approximation for $\vec{\boldsymbol{A}}$ gives:

$$A_\theta(\rho, z) = -\frac{\mu_0 I \rho z (96a^2 + 20z^2 - 15\rho^2)}{256\sqrt{2}a^4}. \tag{2.34}$$

Summing the contributions from each axis and using similar geometric arguments gives the expression for the total $\vec{\boldsymbol{A}}$.

$$\vec{\boldsymbol{A}}_{\boldsymbol{x}} = A_\theta(\rho_{xy}, z)\frac{y}{\sqrt{x^2+y^2}} - A_\theta(\rho_{xz}, y)\frac{z}{\sqrt{x^2+z^2}}. \tag{2.35}$$

Using the two loop approximation (Equation 2.31) we find the $\vec{\hat{\boldsymbol{x}}}$ axis term,

$$\vec{\boldsymbol{A}}_{\boldsymbol{x}} = \frac{35\mu_0 I y z (y^2 - z^2)}{256\sqrt{2}a^4}. \tag{2.36}$$

The other components of $\vec{\boldsymbol{A}}$ can be generated by cyclically permuting the Cartesian coordinates in Equation 2.36. In Figure 2.18 a sample flux surface is shown by plotting the region $\vec{\boldsymbol{A}} = constant$. The adiabatic trajectory shown in Figure 2.9 is constrained to a flux surface like the example shown in this figure.

## 2.6 Approximate loss rate and confinement time

The simplified expressions for $\vec{\boldsymbol{B}}$ in Equation 2.32 can be used to create and test an approximate model of electron confinement in the Polywell. These equations apply to the limit of small spacing where the loops are in contact, and the contributions of the line cusps can be ignored. The fraction of the electron population inside the Polywell's loss cones are described by equation 2.26 [64, 43, 46]. In this case there are $n = 12$ point cusps (6 due to the faces and 8 from the corners). $B_0$ is the minimum field from which the magnetic moment is conserved and $B_m$ is taken to be the peak field in the device. For the central well approximation we will assume that the electron losses through the face and corner fields are balanced and hence $L_{face} = L_{corner} = L$ for $n = 12$.

For the population of electrons inside the critical flux surface, the loss fraction can be interpreted as the probability of escape after each successive random scattering event inside the central non-adiabatic region. Therefore, by ignoring the influx of electrons from external sources, the loss rate of electrons escaping from the magnetic well can be expressed as

$$\frac{dN(t)}{dt} = -\frac{LN}{\tau_{trans}} \tag{2.37}$$

$$\therefore N(t) = N_0 e^{\frac{-Lt}{\tau_{trans}}} \tag{2.38}$$

where $N(t)$ is the number of electrons remaining after a time $t$ of being introduced into the central region.

The average transit time $\tau_{trans}$ can be approximated by considering both the adiabatic and non-adiabatic components of the electron trajectories. The non-adiabatic components consist of approximately straight trajectories that are randomly scattered about the well until they enter a point cusp. As an order of magnitude estimate, we have assumed without further analysis an average of 10 scattering events before entering a loss cone. This assumption is only based on observing the statistics of the numerically calculated trajectories.

The transit time along a point cusp in the adiabatic mirror region can be found by considering the change in parallel velocity as the electrons move into stronger field regions [46]. The velocity component parallel to the magnetic field, $v_{\|}$, can be expressed in terms of the initial velocity $v_0$ and the mirror ratio $B(z)/B_0$ as

$$v_{\|} = v_0 \sqrt{1 - \frac{B(z)}{B_0} \sin^2 \theta_0}, \tag{2.39}$$

where $\theta_0$ is the angle between the velocity vector and the magnetic field at $B_0$. Since $v_{\|} = \frac{dz}{dt}$, it can be shown that

$$t = \frac{1}{v_0} \int \frac{1}{\sqrt{1 - \frac{B(z)}{B_0} \sin^2 \theta_0}} dz \tag{2.40}$$

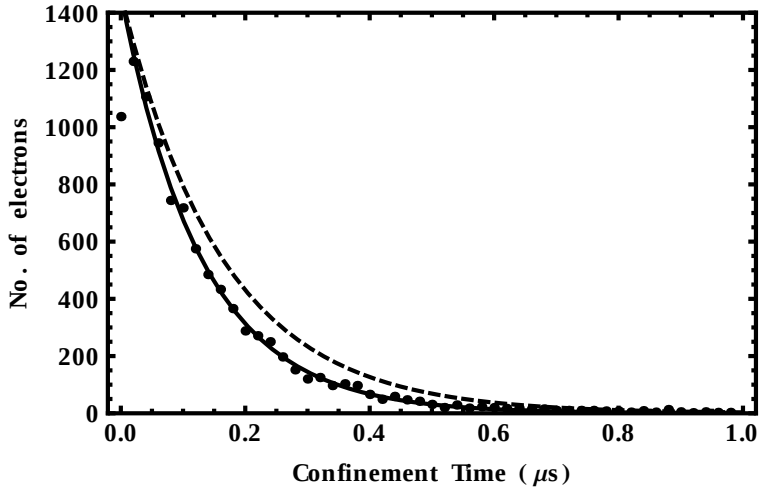


Figure 2.19: The distribution of confinement times for 10,000 electron trajectories simulated in the Simion charged particle optics software. The data points have been fitted for the mean confinement time. The theoretical result is shown as the dashed curve.

Therefore, the total transit time in the Polywell between adiabatic reflections is the sum of the transit times on either side of the critical flux tube.

$$\tau_{trans} = \frac{2}{v_0}\int \frac{1}{\sqrt{1-\frac{B(z)}{B_0}\sin^2\theta_0}}dz + 2\frac{10r_0}{v_0} \tag{2.41}$$

This model was tested in the Simion charged particle optics package[6, 15]. The starting position of 10,000 electrons were randomly distributed in a central spherical region inside the critical flux surface. Hence only electrons with two-component trajectories were studied. All electrons had an initial energy of 100 eV, and the current in the loops was 10 kA. The current loop radius was set at 0.025 m, with a spacing $s = 1$. The electron trajectories were calculated until they left the cube region defined by the Polywell coils, i.e. a cube with side length 0.05 m centred on the origin. The confinement time of each electron was recorded and the resulting distribution is shown in Figure 2.19.

The simulation was compared with the model predictions in Equation 2.41 and the magnetic fields were calculated directly with the simplified central well Equation 2.32. Hence the model was tested against the simplest magnetic field case. The minimum magnetic field at which the magnetic moment is conserved, $B_0$, was calculated from the critical flux tube where $r_g = 10\%R$. The angle with the deepest penetration into the cusp field was used for $\theta_0$. All other parameters were as given above in the simulation.

The fit to the simulated data (dashed line) and the theoretical calculation (solid line) is found to be in good agreement. The fact that the simulated data follows an exponential, confirms that a statistical scattering model is relevant inside the critical flux tube. The simulated data was found to have a mean confinement time of $\tau_0 = 0.129$ $\mu$s, compared with a theoretically calculated value of $\tau_0 = 0.163$ $\mu$s.

The fit to the simulated data (solid line) and the theoretical calculation (dashed line) is found to be in good agreement. The exponential decay of the simulated data confirms that a statistical scattering model is relevant inside the critical flux tube. The simulated data was found to have a mean confinement time of $\tau_0 = 0.129$ $\mu$s, compared with a theoretically calculated value of $\tau_0 = 0.163$ $\mu$s. It is worth pointing out that no effort has been made to adjust the input parameters to optimise the confinement time. The input values used only represent a single case used to test the applicability of conventional point cusp theory.

## 2.7 Electrostatic Plugging of Point Cusps

The prospect of the Polywell as a fusion energy device has to be examined within the context of a sub-microsecond confinement time. For example, a litre of 100 eV electrons at a density of $10^{19}$ m$^{-3}$ would require $\approx$ 400 kW of input power to sustain the energy lost by the electrons with $\tau_0 \approx 0.15$ $\mu$s. However the model developed in this paper is only intended to accurately describe the low beta case (such as during start-up) and at higher densities other plasma effects are anticipated to increase the confinement time.

Space charge limited flow could occur along the critical flux tube, effectively plugging the point cusps. Each point cusp can be treated as an isolated flux tube and modelled like a vacuum diode with the Child-Langmuir law. The electron current leaking from the Polywell along a point cusp in Figure 2.18 is similar to the electron current emitted by the cathode in a vacuum diode. The Child-Langmuir law for space charge limited current is

$$j = \frac{4}{9}\epsilon_0 \sqrt{\frac{2e}{m_e}} \frac{V^{3/2}}{h^2} \tag{2.42}$$

where $V$ is the voltage applied to plane electrodes separated by a distance $h$ [45]. In the case of a virtual cathode forming in the middle of the Polywell, the anode to virtual cathode voltage may be $\approx$ 100 V for 100 eV electrons. Taking a worst case scenario approach, the point cusp leakage area can be estimated as roughly the geometric size of the critical flux tube, giving a radius on the order of 0.5 cm. After taking into account the total leakage area for all 14 point cusps and assuming $h \approx 0.5$ cm, we find $I \approx 0.1$ A or equivalently 10 W of power lost. Obviously this calculation is far too simplistic to be accurate because space charge effects have been neglected, but it does demonstrate the concept of electrostatically plugging the point cusps. These effects could be included in future studies by consulting Dolan's review article on electrostatic cusp plugging [77].

## 2.8 Summary

- The magnetic field structure of the Polywell has been analysed in its complete form, as well as areas of interest such as the point and line cusps, and the central well approximation. It has been found that at small spacings it is possible for point cusp losses to dominate over line cusp losses, allowing the application of conventional point cusp theory to the Polywell. The dominance of point cusp losses may prove beneficial in terms of providing a lower overall loss rate when compared with other devices such as the biconic cusp.

- The types of trajectories that can occur have been analysed in terms of their adiabaticity. It was found that the two component trajectories described in models of biconic cusp confinement can be adapted to the Polywell. The resulting model describes a critical flux surface separating the two types of trajectories, and also defines the minimum field, $B_0$, needed for a simple scattering model of confinement.

- The simplified scattering model was found to be in reasonable agreement with a simulation with parameters matching our current experimental parameters. The central well approximation was used to calculate magnetic fields for the model and simulations, but the correlation between these and experimental results will be left for future work.

- Future studies should address the question to what degree confinement in the Polywell is determined by the parameters of the central well field, and whether the central well approximation can be used to study other aspects of Polywell plasma physics.

- Furthermore, the model of point cusp loss needs to be extended for the high beta case where the Wiffle ball confinement mode and electrostatic plugging effects are anticipated to have a favourable effect on the overall electron confinement time. Neither of these effects have been included in the analysis of this chapter.

Chapter 3

# Experimental Setup and Techniques

Most of the different pieces of equipment and experimental apparatus used in this work were custom designed and constructed in order to study the basic elements of Polywell physics. This chapter contains details of their construction and function, as well as their integration into the complete experimental set-up.

The overriding aim of all Polywell and IEC research is to produce a deep and sustained potential well for supporting fusion grade plasmas. Moreover, for the purpose of producing fusion, the dependence of the well depth on gas/ion density, electron injection energy and current, etc, must be determined. To this end, all of our experiments are designed primarily to measure and determine if potential well formation has occurred. A secondary goal is to measure how the potential well is affected by other parameters of the plasma and experimental control parameters such as electron injection current and energy.

The experimental part of this thesis can be divided into experiments based on two different types of Polywell designs. The first series of experiments were carried out on a Teflon Polywell to study the magnetic field effects of the Polywell on a collimated electron beam using a single ended Langmuir probe for measuring floating potentials. The second set of experiments involved a more detailed Langmuir probe study on a metal Polywell, which was closer in design to Bussard's WB6 design. However, this second Polywell was much smaller in size than that of WB6, and, consequently, will be referred to as WB6-mini in this document.

## 3.1 Teflon Polywell Experiments

### 3.1.1 Design Rationale and Construction

The Teflon Polywell was used first because it was a readily achievable construction and enabled the experimental exploration of some Polywell physics. Only one other group has thus far published papers on Polywell experiments and their latest designs represent the culmination of nearly 20 years of work [69]. The most fundamental elements of a Polywell are the magnetic field coils and a monoenergetic electron source. The Teflon Polywell design enabled both of these elements to be investigated using a simple design.

There is an inverse relationship between coil size and the required magnetic field strength. Specifically,the larger the coil radius the lower the $B$ field required to confine a given electron. However, the required coil current increases with coil radius to create the same magnetic field. In designing a Polywell there is an optimisation procedure that must be observed between the number of turns in a coil and the required current through it, given the maximum voltage of

the power supply from which the current through the coils is obtained. That is, an increasing number of turns also results in an increasing electrical resistance in the coils, and thus one must limit the number of turns such that sufficient current can be obtained in the coils to produce the required magnetic fields.

For example, in the high field ranges of 0.1 T currents of 1 kA are typically needed, and for such large currents even small lengths of small diameter wire can increase the resistance to measurably reduce the achievable current. Additionally, the spatial constraints introduce further compromises since the copper wire diameter can be increased in order to decrease the wire resistance and hence increase the achievable current, however this reduces the number of turns in the coil and reduces the overall Amp turns in a given coil. Furthermore there is a simple practical limit on how many turns can fit into a coil without destroying the intended magnetic field geometry. For example, a ⌀5 cm coil can not fit 100 turns of ?guage copper wire. However Bussard's WB6 was ⌀80 cm and could easily support many hundreds of turns.

Our design settled on a rather compact size of ⌀6 cm, mainly due to the anticipated size constraints of the vacuum chamber and the highest achievable coil current with the electrical equipment available. The pulsed power supply intended for use with our Polywell was projected to produce up to 2.5 kA and with 10 turns would produce peak fields of up to 0.38 T in the coil faces.

Bussard's WB6 design included an electrical bias on the the metallic coil formers. This bias produced an electric field that was used for aiding electron injection and for reducing the size of the point cusp loss cone. For simplicity, only the vacuum magnetic field effects were studied initially without the added effects of superimposed magnetic and electric fields. Consequently, a dielectric was used as a former to insulate the coils from the plasma and protect against arcing.

Teflon was chosen as the coil former dielectric and each coil former was made from a Teflon reel turned in a lathe. The inner faces of opposing reels were separated by 6 cm, and joined with small Aluminium brackets mounted near the cube edges, as shown in Figure 3.1. Each coil former had 10 turns of ? gauge enamelled copper wire wound on and joined with barrel connectors to form one continuous current loop.

The spacing factor of the Teflon Polywell is $s = 1.4$. Although this is much larger than the ideal spacing factor of $s \simeq 1.2$, $s = 1.4$ was deemed to be the smallest $s$ attainable without adding greater complexity to the design. The physical constraints of a small device did not enable an s close to 1.2 to be obtained. With an $s = 1.4$ the mirror reflection effect in the coil faces will be much greater than in the edge and corner cusps, as discussed in Chapter 2. Hence the electrons will tend to leak out of the corner point cusps more than the coil faces. This was deemed acceptable as the first experiment was more concerned with testing the basic ideas of electron confinement in the Polywell magnetic field, rather than the comparatively more advanced goal of trying to optimise electron confinement in the device.

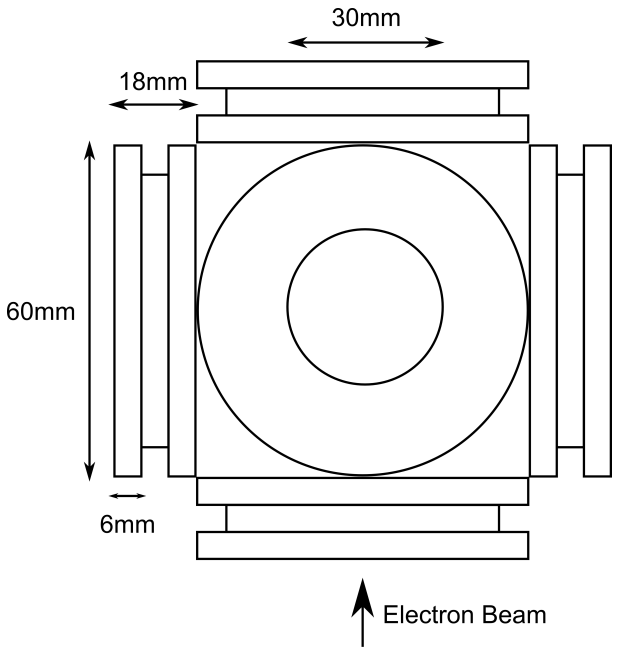


Figure 3.1: Schematic of our Polywell design, constructed from six identical circular Teflon pieces. They have a major diameter of 6 cm, and a hole machined out of the centre with diameter 3 cm. A groove 6 mm wide and 6 mm deep is cut around the outer edge to accommodate the copper wire. The six Teflon pieces were held in place by aluminium angle brackets where two Teflon pieces meet at an cube edge.

Figure 3.2: Two photos of the Teflon Polywell before adding coil windings. The left is orientated down the corner cusp revealing the aluminium angle bracket. The right image reveals the front view of the coil face.

### 3.1.2 High Current Pulsed Power Supply

A custom power supply was built to deliver the high currents needed for the Polywell magnetic field coils using components from the decommissioned capacitor bank of the Tortus tokamak [5]. The power supply consisted of a 7.5 mF capacitor bank, which could be charged to a maximum voltage of 450 V. The capacitors were discharged through a triggered Silicon Controlled Rectifier (SCR) in series with the field coils.

The resistive elements of a bar heater were used as a power dump to ensure the capacitors were totally discharged when the power was turned off. Two relays were used to alternatively isolate the 450 V charging power supply and the SCR trigger circuit. This was to ensure that the power supply could not be directly connected across the Polywell coils which would latch the SCR open and possibly destroy the coils through overheating. The 450 V charging supply used a step up transformer with 6 parallel taps to provide 6 parallel rectification circuits for fast capacitor charging. A flyback diode was connected across the capacitor bank to prevent the capacitors from becoming reverse biased during the back emf of field collapse. The basic elements of the circuit are shown in Figure 3.4, a more detailed circuit schematic is provided in Appendix B.1. A plan view photo of the capacitor bank is shown in Figure 3.5 with some key circuit elements highlighted.

When tested with the Teflon Polywell as a load the maximum peak current achieved was 2.5 kA with a pulse shape as shown in Figure 3.3. The peak current was varied between 200 A and 2.5 kA by changing the charging voltage applied to the capacitors. The peak current was approximately constant over 0.5 ms.

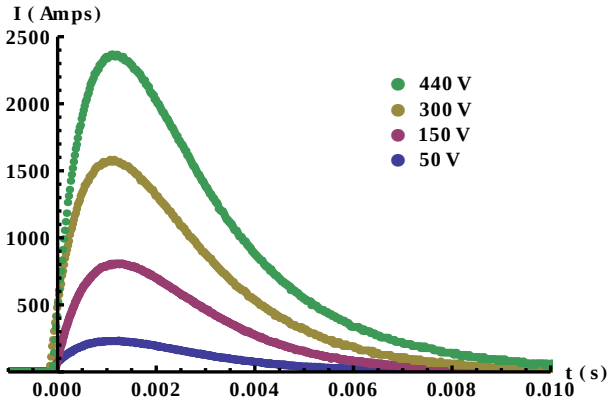


Figure 3.3: Some sample current profiles through the Polywell coils. These current pulses are attained by varying the voltage on the capacitor bank between 50 V and 450 V, giving a maximum current of nearly 2.5 kA. In this experiment the Teflon Polywell mounted in the vacuum chamber was used as the test load. The peak current was approximately constant over 0.5 ms.

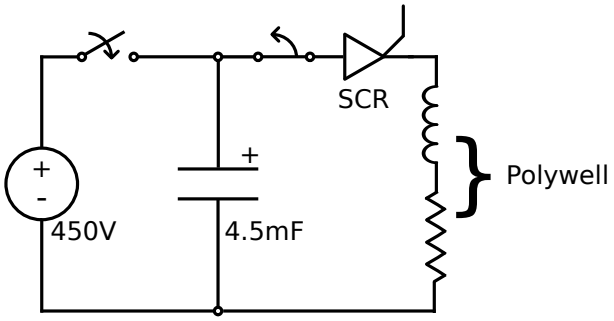


Figure 3.4: The basic elements of the high current pulsed power supply circuit.

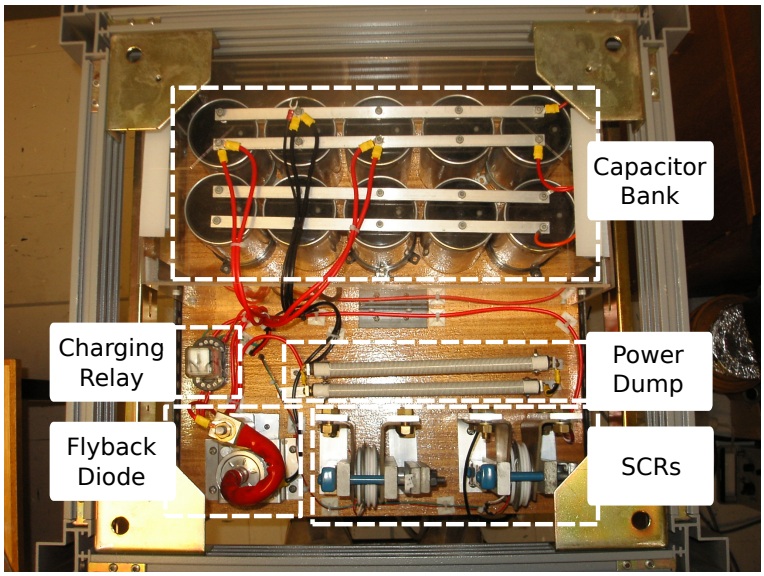


Figure 3.5: A plan view photo of the top rack of the HV pulsed power supply during construction. Some key elements are highlighted.

### 3.1.3 Cylindrical Cathode Electron Source

Electrons were supplied in a single, collimated monoenergetic beam from a cylindrical hollow cathode. A number of previous studies from our lab at the University of Sydney have shown that a cylindrical hollow cathode operating in a hollow cathode discharge mode can effectively isolate the micro-channels observed in a starmode gridded IEC system [22, 26, 27, 38–40]. Magnetic deflection experiments of the electrons emerging from the cylindrical cathode have shown that the beam produced is monoenergetic with energies 80% to 100% of the applied cathode potential [22]. The principle advantage of this method over other possible electron guns is its simplicity. The generation, acceleration and focusing of the electron beam all happens conveniently in one step whereas in a conventional electron gun setup, each of these processes require a separate focussing/extraction grid. This process often involves modelling of electron beam dynamics and the need for custom machined components for the electrostatic lens and acceleration grid components. Therefore it was anticipated that the newly characterised cylindrical cathode discharge would offer substantial benefits for researching electron confinement physics in the Polywell magnetic fields.

Bussard's most successful Polywell (WB6) used the more conventional hot filament method to generate electrons through thermionic emission. The WB6 Polywell was floated to a high positive voltage to accelerate the electrons, and attract them to the general Polywell region, but was not capable of focussing them into a beam. Because the Polywell circuit was raised to a high potential above ground its coil power supply needed to float as well, creating a great deal of complexity in the custom built power supply design. This ultimately contributed to the uncontrollable arcing issues that destroyed the WB6 device [69].

By using a cylindrical hollow cathode the electron beam generation process was greatly simplified and simultaneously negates the need to float the Polywell for electron acceleration, thus reducing the required complexity for the coil power supply. Although there are other anticipated benefits to the confinement properties of a Polywell at high positive potential, this design feature is left for another experiment because of the additional technical complexity required. Furthermore, it simplifies the physics being studied since we can neglect the vacuum electric field effects on electron motion.

The cylindrical cathode electron beam was powered by a high voltage power supply delivering up to 20 kV, in currents ranging from 1-20 mA. The major disadvantage of the cylindrical cathode electron beam is that the beam energy and current are essentially determined by the V-I breakdown characteristics of the cathode. The lowest beam energy possible was fixed at 6 keV, determined by the lower limit of plasma breakdown in our operating pressure range. The breakdown characteristics of our discharge limited our operating range to 15 mTorr to 35 mTorr of Hydrogen. In future experiments by other research students this limit will be overcome by moving the hollow cathode to an adjacent injection chamber allowing a substantial pressure differential to be maintained, and subsequently allowing much lower operating pressures to be achieved [18].

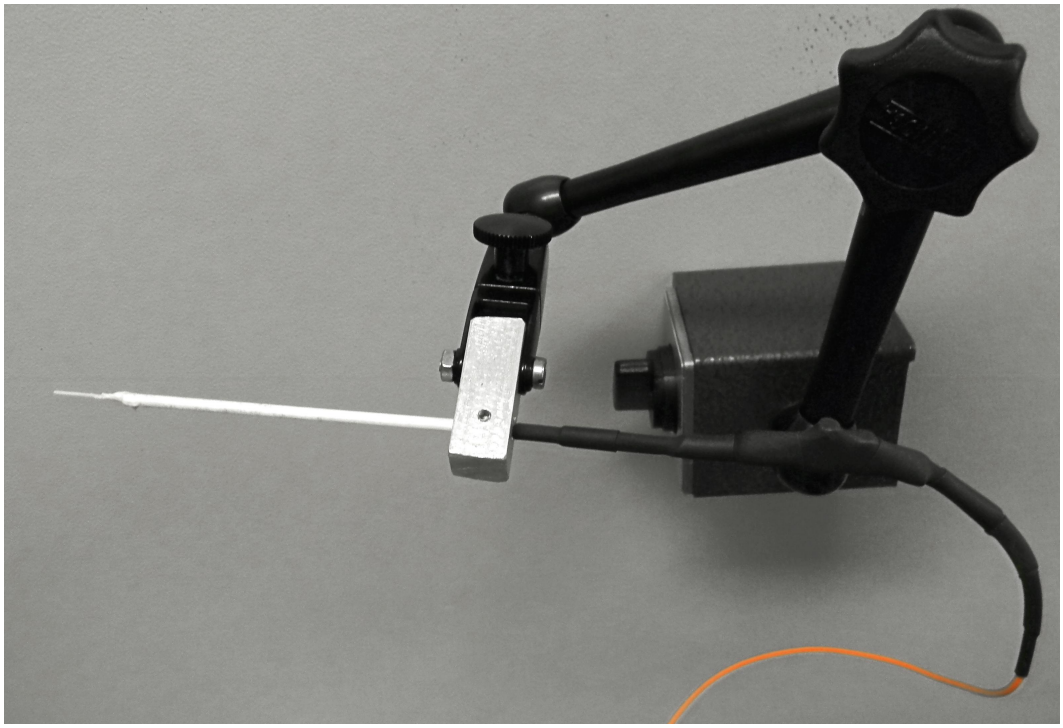

Figure 3.6: A sample Langmuir probe mounted on a magnetic dial gauge holder. The Tungsten probe tip is too small to be resolved in this photo.

### 3.1.4 Langmuir Probe Construction

Almost all of our experiments utilised a Langmuir probe in some way to detect the accumulation of space charge. The Langmuir probes were constructed from ⌀100 $\mu$m Tungsten wire. The wire was threaded through an Alumina ($Al_2O_3$) tube with an inner diameter ⌀0.2 mm and outer diameter ⌀0.8 mm. This Alumina tube was threaded through a larger Alumina tube with an inner diameter ⌀1.14 mm and outer diameter ⌀2.5 mm, and glued in place with Torr Seal® epoxy. The Tungsten wire was allowed to extend 5 mm out of the plasma end of the Alumina tube.

The other end of the tube was anchored with an electrical brass barrel connector. One terminal was used to clamp down on the larger diameter Alumina tube, the other terminal clamped both the Tungsten wire and the external signal wire ensuring a good contact. The entire join was covered with multiple layers of heat shrink to provide electrical isolation. The 15 cm length of large diameter Alumina tube ensured that the insulated barrel connector would not be in contact with the plasma.

The signal wires were connected to a vacuum port where the floating potential could be measured directly, or alternatively connected to the biased probe driver discussed in Section 3.3. The Langmuir probes could be mounted in many ways depending on the desired experiment. Shown in Figure 3.6, a typical Langmuir probe is mounted on a magnetic dial gauge holder.

### 3.1.5 Vacuum Chamber and Mounting

The Teflon Polywell was supported by an aluminium cross beam in the middle of a cylindrical vacuum chamber, which was 420 mm in diameter (see Figure 3.8). The hollow cathode was mounted 10 cm from the Polywell face, and the angle of beam incidence could be varied arbitrarily. The electron beam current and energy could be obtained from the settings on the cylindrical cathode HV power supply. The chamber pressure was measured on a Pirani Gauge accurate to $10^{-4}$ Torr. The chamber was evacuated through an externally connected rotary vane pump and turbomolecular pump which allowed the chamber to be evacuated down to pressures less than $10^{-6}$ Torr. Hydrogen gas was allowed to flow into the chamber using a mass flow controller. By adjusting the mass flow controller any desired pressure between 4 mTorr and 100 mTorr could be achieved. The current in the Polywell coils was measured using a rogowski current transformer [89], model number (IRF/60/D12) [92].

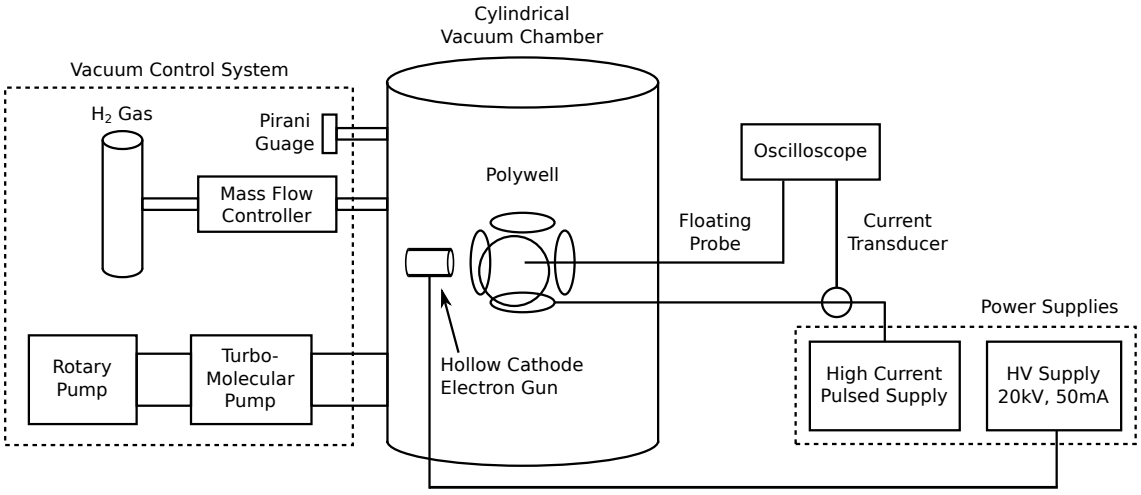


Figure 3.7: A schematic diagram of the experimental setup for the floating probe results. All key equipment and connections are indicated. See the photo in Figure 3.8 for more details of the setup inside the vacuum chamber.

Figure 3.8: A close up photo showing the experimental setup for the Teflon Polywell. The Polywell was mounted in the centre of a cylindrical vacuum chamber with a glass bell jar lid. The cylindrical cathode electron beam is mounted 10 cm away from the Polywell face. It could be moved to make an arbitrary angle with the coil face. The Langmuir probe tip can be seen (small white tip) in the centre of the Polywell. In this experiment, only a single Langmuir probe mounted at the centre of the device was in use. The positions of the red lines indicate the positions of the copper collector plates used in later experiments.

### 3.1.6 Copper Collector Plates

In a later experiment, a copper collector plate was placed around the Teflon Polywell to measure the electron current leaking out of the coil faces. The square copper plate measured 6 cm on each side and was mounted on a long stainless steel rod, insulated by a glass sleeve. The plate was connected to ground through a 100 kΩ resistor, allowing it to float above ground. When placed in the path of the electron beam, the beam current collected was obtained by measuring the voltage across the resistor. The positioning of the collector plates is indicated in Figure 3.8.

In retrospect, the current sense resistor was much larger than necessary. In typical experiments where the collector plate was used, the plate would float to typical voltages of 10-20 V which is not enough to affect the collection of high energy ($>$ 1 keV) electrons from the main cylindrical cathode beam. However it may have affected the current from any low energy electrons produced in the background gas produced by the high energy beam. Results from later experiments indicated that these low energy electrons may have played a significant role in the results and it would have been better to use a much smaller value to limit the plates floating value to $<$1 V.

## 3.2 WB6-mini

### 3.2.1 Design Rationale and Construction

The second Polywell experiment was closer to the design features of Bussard's WB6 Polywell. WB6 represented the culmination of Bussard's research into Polywell physics and was alleged to extend the electron confinement times longer than would be predicted by mirror confinement mechanisms alone through the creation of the wiffle ball effect [69]. Our second Polywell design was intended to bring us closer to WB6 while allowing us to implement a biased Langmuir probe. This new design will be referred to as WB6-mini.

WB6-mini was constructed from 12 Aluminium half torus shells produced with the metal spinning technique. See the schematic for a single shell in Figure 3.9. Each shell had a major radius of 25 mm and a minor radius of 5 mm. Its dimensions were similar to those of the Teflon Polywell. During construction, a sheet of 1 mm thick Aluminium stock was pushed over a toroidal wooden former in a lathe at high speed. This process allows the toroidal ring to be produced quickly and cheaply once the wooden former was made. Many metals can be manipulated with this technique. Although Stainless steel would have been more favourable because of its strength, it would have been much more difficult to manipulate on such a tight curvature. Consequently we chose to use Aluminium sheet for our first design because of its softness and easy working properties.

The WB6-mini Polywell was built in two separate construction phases. A custom made wooden jig allowed careful alignment of each toroidal shell. During the first stage each inner toroidal shell and its pair were individually mounted into the jig and aligned to ensure that each shell was equally spaced from the centre and parallel to its respective cube face. A unique joining pipe piece was constructed for each cubic edge where two shells meet. A dremel and file was used to cut an appropriate radius into each pipe segment to allow mating between the adjoining shells. JB-weld epoxy was used to glue the shells and joining pipes into a single inner frame.

During the next phase the Polywell frame was mounted in a vice with a split-able coil former aligned with a coil axis. A single coil was wound onto the coil former. When finished the former was split in two to enable the coil to be removed and mounted into the toroidal shell. A wire length of 15 m was threaded through the edge tube leading to the next toroidal shell, and then the next coil would be wound. In this way the whole Polywell was wound using a single piece of wire without requiring any bulky connecting terminals between the coil segments. This process was carried out to keep the wire resistance as low as possible, and hence allow the highest possible coil current and magnetic field to be achieved. Once the coil winding was complete, each shell was covered with its mating piece and fencing wire was used in tension to clamp down on the toroidal shells. This allowed easy access to the coils without destroying the frame if future changes were required. A photo during the construction process is shown in Figure 3.11.

The final design and coil spacing schematic is shown in Figure 3.12. The WB6-mini Polywell has a spacing factor of $s = 1.5$, which was larger than the Teflon Polywell and much larger

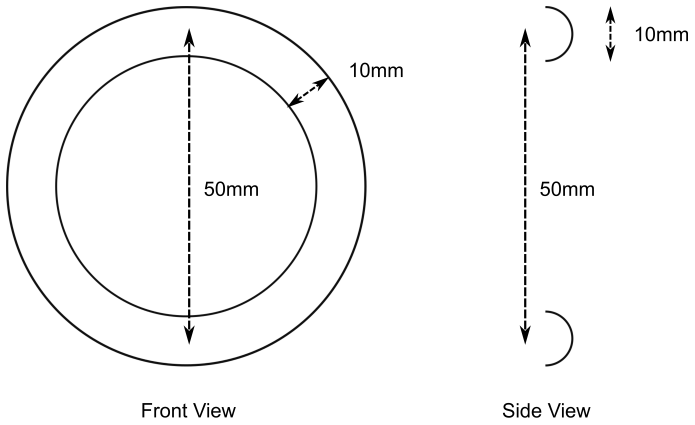


Figure 3.9: The schematic for one of 12 Aluminium half ring Toruses produced with the metal spinning technique.

Figure 3.10: A single coil of 15 enamelled copper wire turns mounted into one of the finished half torus shells.

Figure 3.11: The inner toroidal shells are supported by a custom wooden jig used in coil assembly. The inner toroidal shells are joined with pre-cut pipe segments and JB-weld. On the end of the jig is a split-able coil former. One finished coil can be seen on the far side. A length of 15 m of wire was threaded through the joining pipe so that the next coil could be started. Once the coil winding was complete, the outer shells were clamped onto the frame with tensioned fencing wire.

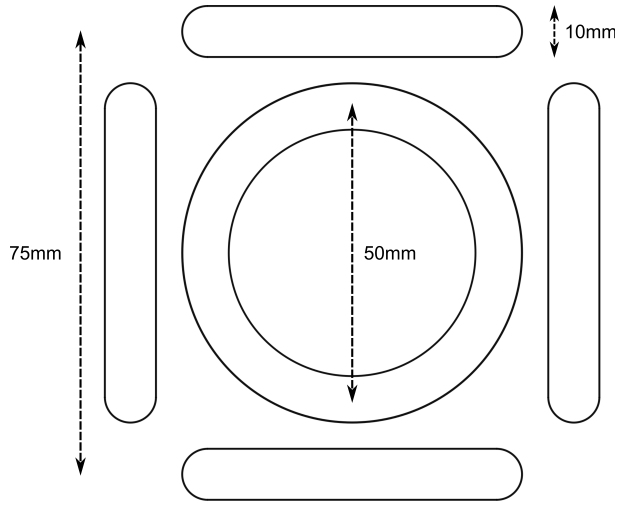


Figure 3.12: The WB6-mini construction dimensions. The joining pipe sections at the coil edges are not shown for clarity. This design has a spacing factor of $s = 1.5$.

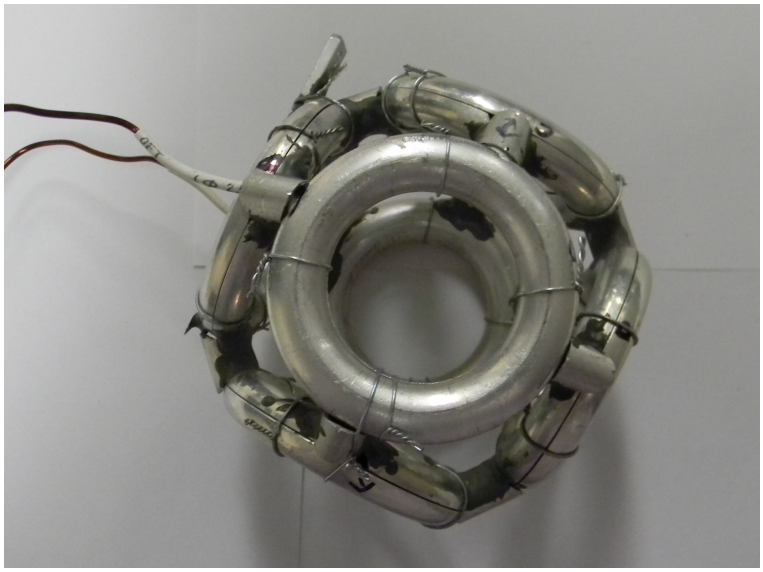

Figure 3.13: A photo of the finished WB6mini prototype

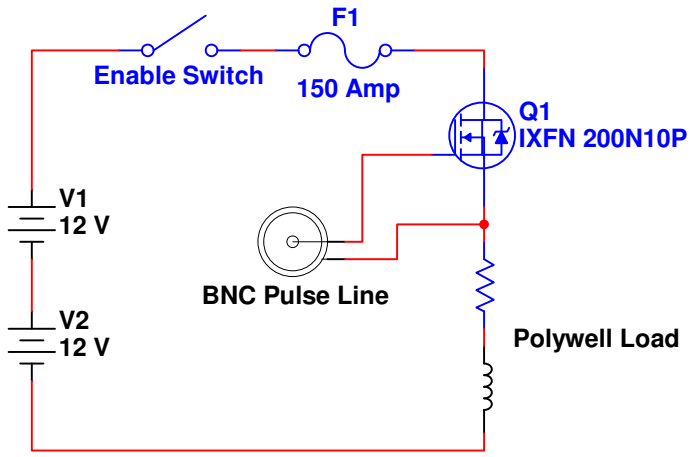


Figure 3.14: The car battery constant current circuit.

than the ideal $s = 1.2$. However, in these early experiments the larger s value was considered secondary to the aim of determining whether there is sufficient confinement in order to achieve any potential well.

### 3.2.2 Constant Current Power Supply

In addition to the pulsed capacitor bank power supply, an additional power supply was constructed to allow constant current and hence constant magnetic field operation. The motivation for adding this functionality is discussed in the results of the Teflon Polywell experiments in Chapter 4. The power supply was constructed from two car batteries in series with a high power MOSFET capable of switching currents up to 60 A. The batteries were recharged with a standard commercially available car battery charger. See Figure 3.14 for the circuit schematic.

This power supply allowed the coil current to be varied from 0-60 A by varying the gate-source voltage on the IXYS MOSFET. The constant current pulse time was controlled by the duration of the gate-source voltage pulse. Our experimental setup typically allowed pulse times of 1 ms up to several seconds. Both power supplies were used interchangeably in the WB6-mini experiments depending on whether a constant B field or high B field were required.

### 3.2.3 Filament Electron Sources

Electrons were supplied through thermionic emission in 12 V 100 W Halogen globes, each drawing 8 A when turned on. The globes were cut open to remove the filament from the glass. A total of six filaments were mounted in the vacuum chamber, each being mounted on a coil axis 2 cm from the coil face. A switch box external to the vacuum chamber allowed each filament to be individually switched into the circuit so that combinations of filaments could be selected for study.

The Polywell shells formed both the extraction and focusing electrodes of a traditional elec-

tron gun, comparable to Bussard's original design concept. The bias applied to the Polywell shells was varied from 20 V to 150 V, providing extraction currents varying exponentially from 10 $\mu$A to 10 mA. The most significant disadvantage of this design is that it does not allow for independent control of the electron beam current and energy.

### 3.2.4 Langmuir Probe Mounting

This experiment utilised two cylindrical Langmuir probes of the same construction as discussed in Section 3.1.4. Both probes were mounted onto magnetic gauge holders to provide easy positioning in 3D. Additionally, Probe A was mounted onto a translation stage with a total travel distance of 5.5 cm and 3 mm increments of movement. The translation stage could be repositioned on any axis in the vacuum chamber. Spatial translation was controlled through a long shaft coupled with two universal joints to an external rotary motion vacuum port. By using two universal joints, linear rotation of angles is approximately preserved. A photo of the translation carriage is shown in Figure 3.15.

For the experiments reported in Chapter 5 Probe A was positioned along a coil axis so that the extremities of translation are the geometric centre of the Polywell and a location just outside the Polywell coils. Probe A made an angle of 8° to the coil axis so that it did not block the filament that emits electrons towards this face of the Polywell. An additional reason for having a small angle is so that the probe crosses more magnetic field lines. Electron transport along magnetic field lines is much faster than cross field transport. This is expected to accelerate space potential build up across field lines and would result in a stronger potential difference than would occur along a point cusp. Probe B was permanently mounted in alignment with a corner cusp and located halfway along the Polywell radius. Both probes were driven from a custom made biased probe driver, discussed in Section 3.3.

A photo of the internal chamber setup is shown in Figure 3.16 and a schematic diagram of the chamber setup with all key equipment and connections indicated is shown in Figure 3.17.

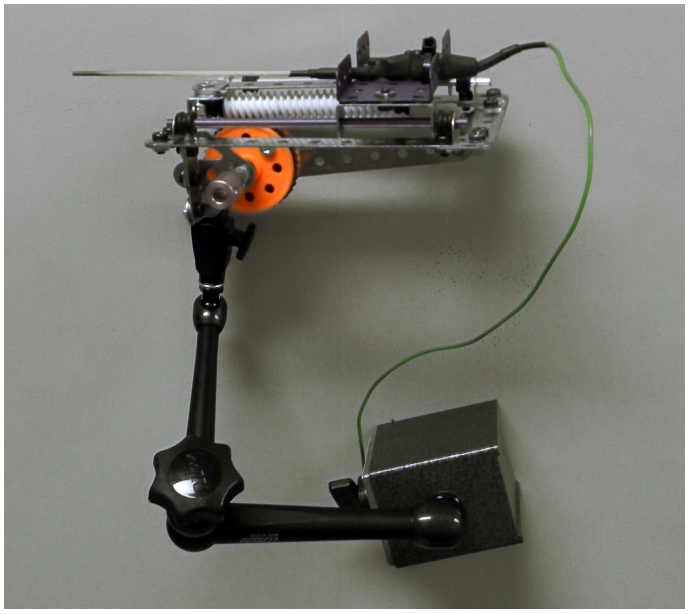

Figure 3.15: The translation carriage for Probe A mounted onto a magnetic dial gauge holder.

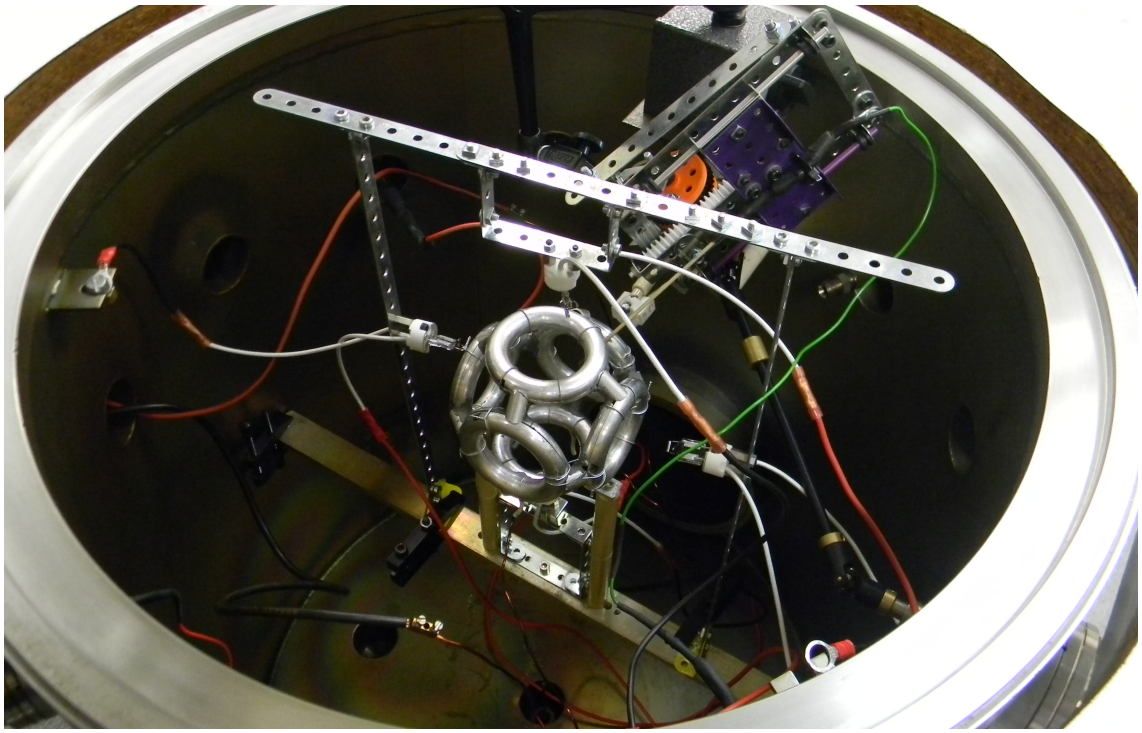

Figure 3.16: WB6-mini mounted in the vacuum chamber with some surrounding filaments. Note that the translational stage had been moved into a corner cusp before this photo was taken.

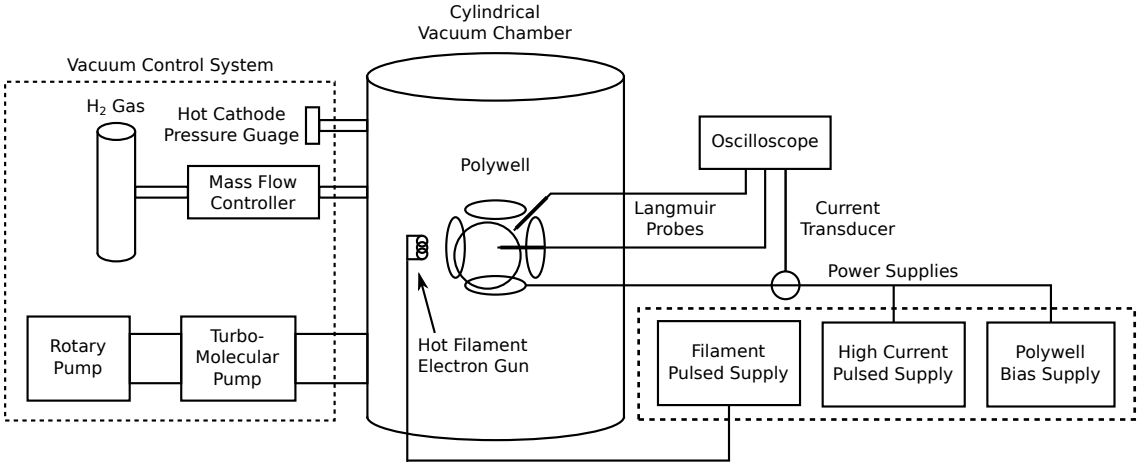


Figure 3.17: The WB6-mini experimental setup showing the key biased probe positions and all relevant electrical connections.

## 3.3 Biased Langmuir Probe Driver

A custom probe driver unit was constructed for making biased probe driver measurements in the Polywell. The unit needed to be able to measure currents as small as 1 $\mu$A in order to accurately measure low electron densities down to $10^{14}$ m$^{-3}$. It also needed to be able to sweep across the full anticipated range of voltages in 100 $\mu$s so that when using the high current pulsed capacitor bank the peak magnetic field would be approximately constant for the duration of a probe sweep.

The final design utilised an Arduino Mega 2560 microcontroller as a programmable function generator [95]. The Arduino was connected to the Freetronics LCD & Keypad Shield allowing various probe functions to be interactively programmed for each experiment pulse [91]. Settings such as the sweep end point voltages, step size and dwell time were all configurable through the LCD panel. The Arduino logic would output an 8-bit digital signal that was converted to a $\pm$10 V analog signal in a DAC module.

The final analog signal was linearly amplified in a high voltage amplifier module by the PA241 high voltage op-amp. Thus the input analog signal proportionally determines all the main sweep features such as sweep time and end point voltages. The full range of the amplifier stage was $\pm$150 V, in a sweep time of 100 $\mu$s. The PA241 has a current limit of 120 mA, which was deemed satisfactory for our experiments. The high voltage amplification module was isolated from the digital input circuits through the INA117 instrumentation amplifier.

Initially this design introduced a significant amount of noise into the circuit because the input signal was digitally switched from one analog level to another at high speed, which was faster than the slew rate of the high voltage op-amp. This had the potential to create excessive noise on the output and interfere with probe measurements. This problem was solved by turning the INA117 and PA241 amplifiers into an active two-pole Bessel filter. This also created a beneficial auxiliary effect whereby the original 8-bit digital input waveform was smoothed to an arbitrary resolution waveform, allowing greater measurement resolution.

The output of the HV op-amp had a current sense resistor, $R_{sense}$, across another INA117 for outputting a voltage signal proportional to the current drawn by the probe. Both the voltage waveform, and the current sense signal were directly measured on a 4-channel Rigol oscilloscope for data display and acquisition. A high level diagram of the main circuit elements is shown in Figure 3.18.

Because the measured probe currents turned out to be very small (on the scale of 1 $\mu$A to 50 $\mu$A) further load balancing techniques were required to prevent measurement errors in the probe current. A compensation resistor, $R_{comp}$, was added to balance the effect of $R_{sense}$ on the INA117 since it has a low input impedance. Additionally, it was found that simply connecting an output coaxial cable for the HV probe signal added a sufficient AC load to give errors in the probe current measured. It was found that for the typical dynamic AC signals being used (the voltage sweep pulse) the current drawn by the cables capacitance was of the same magnitude as the current collected from the electron plasma. Ultimately this problem was countered by adding an additional identically matched coax cable on the other side of the current sense resistor

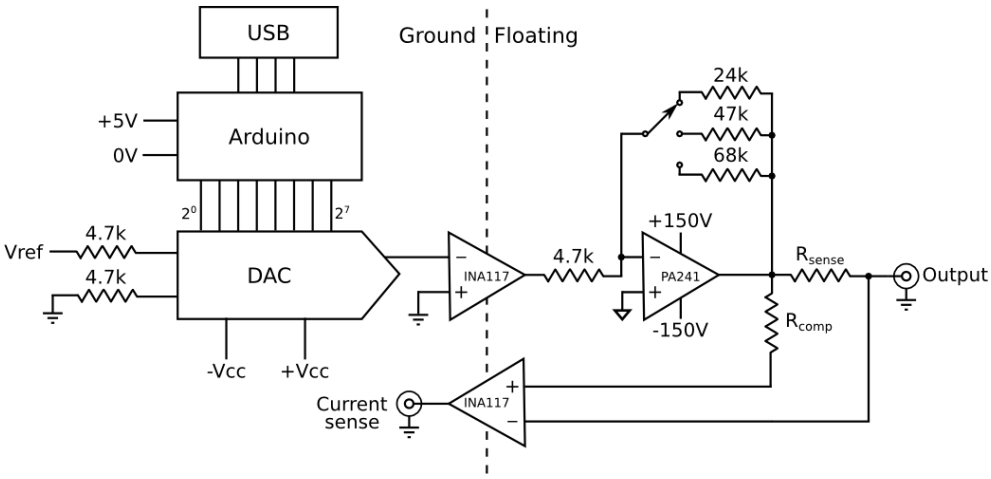


Figure 3.18: A schematic diagram of the biased Langmuir probe driver circuit. The full circuit diagrams are given in Appendix B.2.

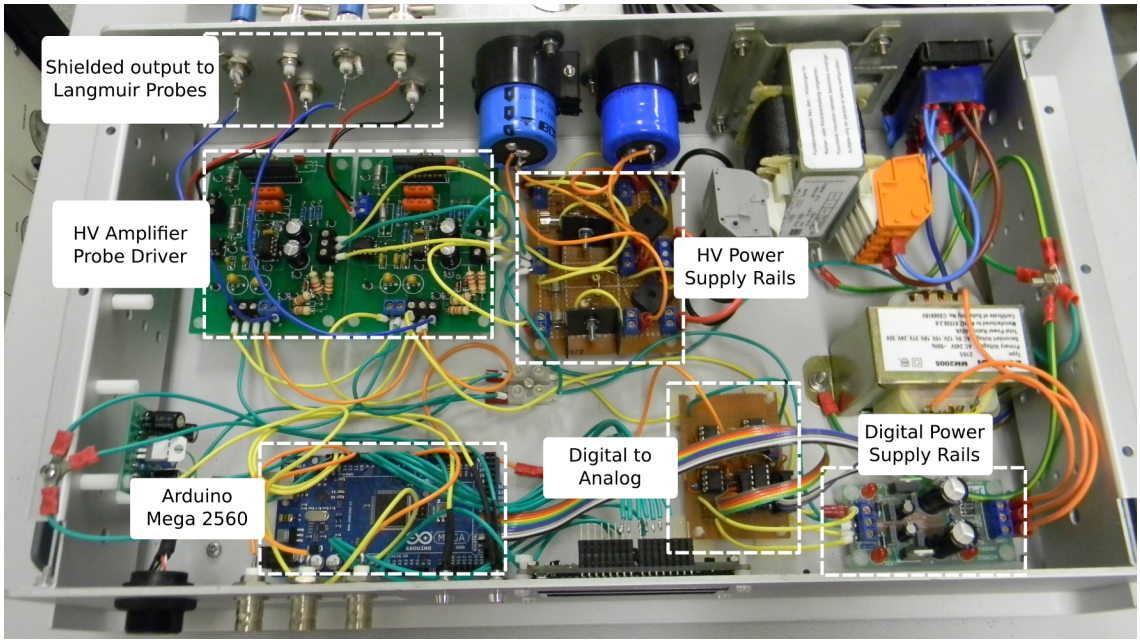


Figure 3.19: A photo of the completed Langmuir probe driver box with its lid removed. Some of the key sub-circuit modules have been highlighted.

$R_{sense}$ so that both sides of the INA117 were identically loaded. The purpose of this additional load was to draw a current through $R_{comp}$ that matches as closely as possible the AC current drawn through the output cable, which is subtracted from the the signal at the + op-amp input. The result was that the INA117 subtracts the error signal from the measured signal thereby cancelling out the effect of the cable loading.

Because of the modular nature of the probe driver design, it was possible to add extra high voltage op-amp modules without requiring any other changes to the circuit. This allowed multiple biased probes to be added to the circuit and swept at the same time. In the biased probe experiments of Chapter 5, two HV op-amp modules were used at the same time to provide measurements in two locations simultaneously.

A sample of the collected data is shown in Figure 3.21, where both the probes bias voltage and current collected are plotted as separate functions of time. Both traces are combined to produce a new current versus voltage dataset. A correction was applied to remove any remaining DC loading offset from the current trace. For example if there was impedance mismatch between the input terminals of the INA117 (and indeed there was), this will introduce a linear offset error in the measured current as a function of voltage. In other words, just as before we added a matched coax cable to account for differing AC loading between the two op-amp inputs, we now need to account for any differing DC loading between the instrumentation amplifier inputs.

A sample trace of probe measurements when no plasma is running is shown in Figure 3.20 showing the expected linear behaviour with voltage indicating a DC impedance mismatch. Using Ohm's law, an offset voltage of 20 mV and an offset current of 20 $\mu$A indicates an error resistance of approximately 1 k$\Omega$, which is well within the expected $< 1\%$ error of the 380 k$\Omega$ resistors included in the INA117 inputs. In future this offset error could be accounted for by including 1 k$\Omega$ trim pots on the current sense op-amp inputs.

After the offset error was removed, the signal was cleaned using both a moving window filter and a Svatsky and Golay filter [103, 107]. The SavitzkyGolay filter is a form of least-square filter where the underlying data within a given moving window is approximated by a polynomial of degree 2 or higher. So for each voltage data point a polynomial was fitted through it and the neighbouring points to smooth out the data.

This method gave two filter parameters that could be tuned, the window size and fitted polynomial order. A larger window size resulted in more smoothing but distorted higher frequency content. In contrast, using higher order polynomials can track narrower features in the underlying data but tend to distort the lower frequency signals. Because our main interest in applying a filter was to discover the underlying $I(V)$ function over the whole voltage domain we were more interested in the low frequency content than the high frequency fluctuations. Therefore, we have chosen to implement a simple second order polynomial with a relatively wide filter window.

A principle advantage of using the SavitzkyGolay filter in biased probe studies over other filters such as the Blackman window or Gaussian filter [103] is that it directly yields the second derivative of the underlying IV signal through the fitted polynomial constants. All one needs to do is extract the fitted constant for the second order polynomial term to obtain the second

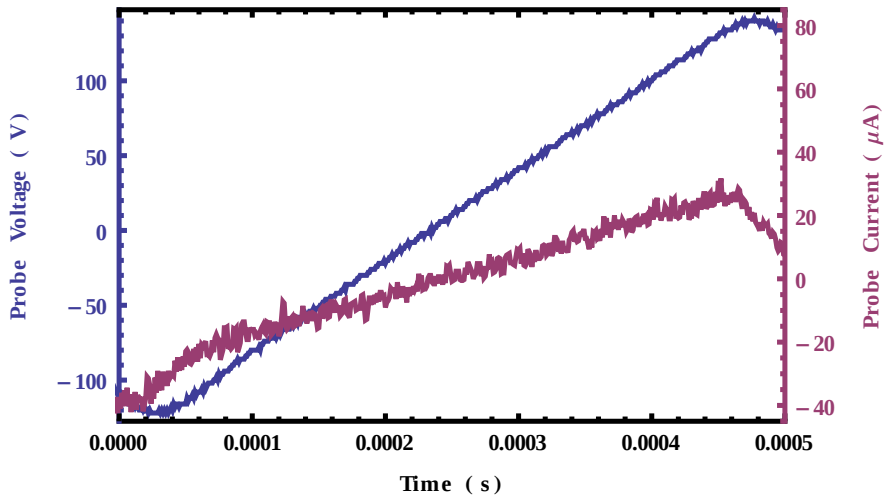


Figure 3.20: An example run with no plasma running. This allows us to measure the DC impedance mismatch on the op-amp inputs. A DC impedance mismatch is evident from the linear change in current with voltage. After measuring this calibration signal we can subtract it from the signal with the plasma running. The fluctuations at the end points of the voltage sweep are AC loading errors appearing when pulsing at high speed. These distortion errors disappear as the sweep is slowed to longer pulse times. For high speed operation, the data range is simply trimmed down to the linear calibration region in software during data processing.

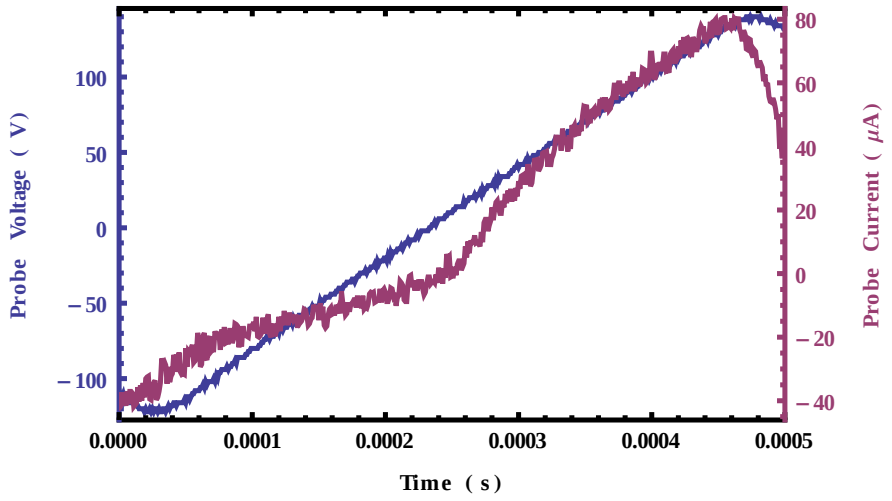


Figure 3.21: Raw data from probe driver with an electron plasma running before subtracting the calibration signal and filtering is applied. The sweep parameters are exactly the same as in Figure 3.20.

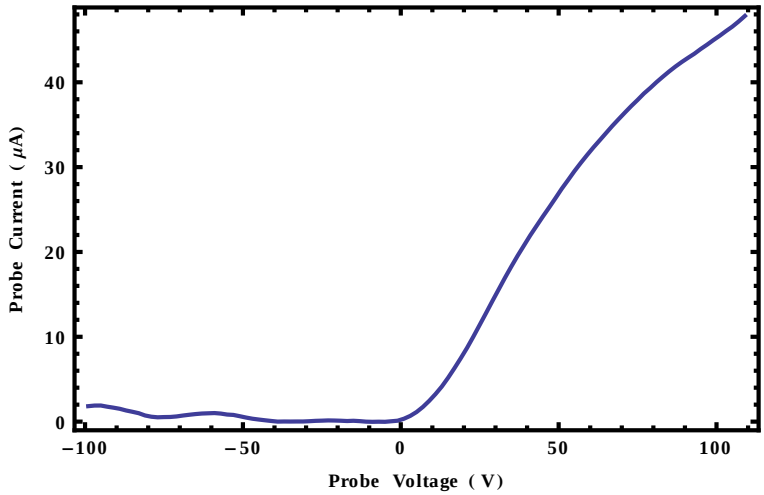


Figure 3.22: An example of the recovered underlying $I(V)$ function after the data had been filtered and corrections to the offset current had been applied.

derivative at each voltage point. This is particularly useful for diagnosing the electron energy distribution function in isotropic plasmas. However it is only useful if you can confidently determine the plasma potential, which is of course a central goal of this thesis.

A significant disadvantage of the SavitzkyGolay filter is that it introduced distortion into the original function at the start and end points of the data where the full window was not available for fitting [103]. Therefore, these points were discarded in the filtered function and the resulting $I(V)$ data range was smaller than that measured with the probe driver. For example, after the combined moving window and SavitzkyGolay filters were applied, a data set measured from $\pm 140$ V was only usable over the range $\pm 110$ V. An example data set after all filtering, offset corrections and range trimming is shown in Figure 3.22.

## 3.4 Confinement Time Clamp Circuit

A final goal of our experiments was to measure the confinement time of the confined electrons inside the Polywell. A typical method for measuring the plasma confinement time in a fusion device starts with sustaining a plasma in normal operating conditions [60]. After some arbitrary time of stable operation the plasma source is sharply cut-off and a Langmuir probe can be used to measure the decay of plasma current in time. The time for the measured probe voltage/current to decay by a factor of $e$ is taken to be an approximation of the real plasma confinement time.

In the WB6-mini Polywell, the most logical way to implement this measurement is to clamp the Polywell's bias voltage to ground in a very short time. Grounding the Polywell bias voltage essentially removes the extraction and acceleration electric fields for the thermionic electron source, and hence the injected electron current is expected to fall to zero very quickly. By keeping the magnetic field constant during this period, the electrons in the Polywell are only contained by mirror reflection with the point cusp fields and the decay in probe current/voltage should give an accurate representation of the average electron confinement time.

For this purpose a custom made clamp circuit was made to allow clamping of the bias voltage to ground in less than 100 ns. The circuit utilised a classic "push-pull" design where two FETs were used to temporarily pull the $V_{bias}$ line down to ground when a pulse is supplied to the pulse transformer. A circuit diagram is shown in Figure 3.23. In normal DC conditions Q1 is on and Q2 is off, and thus the Polywell bias voltage $V_{bias}$ is connected to the +150 V supply line. However during an AC transient on the input pulse line, the situation is reversed and Q2 pulls $V_{bias}$ down to ground. Q1 is turned off so as not to short the HV power supply to ground. A sample trace of the clamp circuit in operation is shown in Figure 3.24.

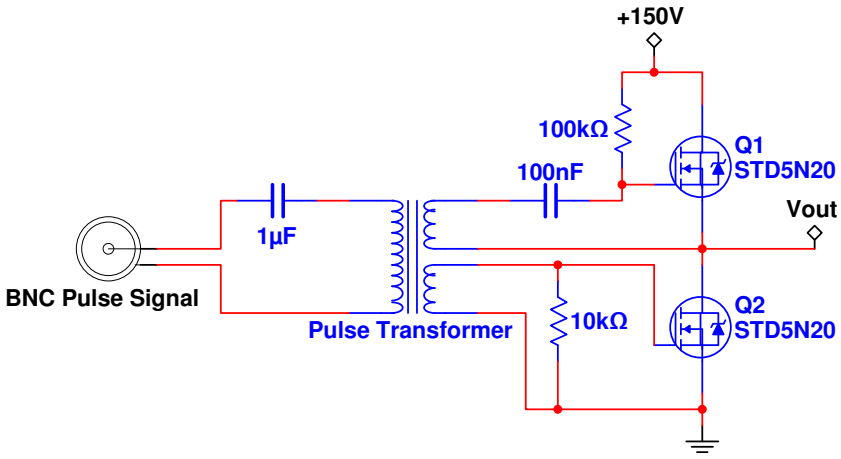


Figure 3.23: The push-pull clamp circuit [90, 93, 94, 96].

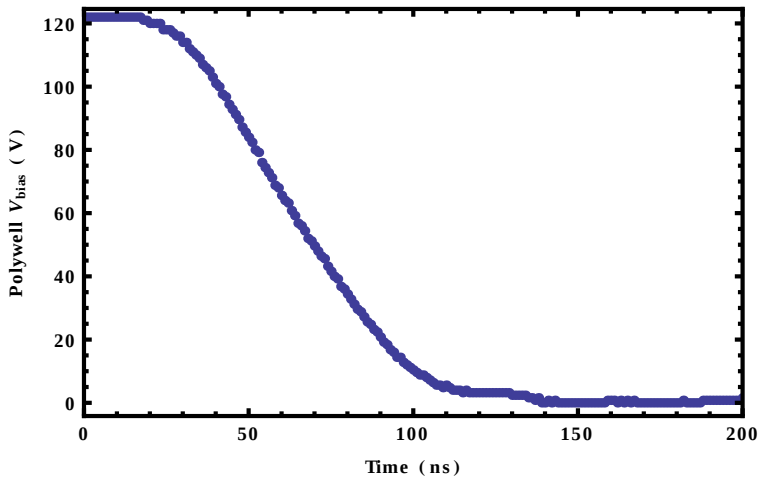


Figure 3.24: A sample trace showing the fall in the Polywell bias voltage $V_{bias}$ when a transient logic pulse is applied to the clamp circuit. In this example the Polywell $V_{bias} = 120$V and was clamped to ground within 60ns. This is well within the required tolerance for measuring electron confinement times in the Polywell.

Chapter 4

# Floating Potential Measurements in a Teflon Polywell

The Teflon Polywell was our first prototype device aimed at obtaining at least qualitative validity of the Polywell concept in establishing a potential well. As described in detail in Section 3.1, the Teflon Polywell was mounted in the middle of a cylindrical vacuum chamber with electrons provided by a cylindrical hollow cathode discharge beam. The dependence of potential well formation on magnetic field strength, background gas pressure and electron injection energy and current has been measured. Potential well formation as a function of magnetic field strength was measured by varying the current in the Polywell coils. Floating potentials of up to –250 V were obtained for periods of several milliseconds, suggesting the formation of a virtual cathode stable on at least the millisecond time scale.

## 4.1 The Floating Potential as a Diagnostic for the Plasma Potential

For this experiment, a single ended Langmuir probe was mounted in the geometric centre of the Polywell and used to measure the plasma floating potential, $V_f$. In this initial study, the floating potential was used as a qualitative parameter for indicating the existence of a virtual cathode and its lifetime. The floating potential can be used in this way because $V_f$ is often taken as an indicator of the plasma potential, $V_p$ [98, 105, 108].

In a typical low energy plasma in thermal equilibrium, the floating potential is determined by the balance of electron and ion currents to the probe. Since the electron temperature is usually greater than the ion temperature, $T_e > T_i$, the relationship between the floating potential and the plasma potential is often only determined by the electron temperature $T_e$. And hence knowledge of the electron temperature is needed to relate the floating potential to the plasma potential.

However, when there is an energetic electron population in a background plasma, such as primary electrons or the presence of an electron beam, the floating potentials relationship to the plasma potential can be dominated by the beam energy $E_b$. For example, Hershkowitz has shown [101] that when $E_b \gg T_e$ and the beam density $n_b \ll n_e$, the current balance at the surface of a planar probe can be solved to yield

$$q(V_f - V_p) \approx -E_b. \tag{4.1}$$

This means that the deviation of the floating potential $V_f$ from the plasma potential $V_p$ is only related to the primary beam energy $E_b$ under these conditions, and even allows evaluation of the plasma potential by knowing only the beam energy $E_b$.

However, the conditions of our plasma may lead to a more complicated relationship between $V_f$ and $V_p$. No further interpretation of the results can be made at this stage because the Electron Energy Distribution Function (EEDF) is unknown and the discharge may not satisfy the quasineutrality condition since electrons are being injected into the confining space. The pulsed nature of the electron confinement introduces a non-locality to the Langmuir probe measurement, and thus presents a limitation on spatial resolution. In addition, the magnetic field further confounds the analysis because its presence leads to increased ionisation by increasing the total path length of the electrons. The combination of these factors makes probe data difficult to analyse without a detailed understanding of the underlying plasma parameters such as the EEDF.

Because of the way the floating potential is related to the plasma potential, changes in the floating potential with time can be seen as indicative of a change in the plasma potential and may indicate a build up or decay of space charge. However, there is no way to use the floating potential to calculate the plasma potential without a detailed knowledge of the EEDF and the electron and ion densities. Thus the principle aim of this set of experiments is to measure a change in the floating potential that is indicative of a change in the local space charge and may be evidence for a potential well. Negative changes in the floating potential in the confining region will be referred to as a potential well, but a truly decisive measurement of the potential well depth will be left for the biased probe analysis in Chapter 5.

## 4.2 Electron Confinement Predictions

Although this experiment is physically much smaller in scale than the original experiments by Bussard and Krall (in particular the HEPS experiment [81] and later WB6 [69]), the coil and power supply parameters have been designed to be in the same magnetic field regime. In the WB6 experiments the peak fields in the cusps were typically on the order of ∼0.15 T [69, 81], whereas in the smaller scale Teflon Polywell described in this thesis the peak field in the cusps is ∼0.25 T at currents of order 2 kA and ten turns of wire in each coil, which was slightly larger than in WB6. However our Polywell is not intended to operate in a high density wiffle ball mode. Additionally, in a larger device the field is not required to be as high in order to obtain the gyroradius needed for good confinement properties. Hence a lower field is required for the larger device to produce equivalent electron confinement.

Based on the low beta model of electron confinement developed in Chapter 2, it is possible to predict the upper bound of electron energies that start to be confined at a given magnetic field strength, parameterised through the coil current. It was concluded in Chapter 2 that the upper bound for electron energy confinement is reached when the electron gyroradius equals 10% of the device radius at a location half way along the face cusp ($r_g(KE, B) = 10\%R_D$). This

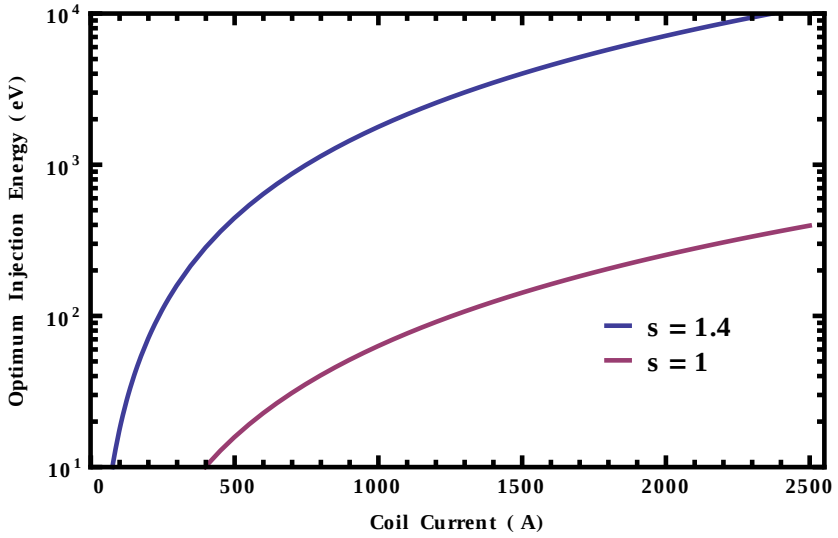


Figure 4.1: The upper bound on confinement energies for the low beta Teflon Polywell, calculated for two different coil spacings. For a given coil current and coil spacing the plotted curve gives the upper bound for electron energies that start to be well confined. In reality there is no distinction between confined and not confined. Instead it is only possible to talk about the degree of confinement and the energies for which electrons in the ensemble start to become "well confined". It was concluded in Chapter 2 that the upper bound for electron energy confinement is reached when the electron gyroradius equals 10% of the device radius at a location half way along the face cusp. Hence our definition for when an electron starts to be "well confined" is $r_g(KE, B) = 10\% R_D$.

equation has been solved for $KE$ and is plotted in Figure 4.1 as a function of coil current in the Teflon Polywell.

Figure 4.1 is highly nonlinear because the $r_g \propto KE^2$. The energy range of the hollow cathode electron beam is 6.5 keV up to 15 keV and thus we expect that the lower energy range of the electron gun should at least produce a small number of mirror reflections in a fraction of the beam population. The equation has been solved for two different coil spacings to highlight the importance of including coil geometry in the calculation. As shown in Figure 2.12 from Chapter 2, there is a nonlinear reduction in the peak field in the coil face due to field cancellation from neighbouring coils. If the calculation is initially carried out with no coil spacing ($s = 1$), the field in the coil face is too weak such that no beam deflection is predicted. However when one allows for coil spacing, the field in the coil face becomes sufficiently large to produce some mirror reflection effects.

## 4.3 Floating Potential Measurements

### 4.3.1 Well variation with magnetic field strength

The first example of a floating potential well measurement is shown in Figure 4.2. For this set of experiments electrons were injected at a constant energy of 15 keV and a current of 2 mA. The background gas pressure was held constant at 25 mTorr of Hydrogen to achieve the correct breakdown conditions for these electron beam parameters. In this experiment the peak current of the pulsed power supply was varied from its low range at ~250 A up to a peak of ~2.5 kA. Only the first pulse is shown on its own in Figure 4.2 for clarity. In Figure 4.3, four different floating potential traces from the same experiment are shown, each with evenly spaced increments in the peak field intensity.

It is shown in Figure 4.2 that a deep floating potential well has been observed when the magnetic field is applied. However there are a number of unexpected results in Figure 4.3. First, the deepest potential well minimum was observed with the lowest current pulse. Without further analysis, this appears to contradict the ideas developed in Chapter 2. Second, the minimum in the floating potential moves out of phase with the peak of the current pulse.

In Figure 4.2 the peak current was 250 A, at the bottom of the possible pulsed power supply range, giving a peak field of approximately $B_{max} = 0.038$ T. A steep drop in the floating potential is observed when the magnetic field is pulsed, indicative of a negative change in the plasma potential. The drop in floating potential of 200 V is 1.3% of the possible well depth based on beam energy alone. However, comparing the experiment parameters with the theoretical model calculations in Figure 4.1 the magnetic field is too low to be producing significant mirror confinement at the beam energy.

In Figure 4.2, using $B_{max} = 0.038$ T and energy of 15 keV gives a minimum electron gyroradius of $r_g = 1$ cm. The length scale for spatial change in the magnetic field is smaller than $r_g$ and hence the adiabatic condition of Equation 1.4 is not satisfied which predicts a negligible amount of mirror reflection. However, the largest magnetic field in Figure 4.3 has a

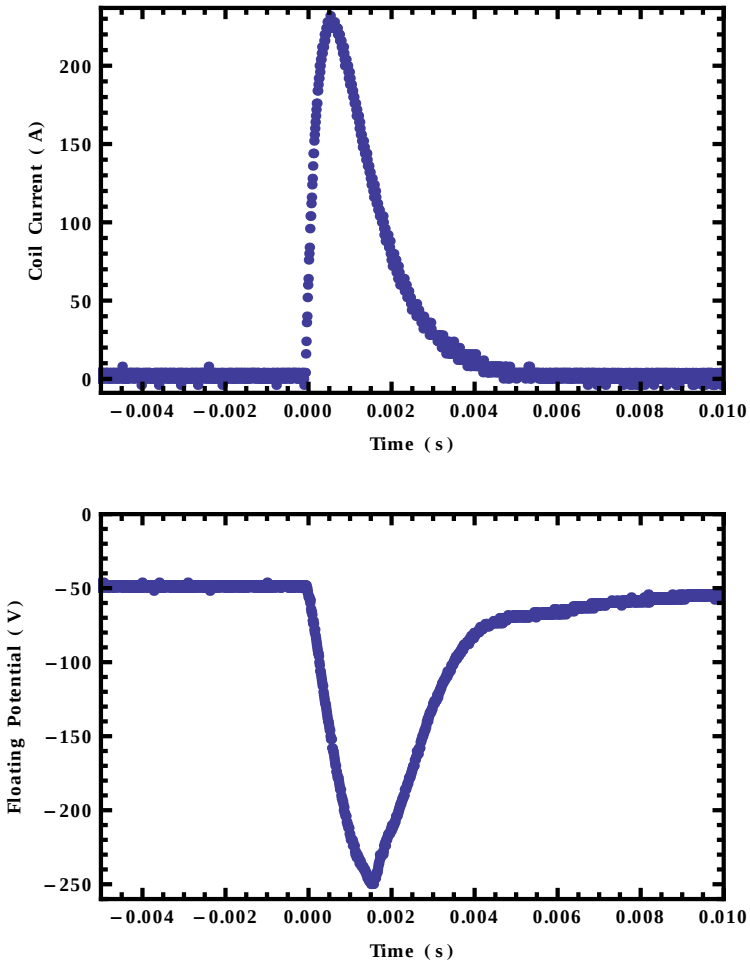


Figure 4.2: A sample measurement of a floating potential well. This particular trace was collected with a beam energy of 15 keV and current of 2 mA. The background gas pressure was 25 mTorr of Hydrogen. The peak current was 250 A, at the bottom of the possible pulsed power supply range, giving a peak field of approximately $B_{peak} = 0.038$ T. A steep drop in the floating potential is observed when the magnetic field is pulsed, indicative of a negative change in the plasma potential. The drop in floating potential of 200 V is 1.3% of the possible well depth based on beam energy alone. However, comparing the experiment parameters with Figure 4.1 the magnetic field is too low to be producing significant mirror confinement at the beam energy.

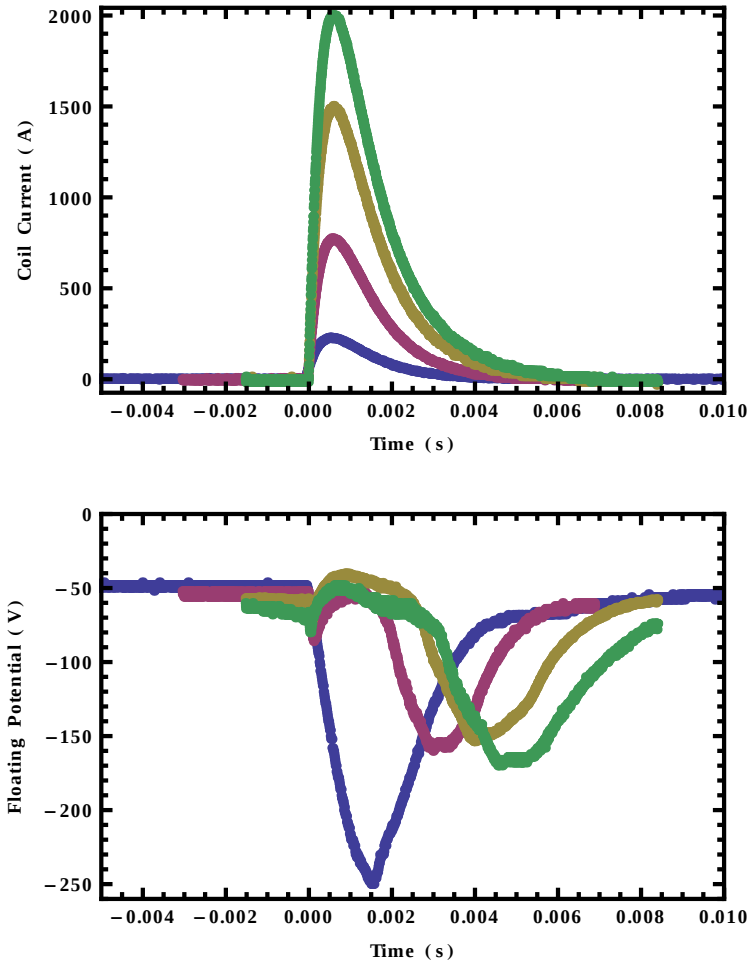


Figure 4.3: The change in floating potential with increasing magnetic field B. These data sets all have the same experimental parameters as Figure 4.2, which is the blue set of traces in this figure. There are two results in this Figure that were unexpected. The first is that the deepest minima in the floating potential was actually observed with the lowest current pulse, and hence the lowest magnetic field strength. Without further analysis, this appears to contradict the ideas developed in Chapter 2. The second unexpected result is that the minima in floating potential moves out of phase with the peak of the current pulse.

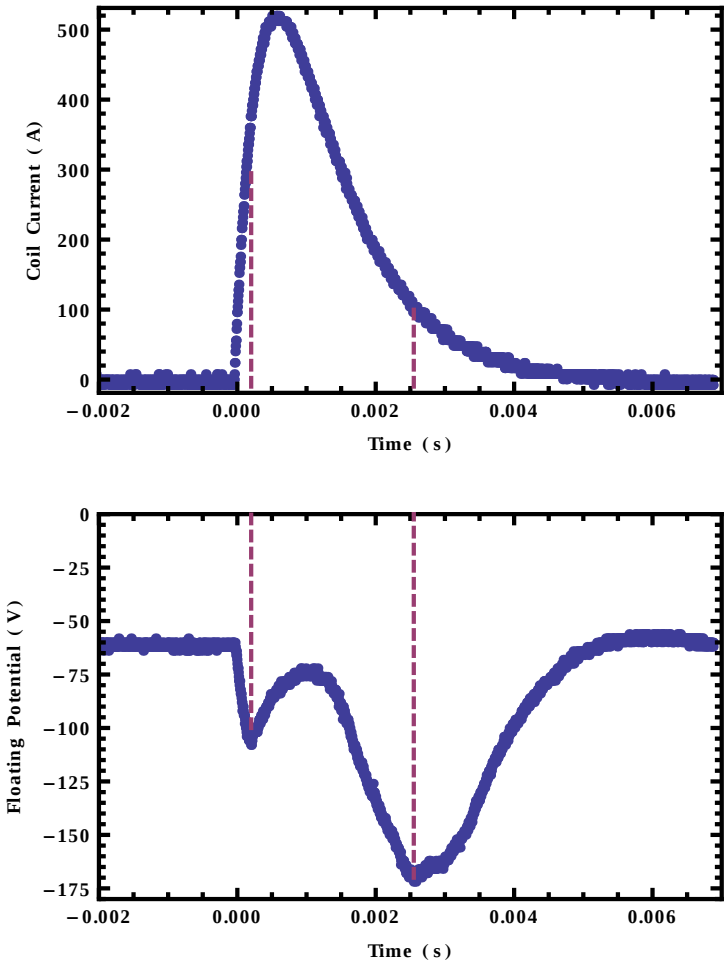


Figure 4.4: A comparison of the floating potential well minima times. This data set occurs between the data sets of Figure 4.3 where the floating potential well starts to move out of phase with the peak magnetic field. The minima in the floating potential occur at different currents depending on whether the current is rising or falling. The floating potential well is approximately twice as deep when the timescale of change in coil current is approximately twice as long. This observation suggests a highly dynamic situation and the plasma may not have reached equilibrium and may be due to the ionisation of the background gas affecting the floating potential well measurement.

peak field in the face cusp of $B_{max} = 0.31$ T, giving a gyroradius of $r_g = 1.3$ mm. The rate of magnetic field change over the length scale of 1 mm is small near the face cusp and therefore the adiabatic condition should be satisfied under these conditions. Hence it is expected that there will be an increase in confinement time with an increase in the magnitude of the magnetic field, thus resulting in deeper wells than those shown in Figure 4.3.

The phase difference in the floating potential minimum and the coil current maximum may mean that there is a narrow range of magnetic fields for which the largest potential well depth may be achieved. An example data set shown in Figure 4.4 reveals that the floating potential well was observed during the rise and fall of the magnetic field, but was depressed during the peak magnetic field. A comparison of the minima times suggests that the experiment is highly dynamic and may not be in an equilibrium state. This implies that the observed phenomena occur on the ion time scale, and may be due to the movement of ions after ionisation by the energetic electrons.

In order to study the change in floating potential well with increasing magnetic field, a 3 Ω high power resistor bank was added in series with the Polywell to dump power and provide a lower operating range of current pulses. With this change, the pulsed power supply could provide current pulses with peak currents over the range of 0 to 200 A. Figure 4.5 shows the two types of floating potential measurements observed in the reduced measurement range. For each current pulse shown in Figure 4.5 (a), there is a corresponding potential well profile displayed in Figure 4.5 (b). For each potential well measured, the minimum point and the time that the minima occurred with respect to the current pulse are recorded in Figure 4.6.

In the low magnetic field range from 0 to ≈100 A, there is a non-linear increase in the potential well depth in Figure 4.6 (a). Moreover, Figure 4.6 (b) shows that the minima of these wells are in phase with the peak current pulse in the coils. The floating potential wells measured over this range exhibit the predicted behaviour. However, for currents greater than ≈100 A there is a sharp change in behaviour as the floating potential minima are of approximately constant depth. Additionally, the floating potential wells in this second current range drift linearly out of phase with the current pulse.

For the pulses that subsequently drift further out of phase with increasing coil current, the appearance of the minima always coincides with the transition current of 100±10 A, leading to the interpretation that this threshold is the peak magnetic field above which potential wells are no longer stable. When the peak magnetic field (and the equivalent coil current) is above this threshold, potential well formation is generally not observed until after the field has decayed down to the threshold value, producing an apparent phase shift.

A possible explanation for the observed magnetic field threshold is that the magnetic mirror effect will be active from both inside and outside the Polywell. When the magnetic moment, $\mu$, is invariant, the condition for reflection in a magnetic mirror [43] is approximately dependent on the ratio of the relative magnetic field strengths,

$$\frac{B_0}{B_{max}} = \sin\theta_m, \tag{4.2}$$

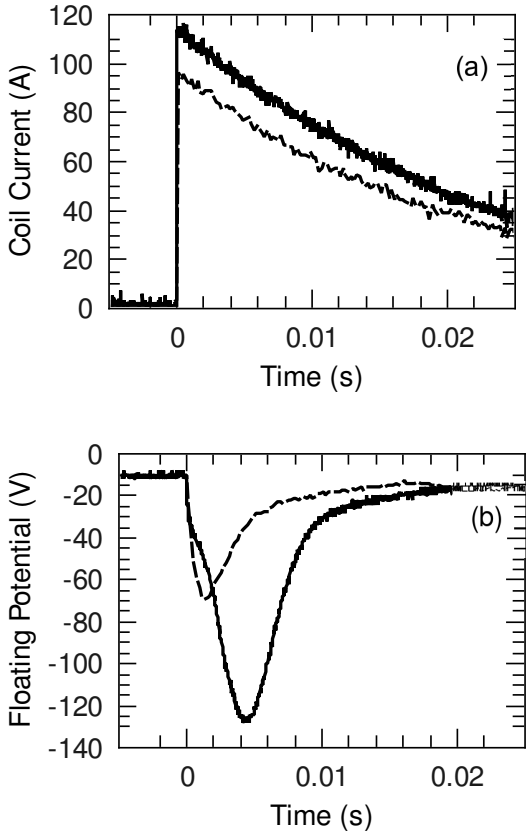


Figure 4.5: Two typical potential well profiles in the low current range. For a given current profile shown in (a) the corresponding potential well measured on the langmuir probe is shown in (b).

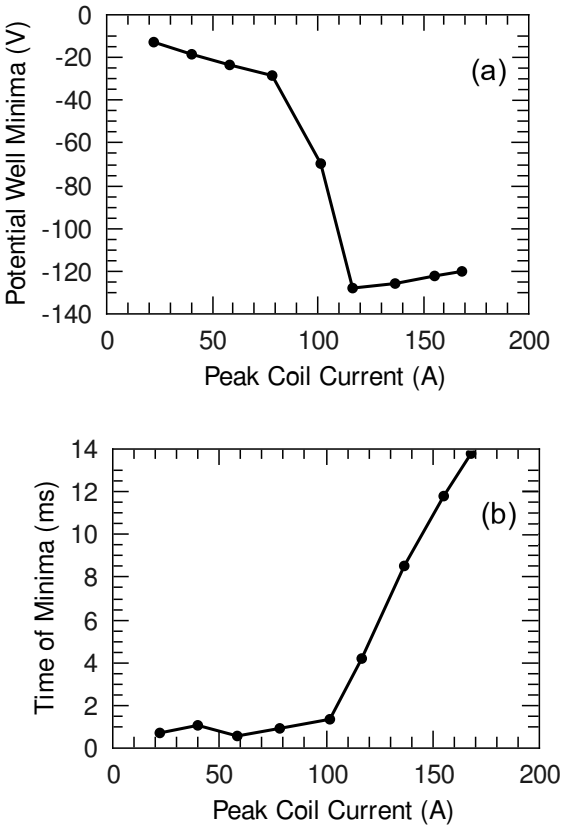


Figure 4.6: (a) displays the minimum well depth observed as the peak coil current is varied from 20A up to 170A. For each current pulse measurement in (a), the corresponding time of the well minimum is plotted in (b).

where $B_0$ is the weakest magnetic field point at which adiabatic condition (Equation 1.4) is satisfied [64], and $B_{max}$ is the peak magnetic field located in the centre of the Polywell's coils. Particles with a velocity vector that makes an angle less than $\theta_m$ in the weak field region will be lost from the region. In phase space, this angle defines a cone, known as the loss cone. Particles with a velocity outside the loss cone, are reflected from the coil face back into the centre of the device.

However, note that the mirror ratio equation (4.2) is only dependent on a difference between the magnetic fields and hence also applies to the magnetic mirror outside the Polywell. The injected electrons are initially far away from the Polywell, but as they approach the coil faces they eventually transition into a region where inequality equation 1.4 is satisfied and $\mu$ is invariant. In this context, the loss cone actually defines the velocity space of electrons that can enter the Polywell. A fraction of the injected beam will have velocities outside the loss cone and are hence reflected from the Polywell coil face. Consequently, there will be a threshold point where a potential well can no longer form since a substantial portion of the injected electron beam is now reflected and no-longer enters the device, which would explain the observed phenomena. Nonetheless, this explanation would be unlikely to explain the data unless there is a second population of electrons at a lower energy than the primary beam. As discussed previously, the injected electrons in Figure 4.2 have a gyroradius too small to produce significant mirror reflection. Hence, in Figure 4.3 we would expect to see an improvement in the confinement time and an increase in potential well depth before seeing a decrease due to reflection of the incoming beam.

Another possible reason for the unexpected change in behaviour is that the relationship between $V_f$ and $V_p$ is far more complicated than given in the assumptions of section 4.1 at the start of this chapter. The ability to analyse the changes in $V_f$ as approximately following changes in $V_p$ is dependent on there being a simple relationship between $V_f$ and $V_p$. Hershkowitz and others have shown that when secondary electron emission from energetic primary electrons is present the floating potential can be multi-valued [101, 105]. An example studied by Nam et. al. [105] with a primary electron energy of $E_p = 300$ eV and background plasma electron temperature of $T_e = 6$ eV yielded three possible floating potentials. The resulting floating potential measured was found to be dependent on the initial bias of the probe with respect to the plasma. Such effects could significantly complicate the floating potential probe analysis and only a detailed knowledge of the EEDF can clarify the relationship between $V_f$ and $V_p$.

### 4.3.2 Dependence on electron injection energy and current

The voltage on the cylindrical hollow cathode could be varied from voltages of 6 kV to 15 keV. At each voltage, the plasma breakdown characteristics change such that the electron beam energy increases with cathode voltage. Additionally, the beam current increases exponentially with increasing cathode voltage. In the previous section, the floating potential well minima were measured over a wide range of current pulses, as in Figure 4.3. This experiment was repeated over three different sets of hollow cathode beam parameters, the results are shown in Figure 4.7.

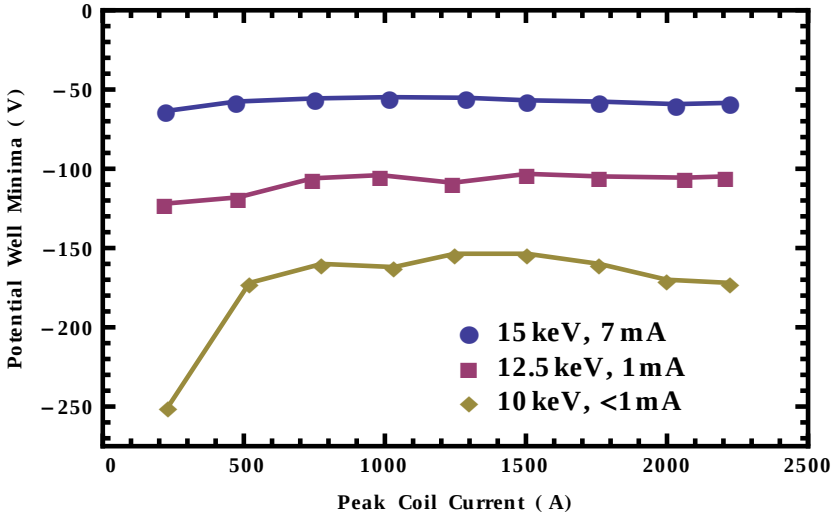


Figure 4.7: The effect of the electron injection energy and current on the potential well minima. For each set of electron injection parameters, the magnetic field was varied over a wide range of coil currents. The data show that the beam current has a much larger effect on the floating potential minima than the magnetic field or beam energy. See text for details.

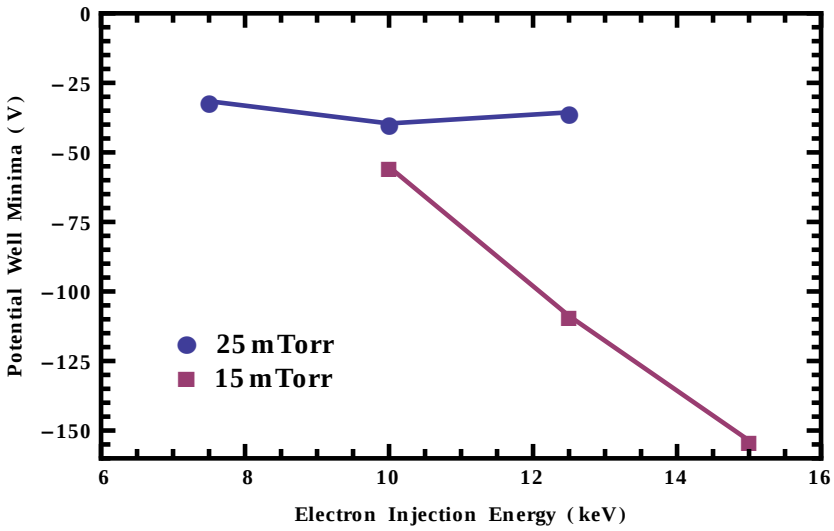


Figure 4.8: Well depth as a function of injection energy, at a constant coil current of 625±25 A. Data was measured at two different pressures, 15 mTorr and 25 mTorr. Well depths at 35 mTorr were deemed too small to be significant.

For each current pulse, the minimum of the well is recorded and plotted with its peak current value, each set of values making a data point.

Figure 4.7 shows that the electron beam injection parameters have a much greater effect on the floating potential wells than the magnetic field. Of the two beam parameters, injection energy and current, the injection current is likely to be the more significant factor for determining the size of the well minima. This is for the same reasons as discussed in the previous section, the primary beam energy is simply too big to show no variation in well minima over such a wide range of currents. Furthermore, increasing the electron energy would be expected to give less mirror reflection and hence produce a decrease in the well depth, but the opposite of this behaviour is observed. An increase in the beam current would lead to an increased electron density in the device, and hence the variation across the data sets in Figure 4.7 can be accounted for by the change in injected beam current.

### 4.3.3 Dependence on gas pressure

Potential well formation as a function of injected electron energy was measured at three pressures (15 mTorr, 25 mTorr and 35 mTorr), whilst keeping the peak coil current constant at 625±25 A. Figure 4.8 shows the results for only two lower pressures, since potential wells completely disappeared at 35 mTorr in all data sets. As pressure is decreased from 25 mTorr to 15 mTorr, the potential wells are consistently deeper, suggesting that the achievable well depth is dependent on pressure.

Increasing the gas pressure will decrease the mean free path of the electrons, which means they collide more frequently with other particles and lose energy. Additionally, there is an increased rate of ionisation which creates an electron and ion pair. If a potential well is present the electron is repelled away from the well, whereas the ion is attracted into the well. Therefore increased ionisation is actually detrimental to potential well formation since the newly created low energy ions will reduce the well depth. In our experimental setup, potential wells became small (on the order of volts) at pressures above 35 mTorr.

## 4.4 Collector Plates

The collector plate experiment was designed to confirm that the prototype Teflon Polywell is working correctly and generating the intended magnetic field effects. It was essential to construct experiments that can establish the correct mode of behaviour is occurring, and aid in preliminary diagnosis of the plasma confinement. This experiment was designed to exploit the anticipated behaviour differences between before and during application of the Polywell's unique magnetic confinement geometry.

When the magnetic field was not turned on, the incident electron beam would pass straight through the Polywell and $I_{in} = I_{out}$. In this case the full current entering the Polywell was expected to leave through the coil directly opposite. If however the magnetic field was applied and, consequently produced the intended confinement behaviour, the magnetic field would lead

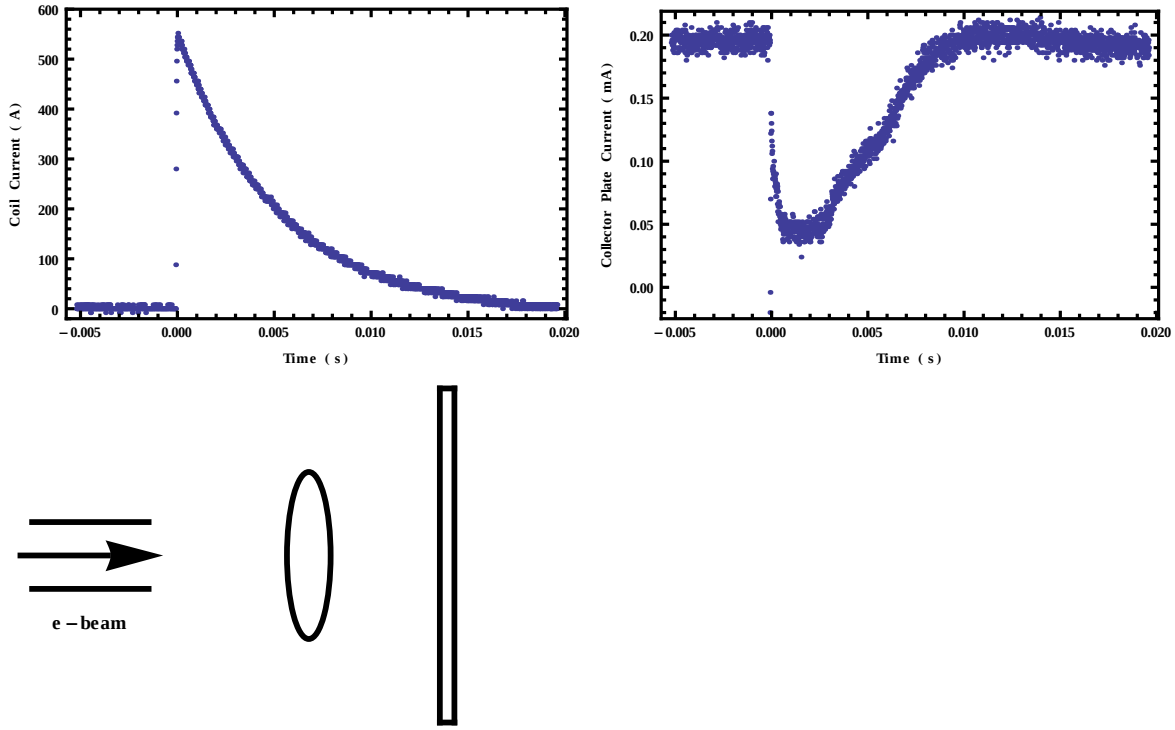


Figure 4.9: The collector plate behind a single coil test case. The current pulse to a single coil is shown in the top left Figure. In the top right Figure is shown the current collected by the collector plate, behind the electron beam. When the magnetic field is highest, only a small fraction of the incident beam is in the loss cone and allowed to pass through the coil.

to an increase in the electron dwell time. This would result in the build up of electron space charge (and the formation of a potential well) until a new equilibrium state is reached where once again $I_{in} = I_{out}$. Except in this new equilibrium state the beam current entering through a single coil face is redistributed through all the other point cusps by the non-adiabatic magnetic null.

The collector plate experiment was designed to measure the current leaking out of a coil face, and hence detect the re-distribution of leakage current when the Polywell is operating in its intended mode. No attempt was made to separately analyse the current leaving Polywell face cusps and corner cusps. Instead, the collector plates were made sufficiently large to cover an entire cubic face, such that any current leaving a coil face or the corner and edge cusps of that cubic face would be expected to be collected by the plate.

The first example shown in Figure 4.9 considers the case of a single coil with a collector plate mounted behind the coil. Initially the electron beam passes straight through the coil and the full current is collected on the plate. However, when the magnetic field is pulsed, a magnetic field gradient is created around the coil with the maximum value in the coil centre, $B_{max}$. As the electron beam approaches the coil, there will be some minimum magnetic field $B_0$ where the

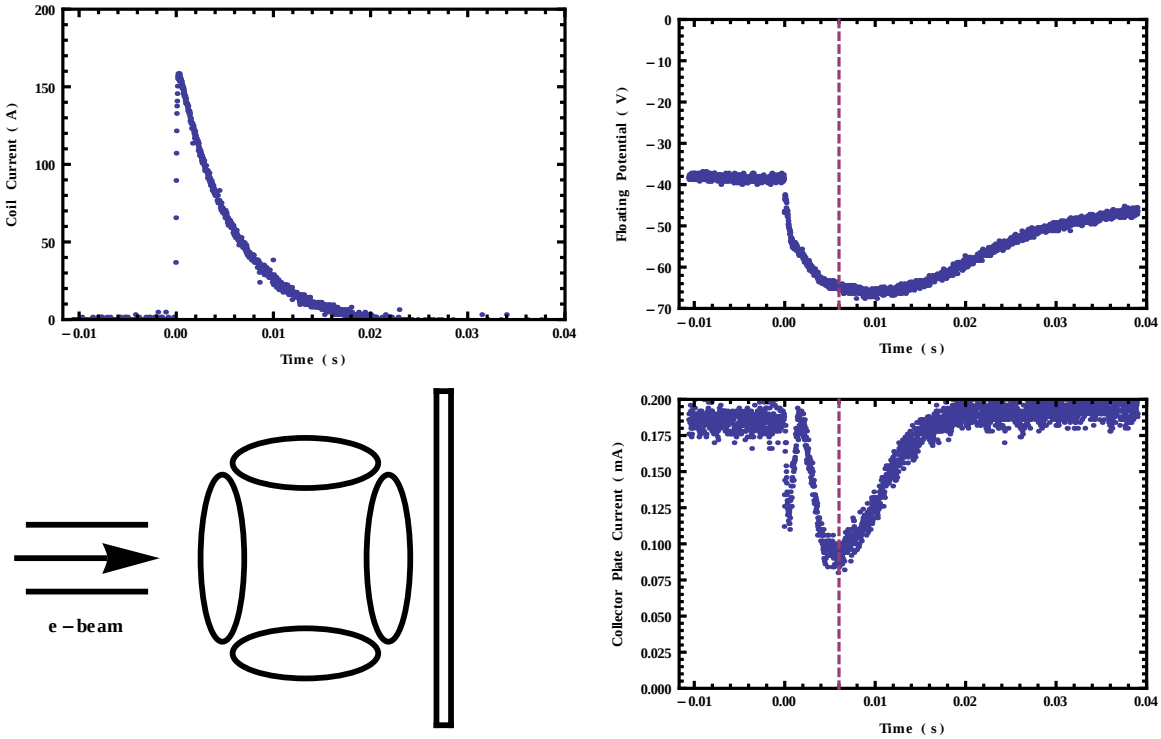


Figure 4.10: The collector plate was mounted behind the Polywells rear coil. A 10 keV electron beam with current $< 1$ mA was incident on the front coil face, aligned with the coil axis. The background gas pressure was 22 mTorr. As the coil current was pulsed a floating potential well was observed to form and simultaneously there was a decrease in the current collected by the rear plate. See text for details.

magnetic moment becomes adiabatic and thus a loss cone (or in this case an admittance angle) can be defined through Equation 4.2. The overall result is that a portion of the incident electron beam will undergo mirror reflection and will not be collected by the plate. Hence we expect to observe a decrease in the collected current when the magnetic field is pulsed.

The results of this experiment in Figure 4.9 show the expected behaviour has been observed. During the peak of the magnetic field pulse, the collected current has reduced to 25% of its initial value. During this experiment the peak magnetic field was $B_{max} = 0.138$ T. The primary electron beam energy was 10 keV with a current of <1 mA (below the resolution of the HV power supply current meter). These parameters give a minimum gyroradius in the coil centre of $\approx 2.5$ mm when the velocity vector of the electrons is perpendicular to the magnetic field. Consequently, it can be predicted, from these initial conditions, that a fraction of the incident beam population will undergo mirror reflection. These conclusions are in agreement with the experiment.

In the next experiment, the collector plate was alternately placed either behind the Polywell's rear coil or covering one of the side coils. The approximate mounting position of the two collector

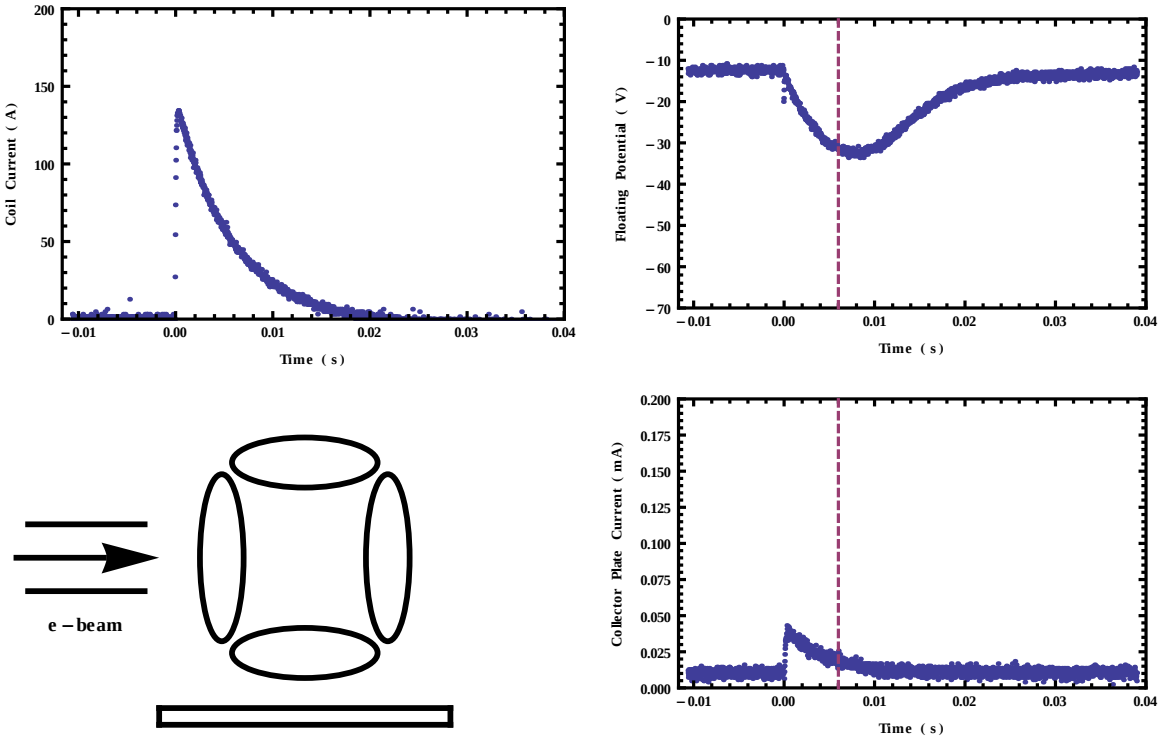


Figure 4.11: The collector plate was mounted on one of the side coils, indicated in Figure 3.8. A 10 keV electron beam with current $< 1$ mA was incident on the front coil face, aligned with the coil axis. The background gas pressure was 22 mTorr. As the coil current was pulsed a floating potential well was observed to form and simultaneously there was an increase in the current collected by the side collector plate. See text for details.

plate locations is shown in Figure 3.8. Two separate pulses have been analysed for evidence of the correct electron confinement behaviour.

The first pulse shown in Figure 4.10 is for the case of a collector plate mounted behind the rear Polywell coil. Just as in the case of a single coil, when there is no magnetic field the full beam current is collected on the rear plate. When the magnetic field is pulsed, there is a minimum in the floating potential and also a decrease in the current collected on the rear plate. Both of these observations are characteristic evidence for mirror confinement in the coil faces producing a build up in negative space charge.

However, this interpretation cannot be correct if we consider the primary electron beam energy and its relationship to mirror confinement. In this experiment, the coil current and magnetic field were set lower than in the previous experiment to a regime where the primary beam should be able to pass through the device without undergoing mirror reflection. In this example pulse, the coil current of $\approx 150$ A produced a peak magnetic field of $B_{max} = 0.024$ T which gives a minimum (best case) gyroradius of $r_g = 1.5$ cm. This implies that the average gyroradius is on the same length scale as the coil radius which is too large to satisfy the adiabaticity condition, Equation 1.4, and hence the primary electron beam would be unlikely to undergo any mirror reflection. Furthermore, because the beam is highly collimated and makes a shallow angle of incidence to the coils peak magnetic field ($\theta \approx 0$), the beam is unlikely to be deflected away from its axis.

Let us now consider the data for the side collector plate position shown in Figure 4.11. All other experimental parameters have been kept constant with the data of Figure 4.10. When no magnetic field is present we would expect the electron beam to pass straight through the device and no current would be collected by the plate. On the other hand, when the magnetic field is pulsed at a field strength high enough to produce mirror confinement, we expect the electron beam current to be redistributed equally around the coil faces. This would lead to a small current being measured on the side coil plate when the magnetic field was pulsed. As expected, the data in Figure 4.11 show that negligible current was drawn when there was no magnetic field. But during the current pulse a floating potential well was formed and there was a small increase in the current collected by the side plate. Qualitatively, one can say that this current approximately takes in to account the current not collected on the rear coil if we assume this current would be similar on all the other side faces.

The data from both collector plate positions suggests that a fraction of the electron beam was redistributed amongst the coil faces through ballistic collisions around the magnetic null. However, for this to occur there must be a secondary low energy component in the electron beam that has not yet been reported in studies characterising the cylindrical hollow cathode electron beam [22, 25, 38]. This conclusion is supported by the results of Section 4.3.

## 4.5 Summary

- The Teflon Polywell was our first prototype device aimed at obtaining at least qualitative validity of the Polywell concept in establishing a potential well. Floating potentials of up to –250 V were obtained for periods of several milliseconds, suggesting the formation of a virtual cathode stable on at least the millisecond time scale.

- It was shown that the virtual cathode does not form outside of a narrow range of coil currents in this design. A number of reasons for this behaviour have been explored including mirror reflection of the injected electron beam, and the concept of a secondary low energy electron population being produced by the hollow cathode. Ultimately it was not possible to precisely determine the cause of this behaviour.

- Potential well formation was shown to be extremely sensitive to the background gas pressure. It was concluded that increasing the background gas pressure results in increased ionisation which counteracts potential well formation. A balance must be found between increasing the background gas pressure for creating meaningful ion densities in the core and decreasing the background gas density for reducing the destructive effects of ionisation.

- A collector plate experiment was constructed to explore the redistribution of the electron beam current during Polywell operation. Data from both collector plates suggested that a fraction of the electron beam was redistributed amongst the coil faces through ballistic collisions around the magnetic null. However the magnetic field in that experiment should have been too low to produce mirror reflections.

- The experimental results of this chapter provided good qualitative evidence of potential well formation but motivated the need for a more precise diagnostic. Lessons learned from this set of experiments were employed in the design of the biased Langmuir probe covered in the next chapter.

Chapter 5

# Biased Probe Results and Analysis in WB6-mini

In this chapter orbital limited motion theory has been applied to two biased probes in a low beta Polywell. The cases studied include electron injection, magnetic field scaling, Polywell bias scaling, and radial position profiles. Langmuir's original orbital limited motion results for a monoenergetic electron beam are shown to be in excellent agreement for electron injection into the Polywell. A distribution function is proposed for the electron plasma characteristics in the centre of the magnetic null and confirmed with experimental results. A translational stage was used to measure the radial plasma potential profile. In other experiments two probes were used to simultaneously measure the profiles in both the null and a position halfway along a corner cusp. The results confirm a radial potential well created by electron trapping in the device. In addition, we present preliminary results of the potential well scaling with magnetic field $B$, Polywell bias voltage $V_{bias}$, and injection current $I_{beam}$.

## 5.1 Introduction and Motivation

A biased probe diagnostic enables a number of parameters to be measured that are crucial to a Polywell's performance. A single ended Langmuir probe provides a local measurement of the plasma potential at the probe position and hence can be used to directly map the spatial potential profile within the device. Characterising the potential well structure is crucial to any experimental study of the Polywell because the formation of a deep virtual cathode is integral to the operation of a Polywell [69]. In addition, a biased probe allows the determination of the Electron Energy Distribution Function (EEDF) and electron density, $n_e$. Understanding the EEDF is critical for measuring the relative energy components for monoenergetic (beam like) and thermal motion. In an ideal Polywell electrons would be monoenergetic to avoid large energy losses through energy upscattering. However in any real plasma system we expect thermalisation to occur, hence we also want to measure the temperature of the electrons, $T_e$. Rosenberg and Krall have theoretically proposed that the Polywell should be able to support a non-Maxwellian plasma on moderately long time scales [86]. Measuring the ratio of the monoenergetic and thermal components of the electron energy distribution enables the degree of thermalisation in the plasma to be determined and is important for determining whether a monoenergetic electron population can be sustained [86].

A biased cylindrical Langmuir probe can be used to measure all of these parameters but

is not usually applied to experiments with a high (keV) electron energy or with a magnetic field. At the high bias voltages required for measuring keV electrons the probe can create its own discharge corrupting the results. However the underlying confinement properties scale with magnetic field strength and energy, and thus can be studied with low energy electrons without fundamentally changing the physics.

In magnetic fields the analysis of biased probes can become extremely complicated and sometimes intractable. In general, there is no exact theory about the interpretation of the current versus voltage I(V) trace of a single ended Langmuir probe in a magnetic field. However, the Polywell has a magnetic null in the centre of the device which can be used to exactly characterise the electron parameters. The magnetic field varies with $r^3$ radially outwards from the null, and hence we can use a second probe to measure the gradual change in the I(V) traces, assuming the deviation due to the presence of the magnetic field is initially small. Eventually one expects the I(V) trace to slowly diverge from the theoretically expected curve, producing increasingly larger errors.

The only previous experiment to measure the plasma potential of the Polywell was performed by Krall using a capacitive probe [81, 109]. The capacitive technique is expected to be superior in larger fusion relevant Polywells where large electron energies and higher electron densities may make the single biased probe method unusable. However, when the physics is scaled down to a comparatively low electron energy and magnetic field regime the biased probe method is advantageous because of its measurement accuracy and scope of parameters measured.

The principle aim of this work is to apply two biased probes to measure the radial potential well profile as a function of other parameters such as magnetic field, injection current and injection energy. We will also present preliminary measurements of the way the potential well scales with the Polywell bias voltage and magnetic field strength. Furthermore, we will comment on the relationships between other parameters measured such as the electron density, mean energy and thermal energy component.

## 5.2 Experimental Setup

Most of the details for the WB6-mini experiment were described in Section 3.2, therefore only a few key elements of the experiment will be highlight here. Figure 5.1 shows the key biased probe mounting positions. The cylindrical Langmuir probes were constructed from tungsten wire with a radius $r_p = 50$ $\mu$m and mounted into ceramic tubing with a 0.8 mm outer diameter. The part of the tungsten wire that extends into the plasma is the probe length, $l_p = 5$ mm. Probe A was mounted onto a translation stage with a total travel distance of 5.5 cm and moved in 3 mm increments. It was positioned along a coil axis so that the extremities of translation are the geometric centre of the Polywell and a location just outside the Polywell coils. Probe A was at an angle of 8° to the coil axis so that it did not block the filament that was the source of electrons to this face of the Polywell. An additional reason for having a small angle is so that the probe crosses more magnetic field lines. Electron transport along magnetic field lines is much

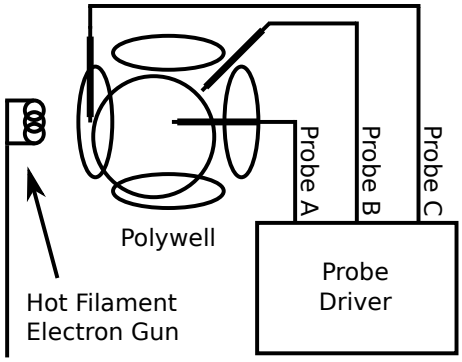


Figure 5.1: A diagram of the experimental setup showing the key biased probe positions.

faster than cross field transport. This is expected to accelerate space potential build up across field lines and would result in a larger potential difference than would occur along a point cusp. Probe B is permanently mounted in alignment with a corner cusp and located halfway along the Polywell radius. All probes were driven from the biased probe driver discussed in Section 3.3.

## 5.3 Orbital Limited Motion Langmuir Probe Theory

The most appropriate type of theory to use is an orbital limited motion theory which was originally described by Langmuir and Mott-Smith [104]. Based on the emission current of our filaments, we expect to observe densities between $10^8$-$10^9$ cm$^{-3}$ at energies that give us debye lengths ranging from 2 cm down to 1 mm. Hence it is assumed that the device radius $R_{device} > \lambda_d \gg r_p$ at all times. In the low density limits we expect to have inaccuracies when the $\lambda_d$ is almost as large as the device. However, even before this limit is reached, the characteristic curve will start to deviate from the theory as $\lambda_d \approx l_p$ and the infinite cylinder approximation is no longer applicable. It was assumed that the sheath around a probe has a sharp edge boundary. The potential at this boundary was considered to be the plasma potential.

We also assumed that the electron plasma is collisionless such that the electron motion in the sheath around the probe can be described by free orbits. Because $r_p \ll l_p$ we can assume the sheath is cylindrically symmetric and probe end effects can be ignored. Consequently, the conditions that determine whether an electron will reach the collector for a given voltage depend only on the space potential and initial electron velocity at the sheath edge. Therefore the total I(V) curve for electron current collected at the probe is determined by summing the contributions from the electron distribution function with the appropriate initial conditions. The resulting equation is only a function of the potential across the sheath and the sheath radius. For the calculation to be exact it is also necessary to solve Poisson's equation for the space charge in the sheath. This approach has been carried out on a number of occasions [97] however we will assume that the problem is independent of sheath size and focus on orbital limited motion.

In cylindrical symmetry the current is calculated in a 2D plane intersecting the probe, giving current per unit probe length, $I/l$. The velocity co-ordinates $u$ and $v$ are defined as the radial

and tangential velocity components, respectively, of an electron arriving at the probe sheath. The velocity distribution function, $f(u, v)$ is normalised such that

$$n_e f(u, v) du dv, \tag{5.1}$$

gives the number of electrons per unit volume with velocity components in $du$ and $dv$. Therefore, the number of electrons in unit time that arrive at the sheath edge with velocities in $du$ and $dv$ are

$$2\pi a n_e u f(u, v) du dv, \tag{5.2}$$

where $a$ is the sheath radius and $n_e$ is the electron density. In its current form, this equation is challenging to use because the sheath radius is an unknown. However, Langmuir has shown [104] that in the limit of an infinite sheath, equation 5.2 approaches a limiting form. By taking the limit of a large sheath in equation 5.2, multiplying by the charge $q$, length $l_p$, and integrating over the limits of velocity for electrons that can reach the probe, Langmuir obtained the general form for the current collected by a cylindrical probe [104].

$$I(V) = 4\pi r_p l_p n_e q \int_{0,v_0}^{\infty} u \sqrt{u^2 + \frac{2q(V - V_p)}{m_e}} f(u, 0) du. \tag{5.3}$$

Here $V$ is the probe bias voltage. The lower boundary of velocity integration is split based on whether the probe is attractive or repulsive with respect to the local plasma potential, $V_p$. When the probe is attractive, $V > V_p$, the lower bound is 0 since all electrons have enough energy to potentially reach the probe surface. However, when the probe is negatively biased, $V < V_p$, electrons must have at least some critical minimum energy in order to overcome the repulsive field from the probe and reach the probe surface. This critical minimum energy is determined by the voltage difference between the probe and the plasma, and can be expressed as a minimum velocity $v_0$, where

$$v_0 = \sqrt{\frac{2q(V - V_p)}{m_e}}. \tag{5.4}$$

This equation was used by Langmuir and Mott-Smith [104] to derive the ubiquitous Maxwellian $I_m(V)$ characteristic as well as the $I_b(V)$ for a one dimensional beam. However, these results are only applicable in plasmas with the appropriate distribution functions and become meaningless in plasmas where extra complicating factors such as a magnetic field can significantly alter the EEDF. To make the process of analysing the probe data tractable it is important to build up information about the EEDF at each phase of progressively more complex plasma conditions.

In the case of the Polywell this means at first understanding and confirming the characteristics of the electrons being injected into the Polywell. This information can be used to approximate the EEDF in the centre of the well when a relatively weak magnetic field is applied. And finally we can build on these results to make measurements of electrons in a moderate magnetic field. At each stage the base $I(V)$ equation (5.3) for the biased probe response can

be directly modified for the specific plasma conditions anticipated. As long as the expected distribution function is known we can integrate this function numerically and compare it with the data, and use it to fit plasma parameters to the measured $I(V)$ data.

## 5.4 Analysis of Electron Injection

The electron source (the heated filament) was at ground potential. Electrons were extracted and accelerated by the electrostatic potential placed on the metal casing of the Polywell field coils, thus accelerating the electrons in a direction that is normal to the plane of the coils. As a result, the energy distribution function of the electron beam was expected to be monoenergetic. However, one can also expect some spreading in this energy distribution due to interactions of the electrons with the local space charge established by the beam.

We have assumed that the magnetic field lines at the centre plane of a coil, and therefore approximately parallel to the direction of motion of the beam, would not change the energy distribution greatly. As a result, we approximated the electron distribution function as that given by Langmuir [104] for a beam of electrons with a Maxwellian energy component given by

$$f_b(u, v, \theta) = \frac{m_e}{2\pi kT} \exp\{-\frac{m_e}{2kT}(u^2 + v^2 + u_d^2 - 2u_d(u\cos\theta + v\sin\theta))\}, \tag{5.5}$$

where $u_d$ is the drift velocity of the beam. The coordinate $\theta$ is the angle between the beam axis along $u_d$ and the radial velocity coordinate, $u$, with respect to the sheath. In the limit of a large sheath, the sheath can be approximated as being circular. Hence the probe current is found by using $f_b(u, v, \theta)$ in Equation 5.3 and integrating around the sheath circumference,

$$I_b(V) = 2\pi r_p l_p n_e q \int_0^{2\pi} \int_{0,v_0}^{\infty} u\sqrt{u^2 + \frac{2q(V - V_p)}{m_e}} f_b(u, 0, \theta) du d\theta. \tag{5.6}$$

When the probe is at the plasma potential $V_p$, the collected probe current can be approximated as

$$I_0 = \frac{1}{4} A_p n_e q \bar{c} \tag{5.7}$$

where $A_p$ is the probe surface area and $\bar{c}$ is the mean speed of the electron distribution [106]. In the case of the beam distribution $f_b$, $\bar{c} = u_d$.

Equation 5.6 cannot be evaluated analytically. Heatley [100] has found an exact series solution but it converges very slowly when the drift velocity is large compared with the thermal velocity. Since this scenario is expected in our situation, we have obtained solutions through numerical evaluation of equation 5.6.

The measured I(V) data was filtered using a moving window average combined with a Svatsky and Golay filter [103, 107]. The data was fitted using the standard non-linear fitting tools available in Mathematica. The only constraint applied to the fitted model was that $V_p < V_{bias}$, since it is not possible for the plasma potential $V_p$ to be more positive than the Polywell bias potential $V_{bias}$ in an electron only plasma.

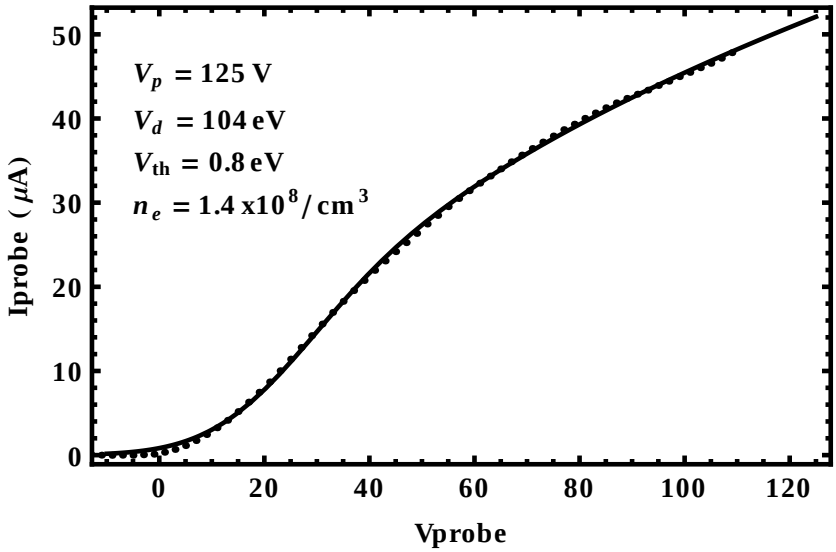


Figure 5.2: A sample $I(V)$ curve fitted with the predicted function for a drifting-Maxwellian. In this experiment the probe was placed in the centre of the coil nearest to the single filament being tested. No magnetic field was present for the test. The Polywell was biased to a voltage of 150 V drawing a current of 4.5 mA.

A sample fit is shown with the fitted parameters in Figure 5.2. All fit parameters are reported in their voltage equivalent energies to make for easy comparisons with other experimental parameters. If electrons are accelerated from ground through to $V_p$ then they are expected to have a monoenergetic drift energy, $V_d$, close to but less than $V_p$, which is observed. Since the electron density and beam transit times are small, such that the electron collision frequency is negligible, we also expect the thermal energy component, $V_{th}$, to be much less than the drift energy. The fitted parameters are in the order $V_{bias} > V_p > V_d \gg V_{th}$, and support the hypothesis that this experimental setup results in a beam of monoenergetic electrons with a very small thermal energy.

A further justification for the use of the drift Maxwellian distribution over the most commonly occurring normal Maxwellian distribution, $f_m$, is now given by examining the differences between both $I(V)$ characteristics. The characteristic $I(V)$ for $f_m$, $I_m(V)$, consists of two regions, one on either side of the plasma potential. The $I_m(V)$ is $\propto e^V$ when the probe is repulsive, and $\propto \sqrt{V}$ when attractive. The plasma potential can then be found by plotting the double derivative, $d^2I/dV^2$, and finding the zero crossing point which is equal to $V_p$. This is because the two halves of the $I_m(V)$ around $V_p$ have opposite curvature. By following this standard procedure we can show that our data differs substantially from the normal Maxwellian characteristic, $I_m(V)$, and hence a poor fit was obtained. Figure 5.3 shows an example data set where using the $d^2I/dV^2 = 0$ method gives $V_p = 23$ V. There was a significant deviation in the fit residuals around $V_p$. This procedure proved that the standard Maxwellian distribution is not suitable, but does not prove that the drifting Maxwellian is the best choice.

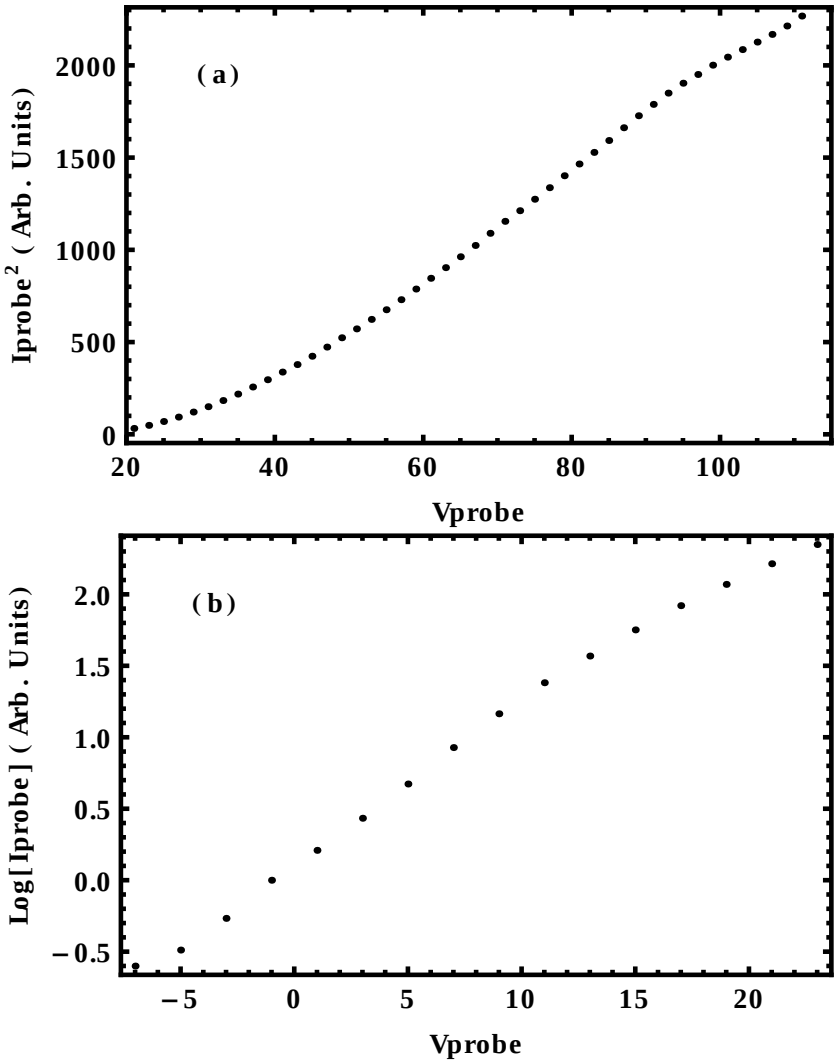


Figure 5.3: If a Maxwellian probe response $I_m(V)$ is assumed, $I_{probe}$ should be $\propto \sqrt{V}$ for voltages $V_{probe} > V_p$. $V_p$ would be given by the location of the crossing point for the double derivative which in the case of this experiment gives $V_p = 23$ V. The data is plotted as a function of $I^2_{probe}$ in plot (a) for $V_{probe} > 23$ V and would be linear if a Maxwellian velocity distribution was appropriate. Similarly, the case for $Log(I_{probe})$ is plotted in (b) for $V_{probe} < 23$ V and would be linear if a simple Maxwellian was present. There was a significant deviation in the fit residuals for $I_m(V)$ around $V_p$ suggesting a Maxwellian distribution is not appropriate for this plasma.

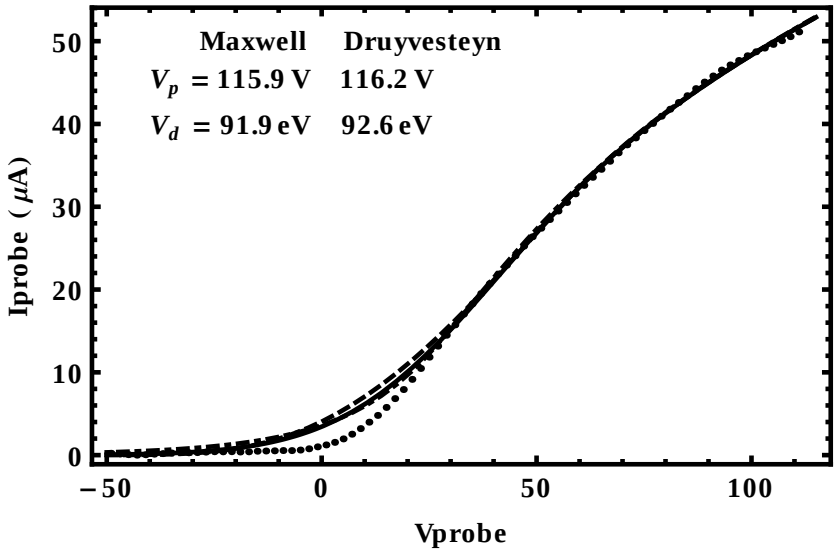


Figure 5.4: A comparison of fits to the data with the drifting Maxwellian (solid line) and Druyvesteyn (dashed line) distributions. Both functions gave the same $V_p$ and $V_d$ to within $\sim 1$ V, suggesting that the high $V_d/V_{th}$ makes it difficult to distinguish between the two distributions.

The data has also been fitted with a drifting Druyvesteyn distribution. However, since the Druyvesteyn distribution only produces a significant change in the thermal component $V_{th}$ of the distribution and $V_d/V_{th} \gg 1$ is expected in our experiment, we would expect there to be very little change in the overall fit quality between the two distributions. Figure 5.4 compares the two fitted functions on an example dataset. Both functions gave the same $V_p$ and $V_d$ to within $\sim 1$ V, confirming that the high $V_d/V_{th}$ makes it difficult to distinguish between the two distributions. Hence we will assume that the comparatively simpler drifting Maxwellian is the most appropriate approximation to the injected electron EEDF.

Because of the complex geometry of the experiment these distributions are likely to be an oversimplification and other distributions could arise. For the cases where the extraction voltage was low, an appropriate fit to either distribution could not be obtained. Consequently, one must assume there might be another more appropriate distribution. Consider that at lower extraction voltages space charge effects can significantly alter the distribution shape. A 1D vacuum diode approximation to this geometry suggests space charge effects may occur in the lower extraction voltage range of this experiment.

## 5.5 With B and Without B Test Cases

By building on the information learned about the EEDF of extracted electrons in the previous section, we can now begin to analyse how a biased probe will respond when placed in the magnetic null at the centre of the device. When the magnetic field is turned off, $B_{peak} = 0$, we can use the same drifting Maxwellian as that given in Eqn. 5.6. However, when the magnetic field is turned on, one needs to take into account the effects of the magnetic field structure on the EEDF in the null. As discussed in Chapter 2, the magnetic null region causes an electron beam to become defocused and undergo ballistic collisions around the adiabatic flux surface. This ballistic scattering effect leads to an electron energy distribution that is isotropic and predominantly monoenergetic with a narrow spread of electron energies due to thermalisation. These assumptions are expected to be valid only in the absence of space charge effects for a low density electron plasma, which were the experimental conditions reported in this chapter. The resulting distribution could be described as a Maxwellian with an isotropic mean offset energy, $V_\mu$. The distribution we propose is

$$f_\mu(v_r) = e^{-\frac{m(v_r - v_\mu)^2}{2\sigma^2}} \tag{5.8}$$

where $v_r$ is the velocity component along the radial coordinate in spherical coordinates, $v_\mu$ is the velocity equivalent to the offset energy $V_\mu$, $\sigma$ is the standard deviation of the velocities and is related to the thermal energy $V_{th}$, through $\sigma^2 = qV_{th} = kT_e$. Here it is possible to define an electron temperature $T_e$ although it is not strictly true in the conventional sense. This distribution function is isotropic because there is no dependence on the angular velocity coordinates $v_\theta$ or $v_\phi$. A plot of $f_\mu(v_r)$ is given in Fig. 5.5.

Two limits are imposed on the proposed velocity distribution as a check to its validity. First, in the limit of no mean speed $v_\mu$ we expect a relaxation to a Maxwellian velocity distribution. This can be seen by converting back to Cartesian velocity components.

$$\lim_{v_\mu \to 0} e^{-(\frac{\sqrt{v_x^2+v_y^2+v_z^2}-v_\mu}{\sigma})^2} = e^{-\frac{v_x^2+v_y^2+v_z^2}{\sigma^2}} = f_m \tag{5.9}$$

Second, the distribution approaches an infinitesimally thin velocity surface as the width of the thermal component approaches zero, $\sigma \to 0$. This describes an isotropic monoenergetic distribution.

$$\lim_{\sigma \to 0} e^{-(\frac{\sqrt{v_x^2+v_y^2+v_z^2}-v_\mu}{\sigma})^2} = \begin{cases} 1, & \text{if } \sqrt{v_x^2+v_y^2+v_z^2} = v_\mu^2 \\ 0, & \text{if } \sqrt{v_x^2+v_y^2+v_z^2} \neq v_\mu^2 \end{cases} \tag{5.10}$$

The equation for the probe current is expressed in terms of the velocity components in the 2D plane intercepting the probe, and hence the distribution becomes

$$f(v_x, v_y) = \int_{-\infty}^{\infty} e^{-(\frac{\sqrt{v_x^2+v_y^2+v_z^2}-v_\mu}{\sigma})^2} dv_z. \tag{5.11}$$

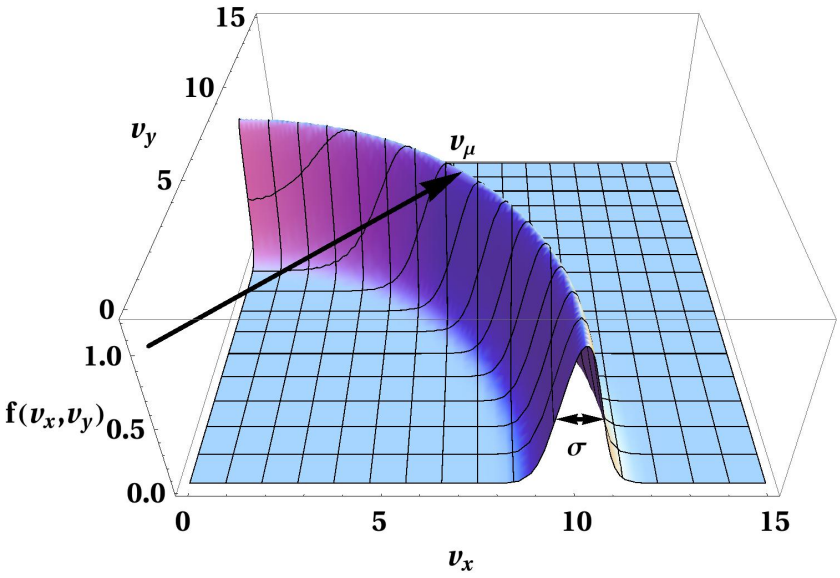


Figure 5.5: A plot of the mean energy isotropic distribution $f_\mu(v_r)$ in one quadrant of a 2D Cartesian plane. When $\sigma \to 0$ this plot becomes a slice through a sphere. In this plot, the function $f_\mu(v_r)$ has not yet been normalised, such that integration over all $\mathbf{v}$ yields 1. Note that this plot is a slice in a Cartesian plane, and distinctly different from the projection of $f_\mu(v_r)$ onto the 2D plane at right angles to the probe, which is plotted in Fig. 5.6.

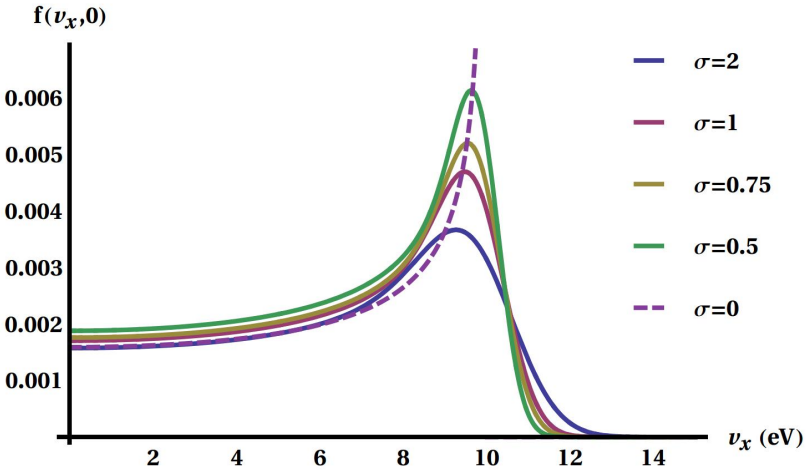


Figure 5.6: Convergence of Eqn. 5.11 $f(v_x, 0)$ on the monoenergetic isotropic distribution. The case shown has $v_\mu = 10eV$. As $\sigma \to 0$ the result converges on $1/\cos\phi$ which is the analytical result for the monoenergetic isotropic case[104]. See Appendix A.1 for this derivation.

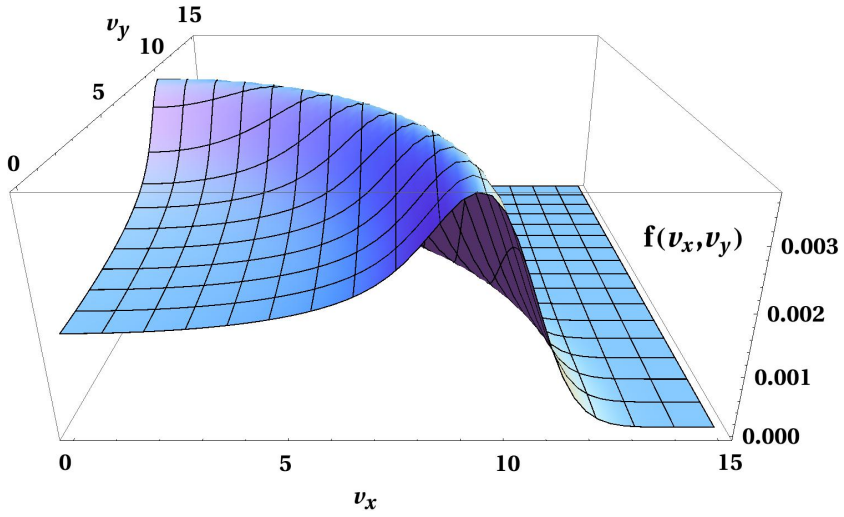


Figure 5.7: A plot of the resulting probability density function $f(v_x, v_y)$ in Equation 5.11.

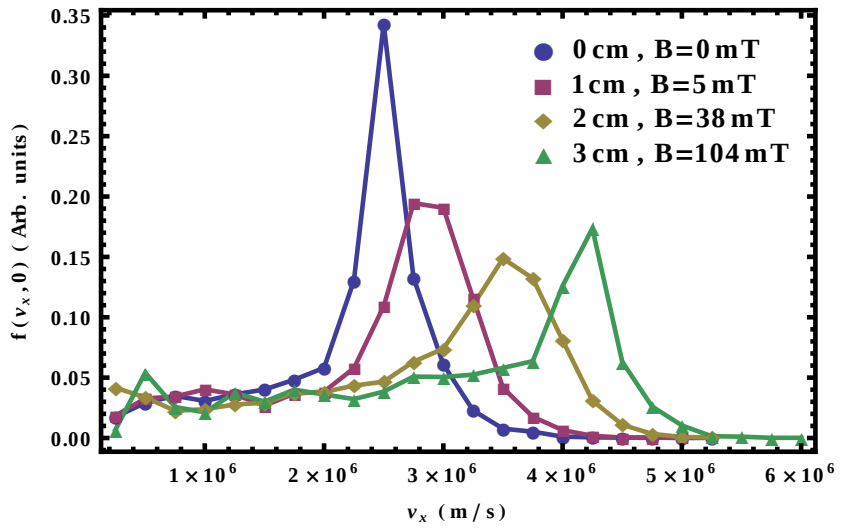


Figure 5.8: A plot of the velocity distribution $f(v_x, 0)$ from simulated data. The commercial OOPIC code was used to simulate an electron plasma with conditions approximating our experiment. The particle data was sampled in a number of spatial locations along the coil face axis. This plot shows reasonable agreement with the predicted function shown in Fig. 5.6 and thus supports the theoretically proposed $I_\mu(V)$.

| Dataset | $B = 0$ | $B = 15$mT | |
|---|---|---|---|
| Model | Beam | Iso. | Beam |
| $V_p$ | 87.2 V | 22.9 V | 56.1 V |
| $V_d$, $V_\mu$ | 65.5 eV | 23.7 eV | 49.7 eV |
| $V_{th}$ | 1.3 eV | 1.1 eV | 0.72 eV |
| $n_e$ | $1.7 \times 10^8$ cm$^{-3}$ | $1.4 \times 10^8$ cm$^{-3}$ | $1.7 \times 10^8$ cm$^{-3}$ |

Table 5.1: Fitted parameters for the two data sets shown in Figure 5.9. For the case of $B = 15$ mT, fits to both models have been listed. The mean energies, $V_d$ or $V_\mu$, are given depending on the model fitted.

A slice of $f(v_x, v_y)$ is shown in Fig. 5.6 revealing its dependence on $v_\mu$ and illustrating its convergence on the monoenergetic isotropic distribution in the limit as $\sigma \to 0$.

Further support for the use of the proposed isotropic mean energy distribution $f_\mu$ has been given by 2D PIC code simulations using the commercially available OOPIC code [2, 17]. The simulated dimensions and parameters were designed to approximately reproduce the experimental conditions explored in this paper. The simulation geometry was in a 2D slice through the centre of the device, intersecting four of the six Polywell coils. The simulated Polywell had a coil current of 7950 Amp turns, giving a peak field in the coil face of $B_{peak} = 0.14$ T. Four simulated electron sources surrounded the coils, each emitting a current of 0.2 mA/cm (note this is expressed as a current per unit of height because the simulation is 2D). The extraction voltage was set to $V_{bias} = 130$ V, and the resulting potential well formed by the electrons is 35 V deep. The velocity components of the simulated particles have been extracted at four spatial positions along the coil axis, extending from the centre of the null to the field coil. The extracted velocity data has been used to create a plot of the projected 2D velocity distribution function, $f(v_x, v_y)$. A 1D slice of that function is plotted in Fig. 5.8 and shows reasonable agreement with our proposed function, plotted in Fig. 5.6. Further discussion and analysis of the simulation results are left for further work, and is only presented here to support the proposed distribution function.

Substituting Eqn. 5.11 into Eqn. 5.3 gives the $I(V)$ characteristic for the isotropic mean energy distribution, $I_\mu(V)$. Two data sets are compared with their respective fits in Figure 5.9. In both cases the data has been collected from a single Langmuir probe located in the centre of the device. The Polywell bias voltage was held constant at $V_{Bias} \simeq 112$ V, extracting a current of $I_{Beam} \simeq 2.7$ mA. The coil current $I_{Poly}$ was varied to contrast the $B_{peak} = 0$ T case (no field in the coil face) with $B_{peak} = 15$ mT. At electron energies in the range of 20 eV to 100 eV, a magnetic field of 15 mT is sufficient to force the electron gyroradius to approach 10% of the device radius, $r_g < 10\% R_D$, which is the approximate condition for reflection from the adiabatic flux surface at the magnetic null boundary [74]. Hence $B$ is sufficiently large to prolong the electron confinement in the core.

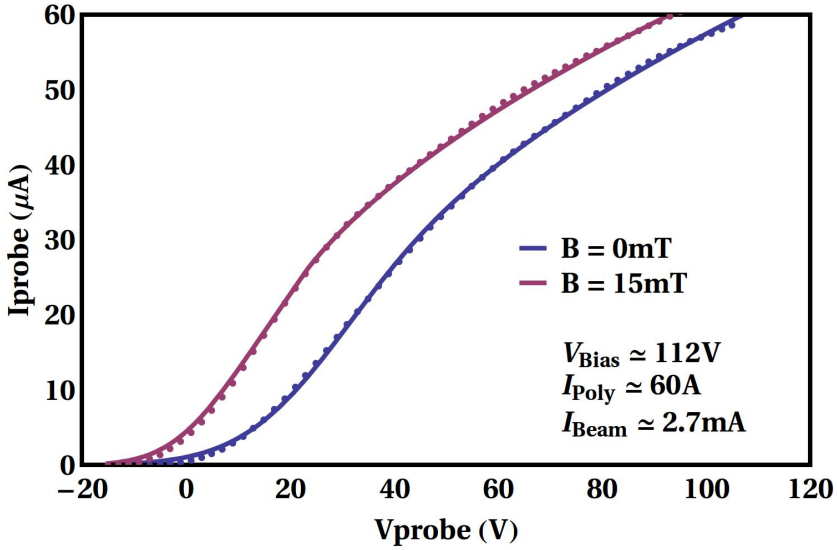


Figure 5.9: The two magnetic field test cases, both measured on Probe A in the centre of the device. The fitted parameters for the two data sets with their respective $I(V)$ characteristic models are given in Table 5.1.

Note that an equally good qualitative fit to the data can be made with the drifting/beam Maxwellian distribution, giving only negligible difference in the fit residuals (not plotted for clarity). Both distributions can be made to fit the data but give different plasma parameters in Table 5.1. The reason for this similarity in the underlying $I(V)$ functions is that Langmuir probes only measure relative energy, not potential. As a result, a Langmuir probe can be considered as a particle energy filter. Although it can be shown that a Maxwellian fit is not appropriate to either of these data sets, it might be impossible to conclusively prove which distribution is correct without resorting to an extra diagnostic that can provide additional information [101]. However, due to the magnitude of the applied magnetic field, ballistic reflections are likely to occur and will effectively make the beam distribution isotropic, and hence Eqn. 5.11 should be the most appropriate distribution of the two discussed. The results of the OOPIC simulation in Fig. 5.8 support this hypothesis.

It is worth noting that regardless of which of the two distributions is applied, the plasma potential $V_p$ has decreased relative to the $B = 0$ case. This is consistent with an increase in potential well depth, relative to the potential on the coils, due to an increase in the dwell time of the electrons in the presence of a magnetic field. However, the measured electron densities for the two cases were not significantly different, which would appear to contradict a claim of potential well formation. A possible explanation for this is that the application of the magnetic field causes the unidirectional beam to spread out isotropically to a larger volume within the device, which would cause a decrease in density. However, an increase in the electron dwell time within the device will lead to a higher electron recirculating current, thus increasing the density. Although the increase in this density is similar or equal to the density of the initial electron

beam, a deeper potential well will result since the electrons occupy a larger volume.

If a potential well has formed then $V_\mu$ must drop to conserve energy as the electrons transit into the well centre. However, if the magnetic field has increased the electron confinement time, then the increased electron density superimposes a space charge onto the vacuum potential field such that the electrons may no longer be accelerated to the same energy as in the $B = 0$ case. The thermal component, $V_{th}$, of the energy distribution remains unchanged, which is expected for the low magnetic fields used in this experiment. However, larger magnetic fields should result in an increase in confinement time leading to more thermalisation.

## 5.6 Radial plasma potential profile in a strong magnetic field

High magnetic fields in the planes of the coils and corner cusps are required to produce sufficient electron confinement in order to establish a virtual cathode in the core of the device. It has been shown [74] there is a non-adiabatic core in the central null region surrounded by adiabatic mirror confinement. Increasing the current in the coils should produce a larger confinement time for electrons within the device. However, this will also result in adiabatic mirror reflections on the outside of the device, thus limiting the injected electron current. Moreover, increasing the coil current further to create large confining fields will result in a reduction in volume of the non-adiabatic core region, which ultimately leads to a smaller confinement volume. This might lead to a smaller volume for fusion reactions when ions are introduced into the device, thus limiting the device efficiency.

In the experiment reported here, the electron injection parameters and coil currents were kept constant so that the effects of varying electron confinement time, volume and admittance do not produce additional confounding effects to the probe results. The probe located at the centre of the device, Probe A, was mounted on a translation stage that could move radially in increments of 3 mm. At each spatial point the experiment was repeated under the same initial conditions, allowing a measurement of the spatial change in the $I(V)$ characteristic across the device radius. All probe traces were analysed with the isotropic mean energy distribution. Some sample probe traces at four different spatial points are shown in Figure 5.10.

In the discussion of the previous section, the isotropic mean energy characteristic, $I_\mu(V)$, was shown to accurately represent the underlying EEDF in the null region. As the probe moves into higher $B$ field regions, we expect to see a growing disparity between the predicted $I(V)$ and the measured data in the attractive saturation current region. This is because the magnetic field limits electron transport across magnetic field lines to the probe, and hence limits the attainable saturation current. The result is an asymmetric sheath around the probe which significantly complicates the $I(V)$ characteristic calculation.

This deviation becomes progressively larger as the B field increases and the electron gyroradius $r_g$ approaches the probe radius. The parameters in this experiment have been chosen to minimise this effect over a large spatial range of the device. For the radial positions ranging from 0 cm to 2 cm, the gyroradius is expected to be at least ten times larger than the probe radius, $r_g \geq 10r_p$, and approaches $3r_p$ in the limit of the maximum magnetic field in the coil face. This means that over a wide range of measurement points, the gyroradius $r_g \gtrsim \lambda_d$ and hence the deviation from the prediction is expected to be minimal. A sample of the typical deviation in the saturation region is shown in Figure 5.11. The deviation in the saturation region was excluded from the curve fitting procedure. In figure 5.11 the fitting algorithm was restricted to the data range of -10 V to +60 V.

Although we would expect the magnetic field to alter the distribution function measured with the probe, we anticipate that when $r_g > r_p$ the magnetic field acts to locally randomise the incoming electron trajectories at the probe sheath, and acts to maintain the mean energy isotropic distribution observed in the magnetic null. This hypothesis is supported by the OOPIC

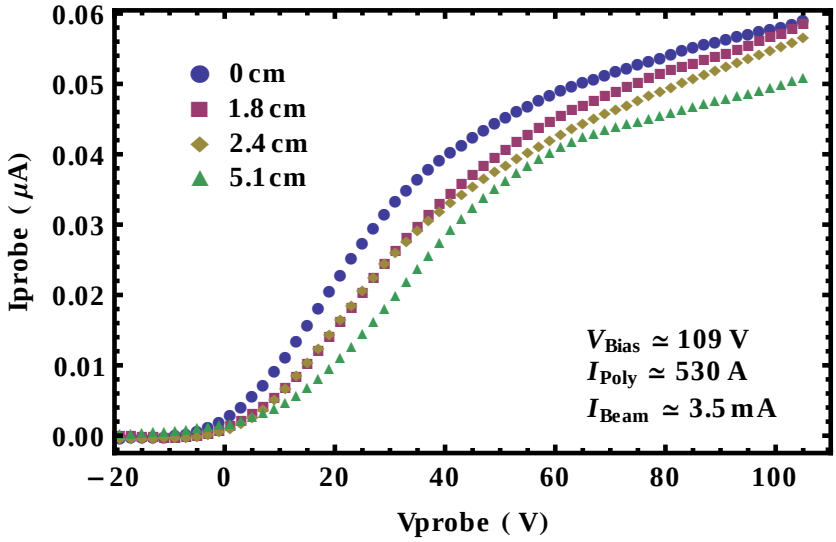


Figure 5.10: Four example $I(V)$ datasets from the high magnetic field radial profile experiment. Each dataset has been taken at a different spatial location along the coil axis.

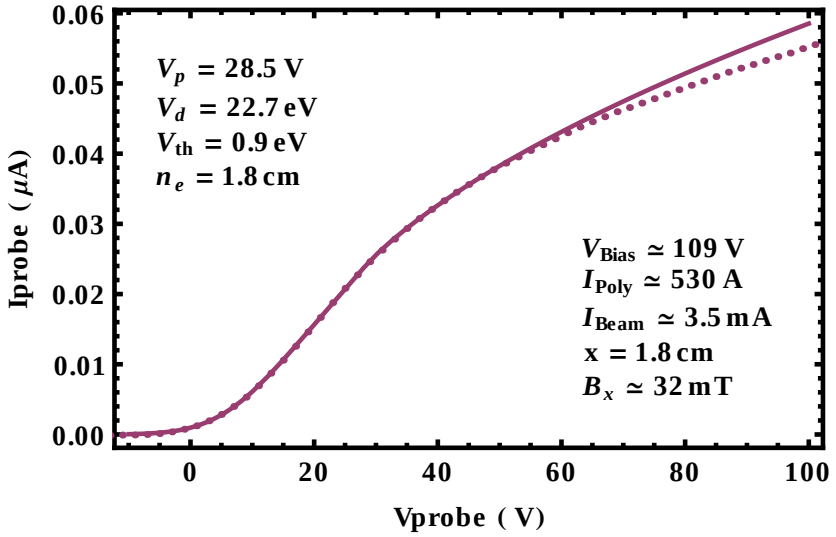


Figure 5.11: Sample of the fitting in a strong magnetic field. Shows the deviation from the fitted $I(V)$ in the saturation region.

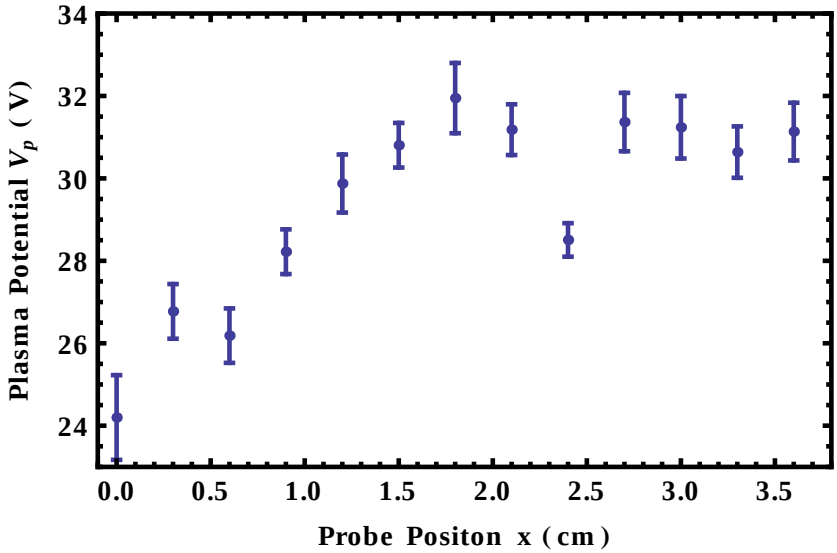


Figure 5.12: The spatial profile of the plasma potential in a strong magnetic field. The $I(V)$ characteristic at each spatial point has been fitted with the $I_\mu(V)$ to find the $V_p$ spatial profile. This data shows a potential well has formed in the middle of the device.

case study presented in Fig. 5.8, where the velocity distribution within the point cusp is similar to the predicted distribution presented in Fig. 5.6. Hence, we have used the mean energy isotropic $I_\mu(V)$ for data fitting for magnetic fields that range from the magnetic null at the device centre to the maximum field, $B_peak$, in the plane of the coils. It was assumed that any fitting errors become progressively larger as $B_{peak}$ was approached.

The resulting data for the radial plasma potential profile is shown in Fig. 5.12. The error bars were calculated from the error in the fit residuals during the fitting process. Note that there is a potential well (also known as a virtual cathode [19, 23]) of -10 V with a 2 cm radius from the centre. The fitting procedure is accurate over this region since the magnetic field is relatively low and the effects of the magnetic field on the distribution function are well characterised. However, there is more uncertainty about the values of the plasma potential in the 2 - 3.5 cm region, due to the higher magnetic fields, and are likely to represent an underestimate of the potentials.

The potential well formed can be compared with an analytical estimate from Poisson's equation if we assume that the well is approximately spherically symmetric and the electron density is approximately constant as a function of radius. In spherical coordinates Poisson's equation is

$$\frac{1}{r^2}\frac{\partial}{\partial r}\left(r^2\frac{\partial}{\partial r}V\right) = -\frac{n_e q}{\epsilon_0}. \tag{5.12}$$

Under the stated conditions we set the boundary condition $\partial V/\partial r = 0$ at $r = 0$. Moreover, we set $V = 0$ at radius $r = R$. Using both of these boundary conditions equation 5.12 can be solved to yield a relationship for $V_{well}$. The complete derivation is giving in Appendix A.2.

$$V_{well} = -\frac{n_e q R^2}{6\epsilon_0}. \tag{5.13}$$

Using the approximate density $n_e = 10^8$ cm$^{-3}$ and radius $R = 0.01$ m, we obtain $V_{well} = -30$ V. This deviation from the measured value is a result of the simplified assumptions stated above. A more accurate calculation of the potential well will need to take into account the real spatial density profile of the electrons. Also, the shape of the potential well does not agree with the simple parabolic shape predicted by Poisson's equation and the previously measured well by Krall [81]. This may be because the experimental device was too small to accurately measure the spatial variation of the plasma potential without averaging the spatial features over the probe length scale.

## 5.7 Scaling with B and E

To allow the measurement of the potential well variation with changes in magnetic field $B$, electric field bias $V_{bias}$, and electron density $n_e$, two probes were used to simultaneously measure $V_p$ at different radial points. Probe A was mounted at the centre of the device, and the other, Probe B, at a radial position of 1.8 cm, which was approximately halfway along the device radius. In the first experiment, the magnetic field was varied such that the peak magnetic field in the coil face varies from $B_{peak} = 0$ to $B_{peak} = 26$ mT. The measured plasma potential from the two probes as a function of the maximum magnetic field is given in Fig. 5.13. When the magnetic field is relatively weak, the potential difference between the probes indicates that no potential well is present, because the $V_p$ at the centre probe is more positive than at Probe B. When the magnetic field reaches some crucial minimum value, 5.5 mT in this experiment, the potential difference between the two probes is inverted and a potential well begins to form and is clearly measurable. Moreover, the potential difference between the two probes becomes progressively larger with increasing magnetic field.

There are significant challenges in designing an experiment that can be used to accurately characterise the way the potential well scales with B because the size of the adiabatic flux surface becomes progressively smaller with increasing B. Hence, the position of Probe B would have to be adjusted for each data point to compensate for the change in well size. If we can assume that the difference between the two probes is indicative of the overall change in the potential well depth we can obtain a relationship for the scaling of potential well with B. The analysis has been restricted to data in the domain of $> 15$ mT because it is unclear if a potential well has formed for fields at lesser magnitudes. A plot of the potential difference between the two probes is shown in Fig. 5.14 and scales approximately linearly with magnetic field $B$. However, a greater measurement range would be needed to confirm this relationship, and also a more detailed study is required to determine how best to characterise the change in well depth with $B$.

In another experiment the magnetic field was held constant at $B_{max} \simeq 0.16$ T while the Polywell bias voltage was varied from $V_{bias} = 93$ V to 122 V, the data is shown in Fig. 5.16.

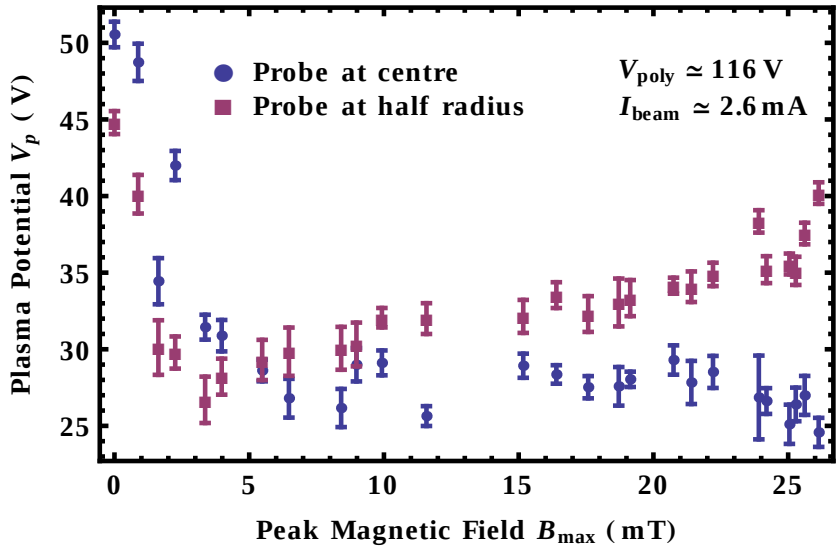


Figure 5.13: Potential well formation in the low magnetic field range. The plasma potential $V_p$ for Probes A and B is shown over a range of relatively low peak magnetic field values. As the field increases, the potential difference between the probes eventually becomes inverted and becomes progressively larger with increasing magnetic field strength.

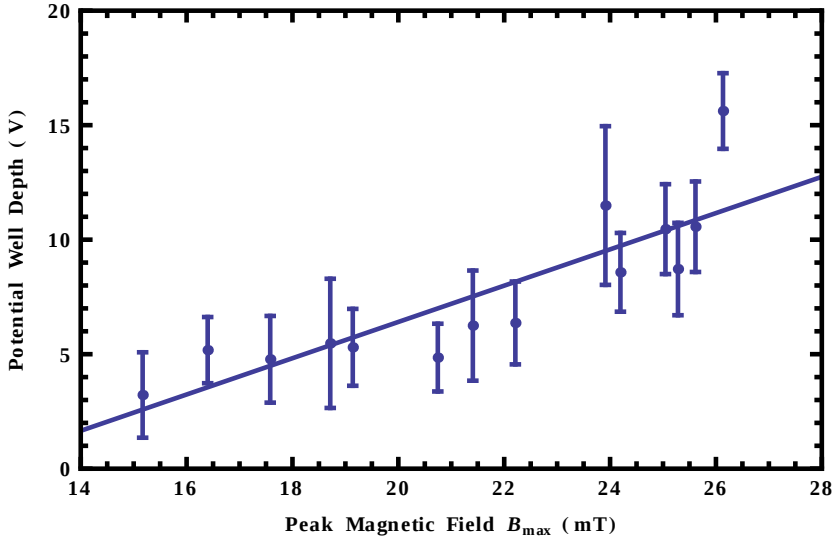


Figure 5.14: Potential well scaling with B. For each data point in Fig. 5.13 with $B_{max} > 15$ mT the difference in the two probe potentials is taken to be indicative of the change in overall potential well depth. The resulting trend is approximately linear.

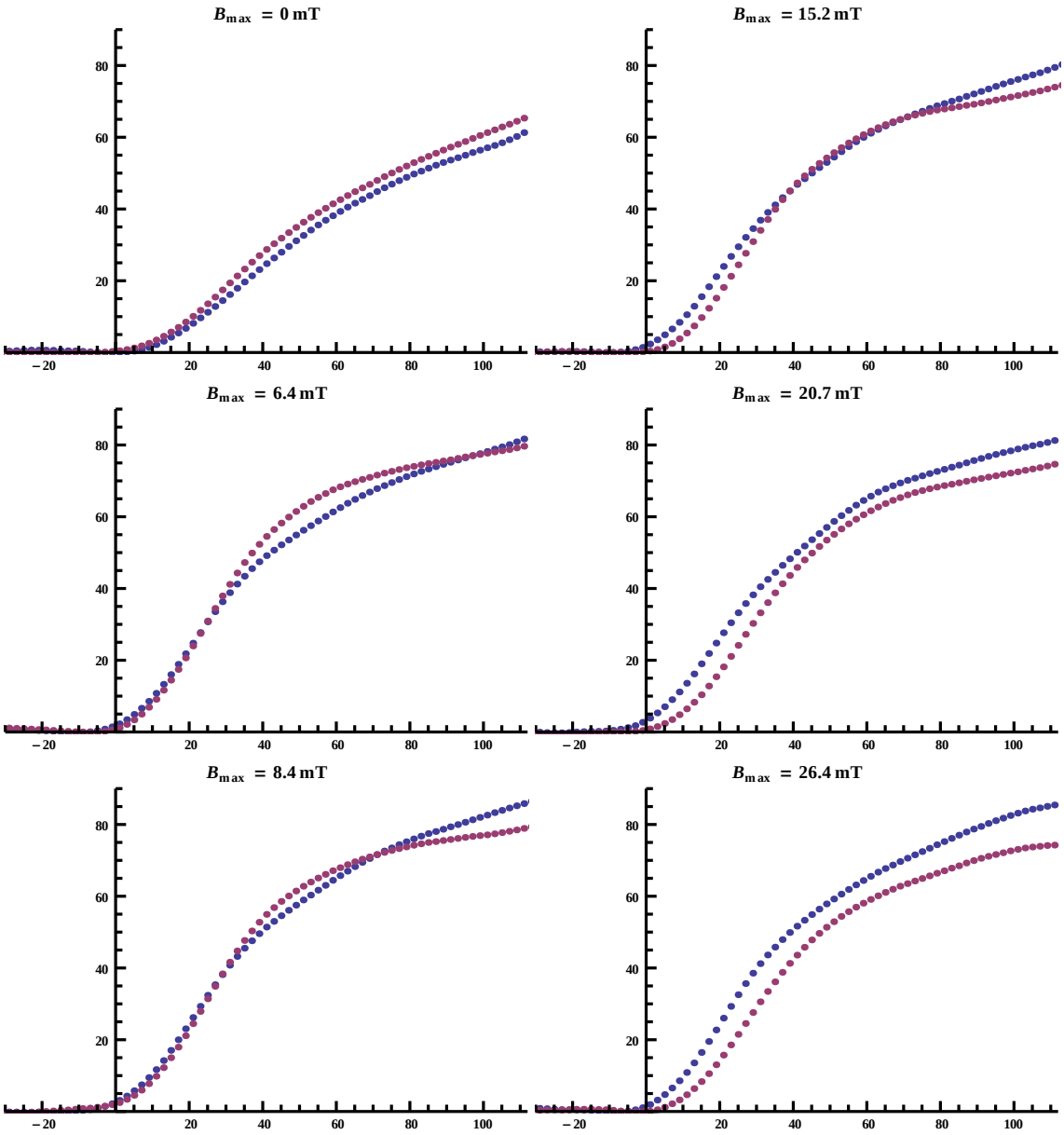


Figure 5.15: A grid of sample probe traces from the magnetic field scaling data sets in Figure 5.13. The blue data trace is Probe A in the centre of the device null, while the red data trace is Probe B, located at half the device radius.

Although changing the bias voltage effectively changes the injection energy of the electrons, it also changes the injection current, and hence affects the ultimate electron density $n_e$ obtained in the well. It was not possible to separate these two effects because they have an opposite effect on the results. An increase in the electron density, with increasing injection current, leads to a linear increase in the potential well depth, $V_{well}$, given in Eqn. 5.13. Increasing the extraction voltage gives an exponential increase in the current emitted from the filaments, but does not necessarily mean an exponential increase in the current entering the Polywell since this is a complex function of the geometry and is space charge limited.

By comparison, increasing the energy of the electrons leads to a decrease in the electron confinement time because a higher energy electron population needs a higher magnetic field to achieve the same degree of adiabatic mirror confinement. However, this effect is at a maximum when the adiabatic flux surface becomes larger than half the device radius, beyond which the degree of mirror confinement decays rapidly. Fig. 5.17 supports this hypothesis since it shows the potential well scales linearly with injected current until the injected electron energy is sufficiently large such that competing effects are introduced.

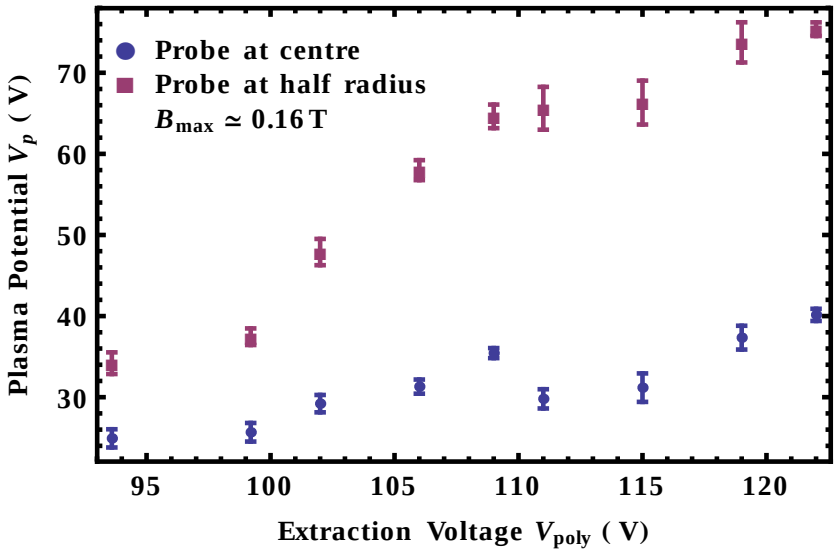


Figure 5.16: The change in potential well formation with extraction voltage, $V_{poly}$. The variation is determined by two competing parameters, the injected electron density and average energy.

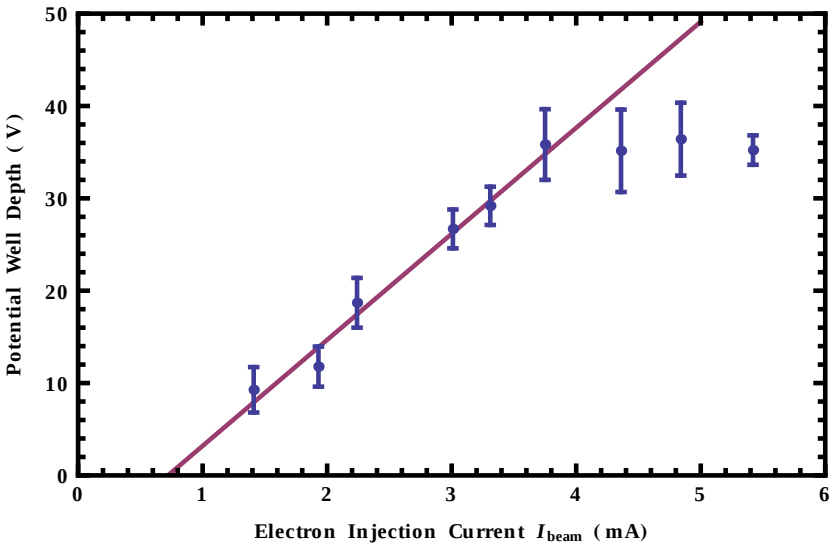


Figure 5.17: Potential well scaling with the injected electron current $I_{beam}$. Here the potential difference between the two probes in Fig. 5.16 is assumed to be indicative of the overall change in well depth, and plotted as a function of the injected beam current.

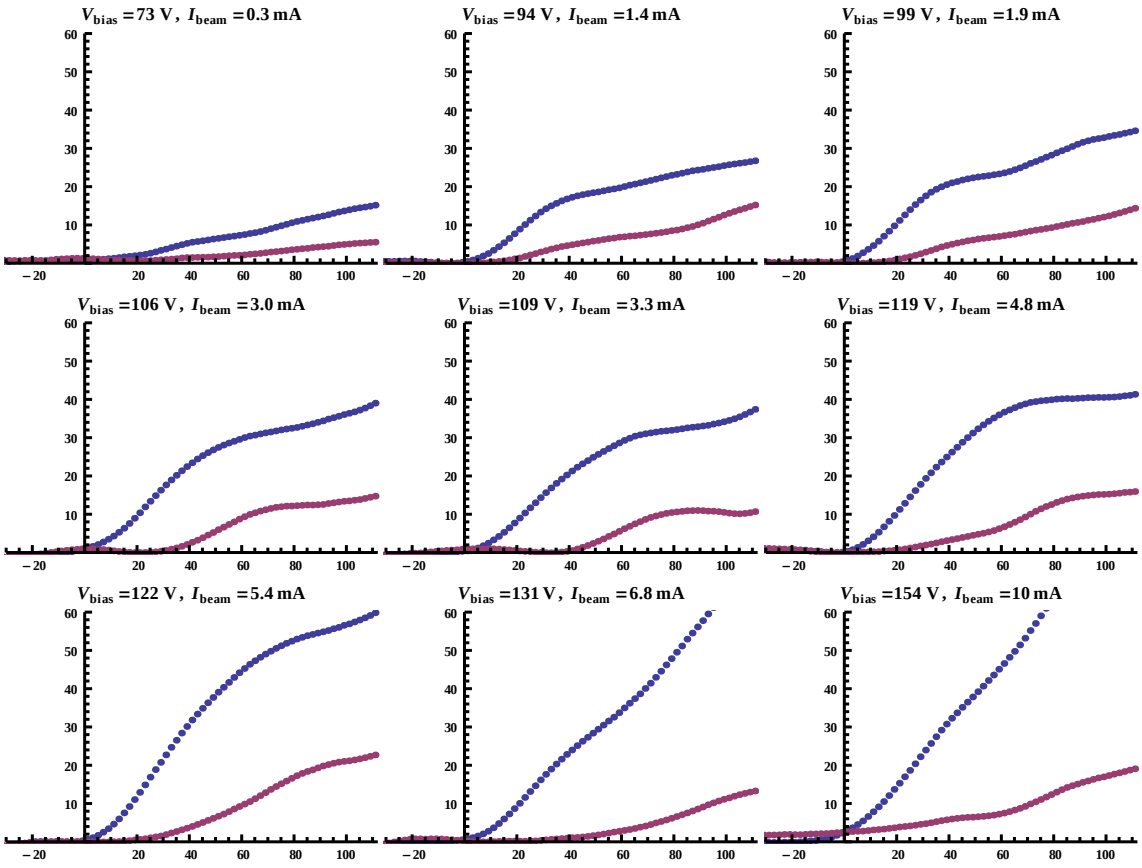


Figure 5.18: A grid of sample energy scaling $I(V)$ traces from the data sets in Figures 5.16 and 5.17. The $I(V)$ traces are labelled by their extraction voltage $V_{bias}$ and extraction current $I_{beam}$. The blue data trace is Probe A in the centre of the device null, while the red data trace is Probe B, located at half the device radius.

## 5.8 Summary

- Biased Langmuir probes have been used to characterise potential well formation as a function of a number of Polywell parameters, such as magnetic field strength and injection energy.

- Orbital Limited Motion theory was used to measure and confirm the EEDF of injected electrons. This information was combined with knowledge of the types of possible electron trajectories [64, 74] to propose an EEDF for the electron population in the magnetic null. The proposed EEDF $I_\mu(V)$ is in good agreement with the collected data.

- The proposed $I_\mu(V)$ was used to study the spatial change of the plasma potential $V_p$ across the device, and confirmed a potential well had formed. However the shape of the potential well did not agree with the simple parabolic shape predicted by Poisson's equation and previously measured by Krall [81]. This may be because of experimental device was too small to accurately measure the spatial variation of the plasma potential without averaging the spatial features over the probe length scale.

- Potential well formation was found to scale linearly with increasing magnetic field and injection current, in good agreement with the currently proposed confinement models. Dependence on injection energy was also measured, but obscured by the competing effect of injection current scaling. It is proposed that the potential well formation scaled linearly with injection current until competing effects from increasing the extraction energy changed the confinement properties.

- The proposed $I_\mu(V)$ provides a powerful diagnostic for studying Polywell physics providing $f_\mu(v_r)$ is an accurate representation of the underlying EEDF. To confirm the interpretation of the $I(V)$ is correct, the biased probe technique discussed in this paper should be combined with another probe technique that is less dependant on the shape of the EEDF. If the $V_p$'s of the two techniques are in agreement, then all other derived parameters from $I_\mu(V)$ can be considered accurate. One such technique is the capacitive probe technique used previously on the HEPS experiment [81, 109]. Additionally, emissive probes have been shown to allow uncomplicated analysis of the $V_p$ through the deviation potential in electron only plasmas [125, 126].

Chapter 6

# Conclusions and Further Work

The magnetic field structure of the Polywell has been analysed in its complete form, as well as areas of interest such as the point and line cusps. It has been found that at small spacings it is possible for point cusp losses to dominate over line cusp losses, allowing the application of conventional point cusp theories to the Polywell. The dominance of point cusp losses may prove beneficial in terms of providing a lower overall loss rate when compared with other devices such as the biconic cusp. The types of trajectories that can occur have been analysed in terms of their adiabaticity. It was found that the two component trajectories described in models of biconic cusp confinement can be adapted to the Polywell. The resulting model describes a critical flux surface separating the two types of trajectories, and also defines the minimum field, $B_0$, needed for evaluating the mirror reflection coefficients.

The described trajectories suggest a simplified ballistic scattering model can be used to describe the confinement time in the device. Such a model was described and found to be in reasonable agreement with a single particle SIMION simulation with parameters matching our current experimental parameters. This model should be extended for a number of cases. The presence of a virtual cathode would be expected to slightly modify the overall confinement time model since it will lead to deceleration followed by acceleration every time an electron passes through the device null. This additional behaviour could be simulated in SIMION by superimposing an electrostatic potential well over the vacuum magnetic field. The new behaviour could be added to the model of confinement time behaviour in Chapter 2.

The next case that should be considered is the case of high $\beta$. The exact shape of the $\beta = 1$ boundary would need to be evaluated numerically by balancing the magnetic pressure with the kinetic pressure, $p_m = p_k$, at each point along the sheath boundary. Additionally $\vec{B}$ must be tangential at the boundary and be equal to the vacuum magnetic field anywhere between the sheath edge and the coils [59]. These calculations would allow an estimate of the reduction of point cusp losses in high beta and could be compared with Bussard's model for high $\beta$ confinement [64]. A further effect which may aid in reducing electron losses from the point cusps is space charge plugging. A number of experiments have demonstrated that electrostatic plugging of cusps can improve confinement [77]. A model of point cusp plugging could be integrated into the confinement model developed in this thesis.

The central well approximation was developed as a tractable analytical approximation to the Polywell magnetic field. It could be used for exploring further analytical models of confinement or for evaluating the shape of the $\beta = 1$ surface.

The Teflon Polywell was our first prototype device aimed at obtaining qualitative validity of

the Polywell concept. Floating potentials of up to –250 V were obtained for periods of several milliseconds, suggesting the formation of a virtual cathode stable on at least the millisecond time scale. Floating potential formation was measured as a function of Polywell coil current, electron injection parameters such as energy and beam current, and the background gas pressure.

It was shown that the virtual cathode does not form outside of a narrow range of coil currents in this design. A number of reasons for this behaviour were explored including mirror reflection of the injected electron beam, the concept of a secondary low energy electron population being produced by the hollow cathode, and possibly a multi-valued floating potential due to the presence of electron populations with differing energies. Ultimately it was not possible to precisely determine the cause of this behaviour. The cylindrical hollow cathode electron gun is a new technology and there is a new experimental effort under-way to optimise its behaviour as an electron gun [18].

Potential well formation was shown to be extremely sensitive to the background gas pressure. It was concluded that increasing the background gas pressure results in increased ionisation which counteracts potential well formation. A balance must be found between increasing the background gas pressure for creating meaningful ion densities in the core and decreasing the background gas density for reducing the destructive effects of ionisation.

A collector plate experiment was constructed to explore the redistribution of the electron beam current during Polywell operation. Data from both collector plates suggested that a fraction of the electron beam was redistributed amongst the coil faces through ballistic collisions around the magnetic null. However the magnetic field in that experiment should have been too low to produce mirror reflections. The experimental results of this chapter provided good qualitative evidence of potential well formation but motivated the need for a more precise diagnostic. Lessons learned from this set of experiments were employed in the design of the biased Langmuir probe experiment.

Orbital Limited Motion theory was used to characterise potential well formation as a function of a number of Polywell parameters, such as magnetic field strength and injection energy. The biased probe theory was used to confirm the EEDF of injected electrons and showed excellent agreement with the distribution proposed by Langmuir. This information was combined with knowledge of the types of possible electron trajectories [64, 74] to propose an EEDF for the electron population in the magnetic null. The proposed EEDF $I_\mu(V)$ is in good agreement with the collected data. The proposed $I_\mu(V)$ was then used to study the spatial change of the plasma potential $V_p$ across the device, and confirmed a potential well had formed.

Potential well formation was found to scale linearly with increasing magnetic field and injection current, in good agreement with the currently proposed confinement models. Dependence on injection energy was also measured, but obscured by the competing effect of injection current scaling. It is proposed that the potential well formation scaled linearly with injection current until competing effects from increasing the extraction energy changed the confinement properties.

The proposed $I_\mu(V)$ provides a powerful diagnostic for studying Polywell physics providing $f_\mu(v_r)$ is an accurate representation of the underlying EEDF. To confirm the interpretation of

the $I(V)$ is correct, the biased probe technique discussed in this thesis needs to be combined with another probe technique that is less dependant on the shape of the EEDF. Multiple diagnostic techniques could be used to confirm the plasma potential is correct, then all other derived parameters from $I_\mu(V)$ can be considered accurate.

One such technique is the capacitive probe technique used previously on the HEPS experiment [81, 109]. Additionally, emissive probes have been shown to allow uncomplicated analysis of the $V_p$ through the deviation potential in electron only plasmas [126]. Kremer et al. [125] showed that the $I(V)$ of a biased emissive probe will deviate from the $I(V)$ of a biased cold probe near the plasma potential. Furthermore, their experiments were carried out on a non-neutral Tokamak and hence could likely be adapted for use on a Polywell. The primary goal of such an experiment would be to show agreement between multiple techniques.

The biased probe technique developed in this thesis could be used in a larger Polywell device to achieve greater spatial accuracy of the radial plasma potential profile. On the WB6-mini device the probe would have locally averaged out the plasma potential and made it difficult to confirm the predicted parabolic potential well profile. In addition, future experiments should aim to achieve much higher electron gun currents so that potential wells can approach high fractions of the gun energy.

The biased probe technique could be further developed to account for changed behaviour of the saturation region in a moderate magnetic field. This would allow the biased probe to be used in the point cusps for measuring/estimating the electron loss rate. Measuring electron leakage through the cusps would help answer fundamental questions about how the power loss through electron leakage compared with the potential fusion power. Furthermore, the biased probe demonstrated that $V_\mu/V_{th} \gg 1$ under steady state low $\beta$ conditions. The biased probe technique could be used to measure the rate of thermalisation as a function of device parameters such as magnetic field strength and the mirror reflection coefficients. The ultimate aim of such an experiment would be to potentially confirm the ideas of Rosenberg and Krall [86] by showing that the Polywell can passively maintain non-equilibrium, perhaps addressing the concerns raised by Polywell critics [33, 35, 36].

Chapter 7

# Bibliography

## General References


[1] C. Braams and P. Stott. *Nuclear fusion: half a century of magnetic confinement fusion research*. Taylor & Francis, 2002.

[2] D.L. Bruhwiler et al. "Particle-in-cell simulations of plasma accelerators and electron-neutral collisions". In: *Physical Review Special Topics - Accelerators and Beams* 4.10 (2001), p. 101302.

[3] D.L. Bruhwiler et al. "Particle-in-cell simulations of tunneling ionization effects in plasma-based accelerators". In: *Physics of Plasmas* 10 (2003), p. 2022.

[4] US Census Bureau. *World POPClock Projection*. Jan. 2013. URL: http://www.census.gov/main/www/popclock.html.

[5] R.C. Cross et al. "The TORTUS tokamak". In: *Atomic Energy in Australia* 24 (1981), pp. 2–10.

[6] David A Dahl. "SIMION for the personal computer in reflection". In: *International Journal of Mass Spectrometry* 200.1 (2000), pp. 3–25.

[7] BH Duane. *Fusion Cross Section Theory*. Tech. rep. 1972.

[8] US Department of Energy. "A technology roadmap for generation IV nuclear energy systems". In: *Washington December* (2002).

[9] Atomic Mass Data Center (FR). *Table of Isotopes*. Jan. 2013. URL: http://amdc.in2p3.fr/nubase/nubtab03.asc.

[10] J. Huba. *NRL: plasma formulary*. Tech. rep. DTIC Document, 2004.

[11] M. Keilhacker et al. "The scientific success of JET". In: *Nuclear fusion* 41.12 (2002), p. 1925.

[12] K. Krane. *Introductory nuclear physics*. John Wiley and Sons Inc., New York, NY, 1987.

[13] D. MacKay. *Sustainable Energy-without the hot air*. UIT Cambridge, 2008.

[14] G.H. Miley, H. Towner, and N. Ivich. *Fusion cross sections and reactivities*. Tech. rep. Illinois Univ., Urbana (USA), 1974.

[15] Scientific Instrument Services. *Simion - Charged Particle Optics Software*. Feb. 2013. URL: http://simion.com/.

[16] G. Van Oost and R. Jaspers. "Thermonuclear Burn Criteria". In: *Fusion Science and Technology* 61.2 (2012).

[17] JP Verboncoeur. "OOPIC: object oriented particle-in-cell code". In: *Plasma Science, 1995. IEEE Conference Record-Abstracts., 1995 IEEE International Conference on*. IEEE. 1995, p. 244.

## IEC

[18] S. Cornish and Khachan J. *A simple self extracting plasma cathode electron gun for beam generation*. Currently under review, 2013.

[19] W. Elmore, J. Tuck, and K. Watson. "On the Inertial-Electrostatic Confinement of a Plasma". In: *Physics of Fluids* 2 (1959), p. 239.

[20] P. Farnsworth. *Electric discharge device for producing interactions between nuclei*. US Patent 3,258,402. June 1966.

[21] P. Farnsworth. *Method and apparatus for producing nuclear-fusion reactions*. US Patent 3,386,883. 1968.

[22] M. Fitzgerald. "Discharge Physics and Plasma Transport in Inertial Electrostatic Confinement Devices". PhD thesis. University of Sydney, Apr. 2009.

[23] R. Hirsch. "Experimental studies of a deep, negative, electrostatic potential well in spherical geometry". In: *Physics of Fluids* 11 (1968), p. 2486.

[24] R. Hirsch. "Inertial-Electrostatic Confinement of Ionized Fusion Gases". In: *Journal of Applied Physics* 38.11 (1967), pp. 4522–4534. ISSN: 0021-8979.

[25] J. Kipritidis. "The Application of Doppler H$\alpha$ Spectroscopy to the Prediction of Experimental Fusion Rates in a deuterium-filled Inertial Electrostatic Confinement device". PhD thesis. University of Sydney, July 2009.

[26] J. Kipritidis and J. Khachan. "Application of Doppler spectroscopy in H_ {2} to the prediction of experimental D (d, n)ˆ{3} He reaction rates in an inertial electrostatic confinement device". In: *Physical Review E* 79.2 (2009), p. 26403. ISSN: 1550-2376.

[27] J. Kipritidis et al. "Absolute densities of energetic hydrogen ion species in an abnormal hollow cathode discharge". In: *Physical Review E* 77.6 (2008), p. 66405. ISSN: 1550-2376.

[28] *Overview of University of Wisconsin IEC Research*. 2009.

[29] O. Lavrentev. "On electrostatic plasma confinement - Part I". In: *Ukrainian Journal of Physics* 8 (1963).

[30] *Overview of Kyoto University Research and Considerations for an IEC Device Driven by a Built-In Ring-Shaped Ion Source*. 2009.

[31] *Overview of University of Illinois IEC Research and Issues for IEC Potential Well Operation*. 2009.

[32] *High-pulsed operation of an inertial electro-static confinement device.* 1999.

[33] WM Nevins. "Can inertial electrostatic confinement work beyond the ion–ion collisional time scale?" In: *Physics of Plasmas* 2 (1995), p. 3804.

[34] *Application of IECF to Neutron Radiography.* 2011.

[35] T. Rider. "A general critique of inertial-electrostatic confinement fusion systems". In: *Physics of Plasmas* 2 (1995), p. 1853.

[36] T. Rider. "Fundamental limitations on plasma fusion systems not in thermodynamic equilibrium". In: *Physics of Plasmas* 4 (1997), p. 1039.

[37] T. Rider. "Modification of classical Spitzer ion-electron energy transfer rate for large ratios of ion to electron temperatures". In: *Physics of Plasmas* 2 (1995), p. 1873.

[38] O. Shrier. "Spectroscopy and modelling of ion charge exchange in energetic discharges used in nuclear fusion". PhD thesis. University of Sydney, July 2007.

[39] O. Shrier, J. Khachan, and S. Bosi. "A Markov chain approach to modelling charge exchange processes of an ion beam in monotonically increasing or decreasing potentials". In: *Journal of Physics A: Mathematical and General* 39.35 (2006), p. 11119.

[40] O. Shrier et al. "Diverging ion motion in an inertial electrostatic confinement discharge". In: *Physics of plasmas* 13 (2006), p. 012703.

[41] T.A. Thorson et al. "Fusion reactivity characterization of a spherically convergent ion focus". In: *Nuclear Fusion* 38.4 (1998), p. 495.

## Plasma Physics Textbooks

[42] L. Artsimovich. *Controlled thermonuclear reactions.* Gordon and Breach, 1964.

[43] F. Chen. *Introduction to plasma physics and controlled fusion: Plasma physics.* Plenum Pub Corp, 1984.

[44] S. Glasstone and R.H. Lovberg. *Controlled thermonuclear reactions: an introduction to theory and experiment.* Robert E. Krieger, 1975.

[45] M.A. Lieberman and A.J. Lichtenberg. "Principles of plasma discharges and materials processing". In: *MRS Bull* 30 (2005), p. 899.

[46] D. Rose and M. Clark. *Plasmas and controlled fusion.* M.I.T. Press, 1961.

[47] W. Stacey. *Fusion: An introduction to the physics and technology of magnetic confinement fusion.* Wiley-VCH, 2010. ISBN: 352740967X.

[48] W. Stacey. *Fusion plasma analysis.* Wiley-Interscience, New York, 1981.

## Magnetic Fields

[49] J. Berkowitz, H. Grad, and H. Rubin. "Magnetohydrodynamic Stability". In: *Proceedings of the Second United Nations International Conference on the Peaceful Uses of Atomic Energy*. United Nations, Geneva, 1958.

[50] R. Good. "Elliptic integrals, the forgotten functions". In: *European Journal of Physics* 22 (2001), p. 119.

[51] H. Grad. "Minimum B as a plasma stability criterion". In: *Physical Review Letters* 16.25 (1966), pp. 1147–1150. ISSN: 1079-7114.

[52] D. Griffiths. *Introduction to electrodynamics*. Vol. 3. Prentice Hall New Jersey; 1999.

[53] J.D. Jackson. *Classical Electrodynamics*. John Wiley and Sons, Inc., New York, 1999.

[54] V. Zworykin, G. Morton, and E. Ramberg. *Electron optics and the electron microscope*. John Wiley and Sons, Inc., New York, 1945.

## Mirror Machines

[55] R. Post. "The magnetic mirror approach to fusion". In: *Nuclear Fusion* 27 (1987), p. 1579.

## Cuspped Geometries

[56] J. Berkowitz et al. "Cusped geometries". In: *Proceedings of the 2nd Int. Conference on Peaceful Uses of Atomic Energy*. Vol. 1. 1958, pp. 146–155.

[57] H. Grad. *Containment in Cusped Plasma Systems*. Tech. rep. New York University, New York Institute of Mathematical Sciences, 1961.

[58] H. Grad. "Plasma trapping in cusped geometries". In: *Physical Review Letters* 4.5 (1960), pp. 222–223. ISSN: 1079-7114.

[59] M. Haines. "Plasma containment in cusp-shaped magnetic fields". In: *Nuclear Fusion* 17.4 (1977), p. 811.

[60] M. Sadowski. "Containment time of plasma in the SM magnetic trap". In: *Physics Letters A* 28.9 (1969), pp. 626–627.

[61] M. Sadowski. "Plasma confinement with spherical multipole magnetic field". In: *Physics Letters A* 25.9 (1967), pp. 695–696. ISSN: 0375-9601.

[62] M. Sadowski. "Plasma containment in a spherical multipole magnetic trap". In: *Journal of Plasma Physics* 4.01 (1970), pp. 1–12. ISSN: 0022-3778.

[63] R. Van Norton. *The motion of a charged particle near a zero field point*. Tech. rep. New York University, New York Institute of Mathematical Sciences, 1961.

## The Polywell

[64] R. Bussard. *Electron Leakage Through Magnetic Cusps in the Polywell Confinement Geometry*. Tech. rep. Directed Technologies Inc., Arlington VA, 1991.

[65] R. Bussard. *Method and apparatus for controlling charged particles*. US Patent 4,826,646. May 2, 1989.

[66] R. Bussard. *Preliminary Study of Inertial Electrostatic-Fusion (IEF) for Electric Power Plants*. Tech. rep. Final Report, EPRI Contract RP-8012-16, Energy/Matter Conversion Corp., EMC2-0693-01, 1994.

[67] R. Bussard. "Should Google Go Nuclear? Clean Cheap Nuclear Power". In: *Google Tech Talks* (2006).

[68] R. Bussard. "Some Physics Considerations of Magnetic Inertial-Electrostatic Confinement: A New Concept for Spherical Converging-Flow Fusion". In: *Fusion Technology* 19.2 (1991), pp. 273–293.

[69] R. Bussard. "The Advent of Clean Nuclear Fusion: Superperformance Space Power and Propulsion". In: *57th International Astronautical Congress, IAC*. 2006.

[70] R. Bussard and D. Gray-Bussard. *Method and apparatus for controlling charged particles*. US Patent App. 11/905,183. Sept. 2008.

[71] R. Bussard and N. Krall. "Comments on 'Ion defocusing in multicusp plasma confinement systems'". In: *Fusion technology* 25 (1994), p. 228.

[72] R. Bussard and N. Krall. "Inherent characteristics of fusion power systems: physics, engineering, and economics". In: *Fusion technology* 26.4 (1994), pp. 1326–1336.

[73] R.W. Bussard. *Method and apparatus for creating and controlling nuclear fusion reactions*. US Patent 5,160,695. Nov. 3, 1992.

[74] M. Carr et al. "Low beta confinement in a Polywell modelled with conventional point cusp theories". In: *Physics of Plasmas* 18 (2011), p. 112501.

[75] Energy Matter Conversion Corporation. *EMC2 Fusion Development Corporation*. Jan. 2013. URL: http://www.emc2fusion.org/.

[76] T Dolan. "Ion defocusing in multicusp plasma confinement systems". In: *Fusion Technology* 24 (1993), p. 128.

[77] T Dolan. "Magnetic electrostatic plasma confinement". In: *Plasma physics and controlled fusion* 36 (1994), p. 1539.

[78] T Dolan. "Response to "Comments on 'Ion defocusing in multicusp plasma confinement systems'"". In: *Fusion Technology* 25 (1994), p. 229.

[79] F. Kazemyzade et al. "Dependence of Potential Well Depth on the Magnetic Field Intensity in a Polywell Reactor". In: *Journal of Fusion Energy* (2011), pp. 1–5.

[80] N. Krall. "The Polywell: A Spherically Convergent Ion Focus Concept". In: *Fusion technology* 22.1 (1992), pp. 42–49.

[81] N. Krall et al. "Forming and maintaining a potential well in a quasispherical magnetic trap". In: *Physics of Plasmas* 2.1 (1995), pp. 146–158. ISSN: 1070-664X.

[82] *A Polywell p+11B Power Reactor*. 2011.

[83] *Designing a Small-Scale D+D Reactor*. 2012.

[84] *Evaluation of Net Power Polywell Designs*. 2010.

[85] *Two-dimensional (2D) Particle-in-cell (PIC) Simulation of Polywell*. 2009.

[86] M. Rosenberg and N. Krall. "The effect of collisions in maintaining a non-Maxwellian plasma distribution in a spherically convergent ion focus". In: *Physics of Fluids B: Plasma Physics* 4 (1992), p. 1788.

[87] J. Santarius and K. Simmons. "Performance of Polywell inertial-electrostatic confinement for applications". In: *1995 IEEE International Conference on Plasma Science*. IEEE. 1995, p. 258. ISBN: 0780326695.

[88] K. Simmons and J. Santarius. "Numerical simulation of the Polywell device". In: *1995 IEEE International Conference on Plasma Science*. IEEE. 1995, p. 258. ISBN: 0780326695.

## Electronics

[89] R.C. Cross. "Current transformers". In: *American Journal of Physics* 54.12 (1986).

[90] P. Horowitz and W. Hill. *The art of electronics*. Cambridge university press, 1989.

[91] Freetronics Pty Ltd. *Freetronics LCD & Keypad Shield*. Jan. 2013. URL: http://www.freetronics.com/collections/display/products/lcd-keypad-shield.

[92] Power Electronic Measurements Ltd. *The IRF AC current transducer*. Jan. 2013. URL: http://www.pemuk.com/irf.html.

[93] J.H. Moore et al. *Building scientific apparatus*. Vol. 4. Cambridge University Press New York, 2009.

[94] P. Scherz. *Practical Electronics for Inventors 2/E*. McGraw Hill Professional, 2006.

[95] Open Source Arduino Team. *The Arduino Mega 2560*. Jan. 2013. URL: http://arduino.cc/en/Main/ArduinoBoardMega2560.

[96] T. Williams. *The circuit designer's companion*. Newnes, 2010.

## Diagnostics

[97] I.B. Bernstein and I.N. Rabinowitz. "Theory of Electrostatic Probes in a Low-Density Plasma". In: *Physics of Fluids* 2 (1959), p. 112.

[98] F.F. Chen. "Electric probes". In: *Plasma diagnostic techniques*. Vol. 1. 1965, p. 113.

[99] M. Druyvesteyn and F. Penning. "The mechanism of electrical discharges in gases of low pressure". In: *Reviews of Modern Physics* 12.2 (1940), pp. 87–174.

[100] A. Heatley. "Collector Theory for Ions with Maxwellian and Drift Velocities". In: *Physical Review* 52.3 (1937), p. 235.

[101] N. Hershkowitz. "How Langmuir probes work". In: *Plasma Diagnostics* 1 (1989), pp. 113–183.

[102] I. Langmuir and H. Mott-Smith. "Studies of electric discharges in gases at low pressures Part I–V". In: *General Electric Rev* 27 (1924).

[103] F. Magnus and J. Gudmundsson. "Digital smoothing of the Langmuir probe I-V characteristic". In: *Review of Scientific Instruments* 79.7 (2008), pp. 073503 –073503–8.

[104] H. Mott-Smith and I. Langmuir. "The Theory of Collectors in Gaseous Discharges". In: *Phys. Rev.* 28 (4 1926), pp. 727–763.

[105] C.H. Nam et al. "Multiple valued floating potentials of Langmuir probes". In: *Journal of applied physics* 63.12 (1988), pp. 5674–5677.

[106] B. Polychronopulos. "Effects on non-Maxwellian electron energy distributions on the orbital limited current-voltage characteristics of cylindrical and spherical Langmuir probes under collisionless conditions". In: *Plasma Physics* 15.1 (1973), pp. 37–48.

[107] A. Savitzky and M. J. E. Golay. "Smoothing and Differentiation of Data by Simplified Least Squares Procedures". In: *Analytical Chemistry* 36.8 (1964), p. 1627.

[108] J. Swift and M. Schwar. "Electrical Probes for Plasma Diagnostics." In: (1970).

[109] E. Wang et al. "Secondary electron emission-capacitive probes for plasma potential measurements in plasmas with hot electrons". In: *Journal of applied physics* 61.10 (1987), pp. 4786–4790.

## Advanced Fuels

[110] W. Barr et al. "A preliminary engineering design of a Venetian blind direct energy converter for fusion reactors". In: *IEEE transactions on Plasma Science* 2.2 (1974), pp. 71–92.

[111] G. Kulcinski and J. Santarius. *New Opportunities for Fusion in the 21st Century - Advanced Fuels*. 14th Topical Meeting, American Nuclear Society, Park City, Utah, Oct 17-20. 2000.

[112] G.L. Kulcinski et al. "Apollo-L3, an advanced fuel fusion power reactor utilizing direct and thermal energy conversion". In: *Presented at the 9th Topical Meeting on the Technology of Fusion Energy*. Vol. 7. 1990, p. 11.

[113] G. Miley et al. “Conceptual design for a D-3He IEC pilot plant”. In: *Fusion Engineering, 15th IEEE/NPSS Symposium on*. Vol. 1. IEEE. 1993, pp. 161–164. ISBN: 0780314123.

[114] R. Moir. “Direct energy conversion in fusion reactors”. In: *Energy technology handbook* 5 (1977), pp. 5–150–5–154.

[115] R. Moir and W. Barr. “Venetian-blind direct energy converter for fusion reactors”. In: *Nuclear Fusion* 13 (1973), p. 35.

[116] J. Santarius et al. “Could advanced fusion fuels be used with today’s technology?” In: *Journal of fusion energy* 17.1 (1998), pp. 33–40.

## Applications of Fusion Research

[117] B. Eastland and W. Gough. “Near term recycling option using fusion grade plasmas”. In: *Fusion Technology* 20.2x (1991).

[118] B. Eastlund. “A market oriented approach to fusion technology”. In: *Journal of fusion energy* 12.4 (1993), pp. 335–348. ISSN: 0164-0313.

[119] G. Kulcinski. “Near term commercial opportunities from long range fusion research”. In: *Presented at the 12th Topical Meeting on the Technology of Fusion Power*. Vol. 16. 1996, p. 20.

[120] G. Kulcinski. “Non-Electric Applications of Fusion Energy-An Important Precursor to Commercial Electric Power”. In: *Presented at the 13th Topical Meeting on the Technology of Fusion Power*. 1998.

[121] G. Kulcinski. “Non-electrical power, near-term applications of fusion energy”. In: *Fusion Engineering, 1999. 18th Symposium on*. IEEE. 1999, pp. 5–8. ISBN: 0780358295.

[122] G. Kulcinski and J. Santarius. “Reducing the barriers to fusion electric power”. In: *Journal of fusion energy* 17.1 (1998), pp. 17–23. ISSN: 0164-0313.

[123] G. Kulcinski et al. “Alternate applications of fusion-production of radioisotopes”. In: *Fusion science and technology* 44.2 (2003), pp. 559–563. ISSN: 1536-1055.

[124] K. McCarthy et al. “Nonelectric applications of Fusion”. In: *Journal of fusion energy* 21.3 (2002), pp. 121–153. ISSN: 0164-0313.

Appendix A

# Derivations

## A.1 The monoenergetic isotropic distribution function

The projection of the monoenergetic isotropic distribution into a 2D plane was used in Langmuir's original work on biased probes [104]. However it is not derived or cited in that work [104]. It is presented here because of its relationship to the isotropic mean energy distribution, $f_\mu$, derived in this thesis. My derivation is as follows.

First, consider the case of an isotropic distribution of electrons with uniform speed (monoenergetic). This distribution can be described as

$$f_{iso}(v_r) = \begin{cases} \frac{1}{N}, & \text{if } v_r = v_0 \\ 0, & \text{if } v_r \neq v_0 \end{cases} \tag{A.1}$$

where $N$ is the normalisation constant, $v_r$ is the magnitude of the velocity, and $v_0$ is the monoenergetic speed. The integral of this distribution function over all space must be 1, hence we can define

$$\int_\Omega f_{iso}(v_r) d\mathbf{a} = \int_0^{2\pi} \int_0^{\pi} f_{iso}(v_r) v_r^2 \sin(\phi) d\phi d\theta = 1 \tag{A.2}$$

To use the distribution in Langmuir's orbital limited motion theory we need to map this distribution into the $(x, y)$ plane. Or equivalently, we need to map $(\theta, \phi)$ to $(v_x, v_y)$, using to coordinate system

$$v_x = v_r \sin(\phi) \cos(\theta) \tag{A.3}$$

$$v_y = v_r \sin(\phi) \sin(\theta) \tag{A.4}$$

$$v_z = v_r \cos(\phi) \tag{A.5}$$

and hence the determinate of the Jacobian is

$$\frac{\partial(v_x, v_y)}{\partial(\phi, \theta)} = v_r^2 \cos(\phi) \sin(\phi) \tag{A.6}$$

Now we need to transform the integral, and set $f_{iso}(v_r) = \frac{1}{N}$ since not integrating over $v_r$.

$$\int_0^{2\pi} \int_0^{\pi} f_{iso}(v_r) v_r^2 \sin(\phi) d\phi d\theta = \int_0^{\infty} \int_0^{\infty} f_{iso}(v_r) v_r^2 \sin(\phi) \frac{\partial(\phi, \theta)}{\partial(v_x, v_y)} dv_x dv_y \tag{A.7}$$

$$= \int_0^{\infty} \int_0^{\infty} \frac{1}{N \cos(\phi)} dv_x dv_y \tag{A.8}$$

and therefore we can define the distribution function for the velocities in the $(x, y)$ plane as

$$\therefore f_{iso}(v_x, v_y) = \frac{1}{N\cos(\phi)} \tag{A.9}$$

But $\cos(\phi) = v_z/v_0$, and hence can be re-written in terms of $v_x$, and $v_y$ by algebraic manipulation.

$$v_x^2 + v_y^2 + v_z^2 = v_0^2 \tag{A.10}$$

$$\therefore \frac{v_z^2}{v_0^2} = 1 - \frac{v_x^2 + v_y^2}{v_0^2} \tag{A.11}$$

$$\therefore \frac{1}{\cos(\phi)} = \frac{1}{\sqrt{1 - \frac{v_x^2+v_y^2}{v_0^2}}} \tag{A.12}$$

We can find the normalisation constant by integration over the boundary $v_x^2 + v_y^2 \leq v_0^2$.

$$N = \int_{-v_0}^{v_0} \int_{-v_0\sqrt{1-v_x^2/v_0^2}}^{v_0\sqrt{1-v_x^2/v_0^2}} \frac{1}{\sqrt{1 - \frac{v_x^2+v_y^2}{v_0^2}}} dv_y dv_x = 2\pi v_0^2 \tag{A.13}$$

$$\therefore f_{iso}(v_x, v_y) = \frac{1}{2\pi v_0^2 \sqrt{1 - \frac{v_x^2+v_y^2}{v_0^2}}} \tag{A.14}$$

## A.2 Potential Well Derivation

We need to solve Poisson's equation in radial coordinates.

$$\frac{1}{r^2}\frac{\partial}{\partial r}\left(r^2 \frac{\partial}{\partial r} V\right) = -\frac{n_e q}{\epsilon_0} \tag{A.15}$$

$$\therefore r^2 \frac{\partial}{\partial r} V = -\int \frac{r^2 n_e q}{\epsilon_0} dr = -\frac{r^3}{3}\frac{n_e q}{\epsilon_0} + C \tag{A.16}$$

For the boundary conditions let $\frac{\partial v}{\partial r} = 0$ at $r = 0$, and therefore $C = 0$.

$$\therefore \frac{\partial V}{\partial r} = -\frac{r}{3}\frac{n_e q}{\epsilon_0} \tag{A.17}$$

$$V = -\int \frac{r}{r} dr \left(\frac{n_e q}{\epsilon_0}\right) = -\frac{r^2}{6}\frac{n_e q}{\epsilon_0} + D \tag{A.18}$$

At the maximum radius $R$, let $V = 0$.

$$\therefore 0 = -\frac{r^2}{6}\frac{n_e q}{\epsilon_0} + D \tag{A.19}$$

$$\therefore D = \frac{R^2}{6}\frac{n_e q}{\epsilon_0} \tag{A.20}$$

Therefore, the resulting equation for the potential as a function of radius is

$$V = \frac{n_e q}{6\epsilon_0}\left[r^2 - R^2\right]. \tag{A.21}$$

Let us set $r = 0$ to find the potential well depth, $V_{well}$, in the core due to an electron density $n_e$ and device radius $R$,

$$V_{well} = -\frac{n_e q R^2}{6\epsilon_0}. \tag{A.22}$$

Appendix B

# Power Supplies and Custom Electronics

## B.1 Pulsed High Current Capacitor Supply Circuit

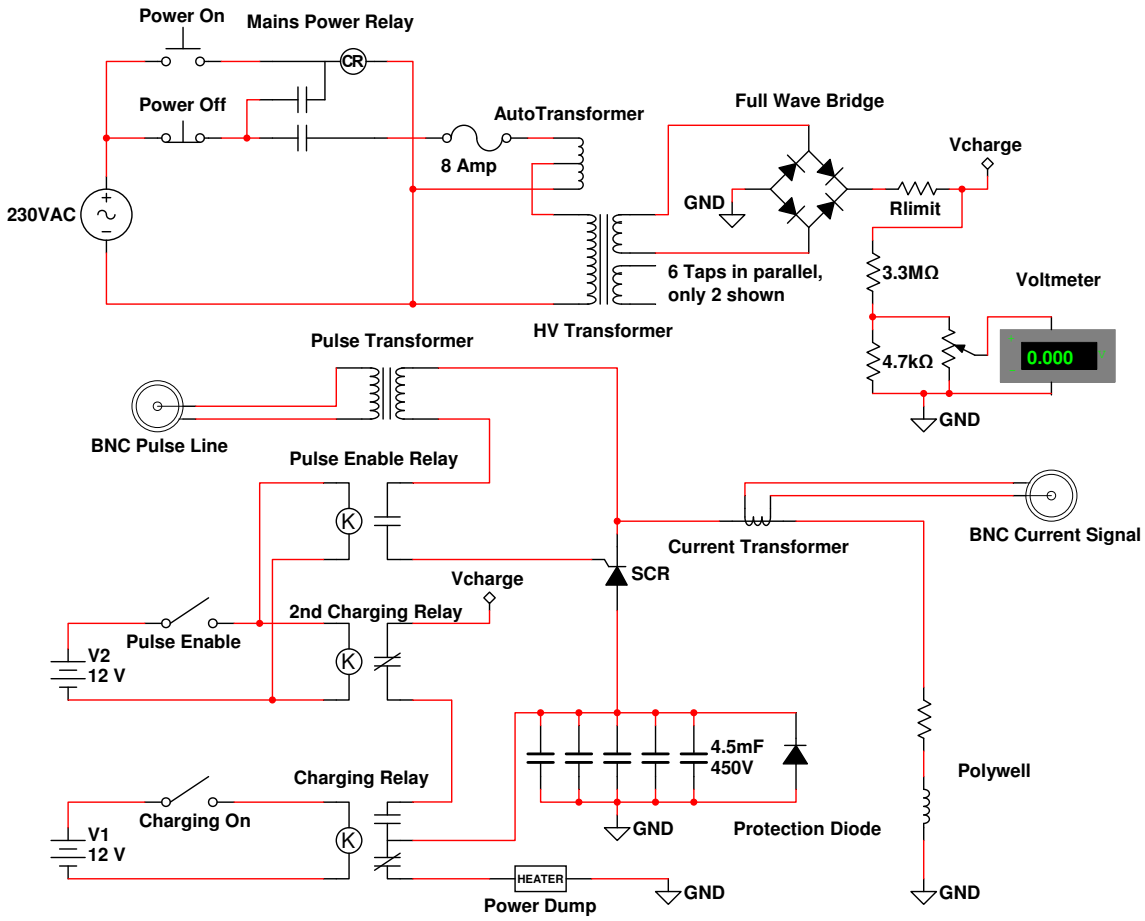


Figure B.1: This is the full circuit diagram for the pulsed high current power supply circuit discussed in section 3.1.2.

## B.2 Langmuir Probe Driver Circuit

This section contains detailed circuit schematics for each module of the custom Langmuir probe driver. High level descriptions of each module and their interactions are discussed in Section 3.3. In addition to the circuit schematics, we also include the hardware code for running the Arduino microcontroller.

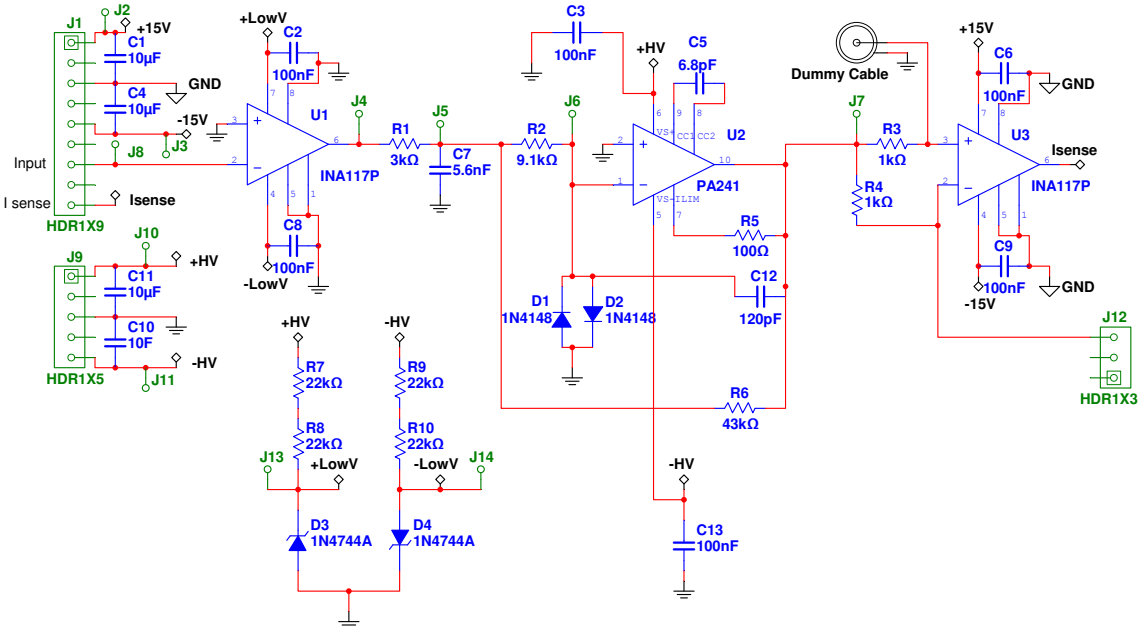


Figure B.2: High Voltage OpAmp module circuit diagram.

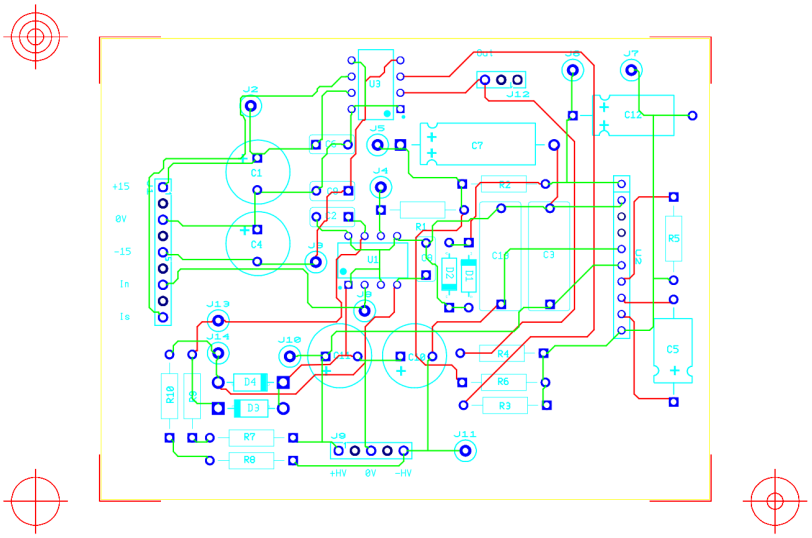

Figure B.3: The PCB board design for the High Voltage Op-Amp module.

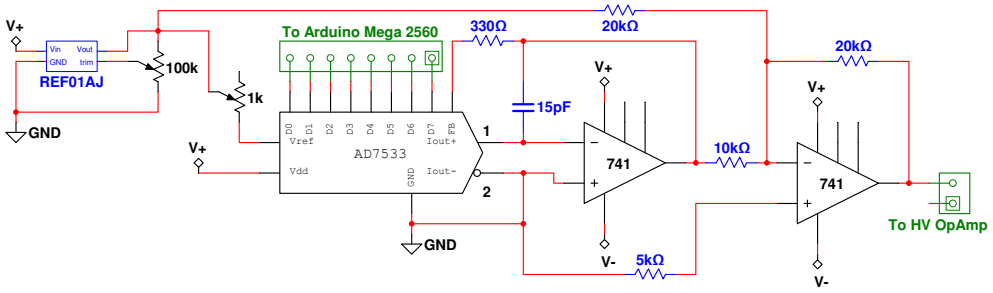


Figure B.4: The Digatal to Analog Conversion (DAC) module. Note that the AD7533 is actually a 10-bit DAC but was only used in 8-bit mode to attain higher sweep speeds. The extra logic bits are redundant since the Bessel filter in the HV OpAmp module smooths the voltage sweep to arbitrary resolution.

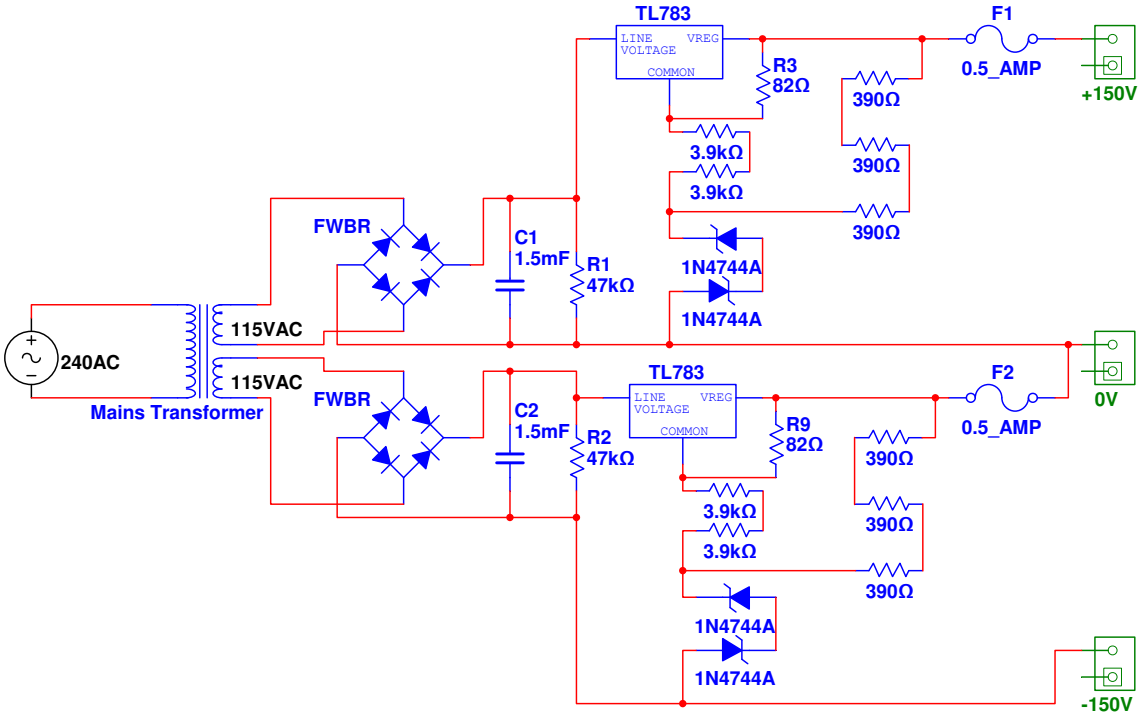


Figure B.5: The high voltage power supply module for supplying the dual ±150V supply rails to the HV OpAmp module.

### B.2.1 Arduino Microcontroller Code

```
/*
  Based on the public domain example code for
  the Freetronics LCD & Keypad Shield:

   http://www.freetronics.com/products/lcd-keypad-shield

  Original by Marc Alexander, 7 September 2011
  This example code is in the public domain.

  Edited by Matthew Carr, 26 January 2012

  Pins used by LCD & Keypad Shield:

    A0: Buttons, analog input from voltage ladder
    D4: LCD bit 4
    D5: LCD bit 5
    D6: LCD bit 6
    D7: LCD bit 7
    D8: LCD RS
    D9: LCD E
    D3: LCD Backlight (high = on, also has pullup high so default is on)

  ADC voltages for the 5 buttons on analog input pin A0:

    RIGHT:  0.00V :   0 @ 8bit ;   0 @ 10 bit
    UP:     0.71V :  36 @ 8bit ; 145 @ 10 bit
    DOWN:   1.61V :  82 @ 8bit ; 329 @ 10 bit
    LEFT:   2.47V : 126 @ 8bit ; 505 @ 10 bit
    SELECT: 3.62V : 185 @ 8bit ; 741 @ 10 bit
*/

#include <LiquidCrystal.h>   // include LCD library

/*-----------------------------------------------------------------------
  Defines
-----------------------------------------------------------------------*/
// Pins in use
#define BUTTON_ADC_PIN           A0  // A0 is the button ADC input
#define LCD_BACKLIGHT_PIN         3  // D3 controls LCD backlight
```

```
// ADC readings expected for the 5 buttons on the ADC input
#define RIGHT_10BIT_ADC           0  // right
#define UP_10BIT_ADC            145  // up
#define DOWN_10BIT_ADC          329  // down
#define LEFT_10BIT_ADC          505  // left
#define SELECT_10BIT_ADC        741  // right
#define BUTTONHYSTERESIS         10  // hysteresis for valid button
// sensing window return values for ReadButtons()
#define BUTTON_NONE               0  //
#define BUTTON_RIGHT              1  //
#define BUTTON_UP                 2  //
#define BUTTON_DOWN               3  //
#define BUTTON_LEFT               4  //
#define BUTTON_SELECT             5  //
//Variables
byte buttonJustPressed  = false;
byte buttonJustReleased = false;
byte buttonWas          = BUTTON_NONE;   //used by ReadButtons() for
// detection of button events
LiquidCrystal lcd( 8, 9, 4, 5, 6, 7 );

/*-----------------------------------------------------------------------
  Start Mathew's Additions
-----------------------------------------------------------------------*/
#define PULSE_INDICATOR          13  // RED LED
#define FilamentTrigger          2   // Filament Trigger BNC
#define PulsePolywellI           11  // Fire battery bank or Caps
#define OscilloscopeTrigger      10  // IV curve square wave indicator on BNC

#define TOPSCREEN                4   // Highest Screen Number
#define StartDelayScreen         0
#define DwellTimeScreen          1
#define MaxVoltScreen            2
#define MinVoltScreen            3
#define FlatScreen               4
int CurrentScreen = 0;
int CurrentScreenArray[] = {0,1};
int StartDelay = 2; // Time in milliseconds
float StartDelayArray[] = {0,0.5,1,1.5,2,2.5,3};
int DwellTime = 1; // Time in microseconds
int DwellTimeArray[] = {1,5,10,20,40,60,80,100};
```

```
int MaxVoltage = 140; // Time in milliseconds
int MinVoltage = -130;
int FlatVoltage = 100;
const int debounceDelay = 10;

int FilamentTime = 5;
int FilamentTimeArray[] = {1,2,3,4,5,6};

void setup()
{
  // initialize the digital pin as an output.
  pinMode(49, OUTPUT);
  pinMode(48, OUTPUT);
  pinMode(47, OUTPUT);
  pinMode(46, OUTPUT);
  pinMode(45, OUTPUT);
  pinMode(44, OUTPUT);
  pinMode(43, OUTPUT);
  pinMode(42, OUTPUT);
  PORTL = byte(128);
  pinMode(51, OUTPUT);
  pinMode(50, OUTPUT);
  digitalWrite(51, LOW);
  digitalWrite(50, LOW);

  pinMode(10, OUTPUT);
  pinMode(11, OUTPUT);
  pinMode(2, OUTPUT);
  digitalWrite(10, LOW);
  digitalWrite(11, LOW);
  digitalWrite(2, LOW);

   //button adc input
   pinMode( BUTTON_ADC_PIN, INPUT );         //ensure A0 is an input
   digitalWrite( BUTTON_ADC_PIN, LOW );      //ensure pullup is off on A0

   //LED INDICATORS
   pinMode(PULSE_INDICATOR, OUTPUT);
   digitalWrite(PULSE_INDICATOR, LOW);

   //lcd backlight control
```

```
   digitalWrite( LCD_BACKLIGHT_PIN, HIGH );  //backlight control pin D3 is high
   pinMode( LCD_BACKLIGHT_PIN, OUTPUT );     //D3 is an output
   lcd.begin( 16, 2 );
   lcd.setCursor( 0, 0 );   //top left
   //          1234567890123456
   lcd.print( "Langmuir Probe  " );
   lcd.setCursor( 0, 1 );   //bottom left
   lcd.print( "Ready for Sweep " );
}

/*--------------------------------------------------------------------------
  Main Loop + Screen Functions
--------------------------------------------------------------------------*/
void loop()
{
   byte button;
   byte timestamp;
   // get the latest button pressed, also the buttonJustPressed,
   // buttonJustReleased flags
   button = ReadButtons();

   if ( buttonJustPressed )
   {
     switch( button )
     {
       case BUTTON_NONE:
       {
         break;
       }
       case BUTTON_RIGHT:
       {
         if (CurrentScreen != TOPSCREEN)
         {
           CurrentScreen = CurrentScreen + 1;
         }
         else
         {
           CurrentScreen = 0;
         }
         break;
       }
```

```
case BUTTON_UP:
{
  switch (CurrentScreen)
  {
    case StartDelayScreen:
    {
      if (StartDelay != 6)
        StartDelay = StartDelay + 1;
      else
        StartDelay = 0;
      break;
    }
    case DwellTimeScreen:
    {
      if (DwellTime != 7)
        DwellTime = DwellTime + 1;
      else
        DwellTime = 0;
      break;
    }
    case MaxVoltScreen:
    {
      if (MaxVoltage != 140)
        MaxVoltage = MaxVoltage + 10;
      else
        MaxVoltage = 0;
      break;
    }
    case MinVoltScreen:
    {
      if (MinVoltage != 0)
        MinVoltage = MinVoltage + 10;
      else
        MinVoltage = -140;
      break;
    }
    case FlatScreen:
    {
      if (FlatVoltage != 140)
        FlatVoltage = FlatVoltage + 10;
      else
```

```
        FlatVoltage = -140;
      break;
    }
  }
  break;
}
case BUTTON_DOWN:
{
  switch (CurrentScreen)
  {
    case StartDelayScreen:
    {
      if (StartDelay != 0)
        StartDelay = StartDelay - 1;
      else
        StartDelay = 6;
      break;
    }
    case DwellTimeScreen:
    {
      if (DwellTime != 0)
        DwellTime = DwellTime - 1;
      else
        DwellTime = 7;
      break;
    }
    case MaxVoltScreen:
    {
      if (MaxVoltage != 0)
        MaxVoltage = MaxVoltage -10;
      else
        MaxVoltage = 140;
      break;
    }
    case MinVoltScreen:
    {
      if (MinVoltage != -140)
        MinVoltage = MinVoltage - 10;
      else
        MinVoltage = 0;
      break;
```

```
        }
        case FlatScreen:
        {
          if (FlatVoltage != -140)
            FlatVoltage = FlatVoltage -10;
          else
            FlatVoltage = 140;
          break;
        }
      }
      break;
    }
    case BUTTON_LEFT:
    {
      if (CurrentScreen != 0)
      {
        CurrentScreen = CurrentScreen - 1;
      }
      else
      {
        CurrentScreen = TOPSCREEN;
      }
      break;
    }
    case BUTTON_SELECT:
    {
      lcd.setCursor( 0, 0 );
      lcd.print( "                " );
      lcd.setCursor( 0, 1 );
      lcd.print( "   PULSE SENT   " );
      if (CurrentScreen == FlatScreen)
        FlatPulseFn();
      else
        VoltageSweep();
      break;
    }
    default:
    {
      break;
    }
  }
```

```
if (CurrentScreen == StartDelayScreen)
{
  lcd.setCursor( 0, 0 );   //top left
  //          1234567890123456
  lcd.print( "Starting Delay  " );
  lcd.setCursor( 0, 1 );   //bottom left
  lcd.print( "                " );
  lcd.setCursor( 0, 1 );   //bottom left
  lcd.print(StartDelayArray[StartDelay]);
  lcd.setCursor( 4, 1 );
  lcd.print( " ms        " );
}
else if (CurrentScreen == DwellTimeScreen)
{
  lcd.setCursor( 0, 0 );   //top left
  //          1234567890123456
  lcd.print( "Dwell Time      " );
  lcd.setCursor( 0, 1 );   //bottom left
  lcd.print( "                " );
  lcd.setCursor( 0, 1 );   //bottom left
  if (DwellTimeArray[DwellTime] <= 9)
    lcd.print( "  " );
  else if (DwellTimeArray[DwellTime] < 100)
    lcd.print( " " );
  lcd.print(DwellTimeArray[DwellTime]);
  lcd.setCursor( 4, 1 );
  lcd.print( "us         " );
}
else if (CurrentScreen == MaxVoltScreen)
{
  lcd.setCursor( 0, 0 );   //top left
  //          1234567890123456
  lcd.print( "Maximum Voltage " );
  lcd.setCursor( 0, 1 );   //bottom left
  lcd.print( "                " );
  lcd.setCursor( 0, 1 );   //bottom left
  if (MaxVoltage < 10)
    lcd.print( "   " );
  else if (MaxVoltage < 100)
    lcd.print( "  " );
  else
```

```
      lcd.print( " " );
    lcd.print(MaxVoltage);
    lcd.setCursor( 4, 1 );
    lcd.print( " V         " );
  }
  else if (CurrentScreen == MinVoltScreen)
  {
    lcd.setCursor( 0, 0 );   //top left
    //          1234567890123456
    lcd.print( "Minimum Voltage " );
    lcd.setCursor( 0, 1 );
    if (MinVoltage > -10)
      lcd.print( "  " );
    else if (MinVoltage > -100)
      lcd.print( " " );
    lcd.print(MinVoltage);
    lcd.setCursor( 4, 1 );
    lcd.print( " V         " );
  }
  else if (CurrentScreen == FlatScreen)
  {
    lcd.setCursor( 0, 0 );   //top left
    //          1234567890123456
    lcd.print( "Flat Voltage Pul" );
    lcd.setCursor( 0, 1 );
    if (FlatVoltage > 99)
      lcd.print( " " );
    else if (FlatVoltage < 100 && FlatVoltage >= 0)
      lcd.print( "  " );
    else if (FlatVoltage < 0 && FlatVoltage > -99)
      lcd.print( " " );
    lcd.print(FlatVoltage);
    lcd.setCursor( 4, 1 );
    lcd.print( " V         " );
  }
}

// clear the buttonJustPressed or buttonJustReleased flags,
// they've already done their job now.
if( buttonJustPressed )
   buttonJustPressed = false;
```

```
   if( buttonJustReleased )
      buttonJustReleased = false;
}

//  ReadButtons()
byte ReadButtons()
{
  byte state;
  byte previousState;
  previousState = GetState();
  for(int counter=0; counter < debounceDelay; counter++)
  {
    delay(1);
    state = GetState();
    if( state != previousState)
    {
      counter = 0; // reset the counter if the state changes
      previousState = state; // and save the current state
    }
  }

  //handle button flags for just pressed and just released events
  if( ( buttonWas == BUTTON_NONE ) && ( state != BUTTON_NONE ) )
  {
    buttonJustPressed  = true;
    buttonJustReleased = false;
  }
  if( ( buttonWas != BUTTON_NONE ) && ( state == BUTTON_NONE ) )
  {
    buttonJustPressed  = false;
    buttonJustReleased = true;
  }
  buttonWas = state;
  return(state);
}

byte GetState()
{
  byte button;
  unsigned int buttonVoltage;
  buttonVoltage = analogRead( BUTTON_ADC_PIN );
```

```
  if( buttonVoltage < ( RIGHT_10BIT_ADC + BUTTONHYSTERESIS ) )
  {
    button = BUTTON_RIGHT;
  }
  else if(   buttonVoltage >= ( UP_10BIT_ADC - BUTTONHYSTERESIS )
          && buttonVoltage <= ( UP_10BIT_ADC + BUTTONHYSTERESIS ) )
  {
    button = BUTTON_UP;
  }
  else if(   buttonVoltage >= ( DOWN_10BIT_ADC - BUTTONHYSTERESIS )
          && buttonVoltage <= ( DOWN_10BIT_ADC + BUTTONHYSTERESIS ) )
  {
    button = BUTTON_DOWN;
  }
  else if(   buttonVoltage >= ( LEFT_10BIT_ADC - BUTTONHYSTERESIS )
          && buttonVoltage <= ( LEFT_10BIT_ADC + BUTTONHYSTERESIS ) )
  {
    button = BUTTON_LEFT;
  }
  else if(   buttonVoltage >= ( SELECT_10BIT_ADC - BUTTONHYSTERESIS )
          && buttonVoltage <= ( SELECT_10BIT_ADC + BUTTONHYSTERESIS ) )
  {
    button = BUTTON_SELECT;
  }
  else
  {
    button = BUTTON_NONE;
  }
  return button;
}


/*-----------------------------------------------------------------------
  Sweep Voltages for Langmuir Probe -> Define Pulse Shape
-----------------------------------------------------------------------*/
void VoltageSweep()
{
  int MaxInt = map(MaxVoltage, -150, 150, 0, 255);
  int MinInt = map(MinVoltage, -150, 150, 0, 255) ;
  int StepNeg = (MinInt * -1)/35;
  int StepPos = MaxInt/35;
```

```
  digitalWrite(PULSE_INDICATOR, HIGH);
  digitalWrite(FilamentTrigger, HIGH);
  delay(FilamentTime * 1000);

  digitalWrite(PulsePolywellI, HIGH);
  delay(StartDelay);

  for (int number = 128; number > MinInt + 1; number = number - 1) {
    PORTL = byte(number);
    delayMicroseconds(DwellTime);
  }
  digitalWrite(OscilloscopeTrigger, HIGH);
  for (int number = MinInt; number < MaxInt; number++) {
    PORTL = byte(number);
    delayMicroseconds(DwellTime);
  }
  digitalWrite(OscilloscopeTrigger, LOW);
  for (int number = MaxInt; number > 129; number = number - 1) {
    PORTL = byte(number);
    delayMicroseconds(DwellTime);
  }
  PORTL = byte(128);
  delay(1);

  digitalWrite(PulsePolywellI, LOW);
  digitalWrite(FilamentTrigger, LOW);
  digitalWrite(PULSE_INDICATOR, LOW);
}

/*-----------------------------------------------------------------------
  Hold Arbritary Constant Voltage -> Confinement Time Measurements
-----------------------------------------------------------------------*/
void FlatPulseFn()
{
  int FlatInt = map(FlatVoltage, -150, 150, 0, 255);
  digitalWrite(PULSE_INDICATOR, HIGH);
  digitalWrite(11, HIGH);
  delay(StartDelay);

  digitalWrite(10, HIGH);
```

```
  PORTL = byte(FlatInt);
  delayMicroseconds(DwellTime * 100);
  digitalWrite(10, LOW);
  PORTL = byte(128);
  delay(2000);
  digitalWrite(PULSE_INDICATOR, LOW);
  digitalWrite(11, LOW);
}
```

# Index

advanced fuels, 13

binding energy, 2
Bussard's Polywells
    WB6, 55

coulomb barrier, 1

electron gun, 55, 59
    hollow cathode, 55, 59

HEPS experiment, 57, 59

langmuir probe, 62
loss cone, 8

magnetic confinement, 4
    closed systems, 4
    open systems, 6
magnetic field
    in the Polywell, 29
magnetic moment, 6
    adiabatic invariance, 6
magnetic pressure, 8
MHD instabilities
    flute, 8
MHD stability, 8, 9, 33
minimum B
    central well approximation, 43
mirror effect, 6
mirror machine, 6

nuclear fission, 1
nuclear fusion, 1
    candidate reactions, 2

power supply
    pulsed, 52, 59

reaction rate, 3

scaling laws, 57, 59

Teflon Polywell, 51, 53, 59
    schematic, 53, 60
tokamak, 4